LOW REYNOLDS NUMBER SWIMMING OF HELICAL STRUCTURES AND RIGID SPHERES

by

EBRU DEMİR

Submitted to the Graduate School of Engineering and Natural Sciences

in partial fulfilment of the requirements

for the degree of

Doctor of Philosophy

SABANCI UNIVERSITY

JULY 2018

LOW REYNOLDS NUMBER SWIMMING OF
HELICAL STRUCTURES AND RIGID SPHERES

APPROVED BY:

Prof. Dr. Serhat Yeşilyurt
(Dissertation Supervisor)

Assoc. Prof. Dr. Güllü Kızıltaş Şendur

Assoc. Prof. Dr. Ayhan Bozkurt

Prof. Dr. Mehmet Şahin

Asst. Prof. Dr. Yegân Erdem
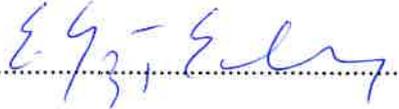
DATE OF APPROVAL: 19/07/2018

ABSTRACT

LOW REYNOLDS NUMBER SWIMMING OF HELICAL STRUCTURES

AND RIGID SPHERES

EBRU DEMİR

Ph.D. Dissertation, July 2018

Dissertation Supervisor: Prof. Serhat Yeşilyurt

Keywords: Confined Swimming, Micro Swimmer, Bio-inspired Artificial Helical

Swimmers, Rigid Spheres, Hydrodynamic Focusing, Computational Fluid Dynamics,

Resistive Force Theory, Magnetic Actuation

Micro swimmers have a great potential to realize minimally invasive medical procedures to detect and treat diseases. They are promising candidates for achieving targeted drug delivery, which can reduce the side effects of potent drugs and minimize the secondary complications of dangerous treatments. However, swimming at low Reynolds number environments such as bodily fluids requires breaking the time reversal symmetry to achieve propulsion, therefore swimming of micro structures in viscous environments presents a challenge. In this thesis, swimming characteristics and performance of both chiral and magnetically actuated axisymmetric structures swimming inside cylindrical

conduits at low Reynolds numbers are investigated using computational and numerical models, as well as experimental studies. Computational tools that predict the swimming performance of both chiral and axisymmetric swimmers are presented to provide a comprehensive analysis that considers both types of swimmers used in this research field. Effects of geometric parameters on the swimming performance of chiral structures are analyzed and guidelines for designing helical tails for optimized velocity or efficiency are established using a computational fluid dynamics model. Symmetry breaking with axisymmetric particles is achieved by exploiting their hydrodynamic interactions with confining boundaries. A numerical model based on the resistive force theory that can predict their trajectories with high accuracy is reported. Non-inertial focusing and controlled motion of rigid spheres inside cylindrical channels are experimentally demonstrated. The findings presented contribute to our understanding of the swimming characteristics of both symmetric and asymmetric micro swimmers and pave the way for new applications.

ÖZET

SARMAL YAPILAR VE KATI KÜRELERİN DÜŞÜK REYNOLDS SAYILI ORTAMLARDA YÜZMESİ

EBRU DEMİR

Doktora Tezi, Temmuz 2018

Tez Danışmanı: Prof. Dr. Serhat Yeşilyurt

Anahtar Kelimeler: Sınırlandırılmış Alanda Yüzme, Mikro yüzücü, Doğadan Esinlenilmiş Helis Yüzücüler, Sert Küreler, Hidrodinamik Odaklama, Bilgisayarlı Akışkanlar Dinamiği, Direnç Kuvveti Teorisi, Manyetik Tahrik

Mikro yüzücüler, hastalıkların tanısı ve tedavisine yönelik minimal invasif medikal uygulamaların gerçekleştirilmesini sağlayabilecek büyük potansiyele sahiptir. Tehlikeli tedavilerin yan etkilerini azaltıp tedavi kaynaklı ikincil sorunların giderilmesini sağlayabilecek hedefli ilaç taşınımının gerçekleştirilmesinde umut vaat eden adaylardır. Ancak, vücut salgıları gibi düşük Reynolds sayısına sahip ortamlarda küçük ölçekli yüzücülerin itki elde edebilmesi, yüzmeyi sağlayacak hareketin zaman göre simetrisini kırabilmeyi gerektirir; bu da viskoz ortamlarda mikro yüzücülerin ilerleyebilmesini zorlu bir görev yapmaktadır. Bu tezde kiral ve aksisimetrik yüzücülerin düşük Reynolds sayılı

ortamlarda silindirik kanal içinde yüzme performansları bilgisayarlı simülasyon, numerik modelleme ve deneysel çalışmalar kullanılarak incelenmiştir. Bu araştırma alanında kullanılan kiral ve aksisimetrik yüzücülerin performansını geniş bir çerçevede ve yüksek tutarlılıkla analiz etmede kullanılabilecek bilgisayarlı hesaplama metotları sunulmuştur. Kiral yapıların yüzmesine etki eden geometrik parametreler analiz edilmiş ve bu yüzücülerin maksimum hız ya da verimlilik açısından optimize edilmesine olanak tanıyacak bir kılavuz oluşturulmuştur. Aksisimetrik parçacık kullanılarak yüzme hareketinin zamana göre simetrisinin kırılması, küresel yüzücünün silindirik kanalla hidrodinamik etkileşimleri kullanılarak başarılmıştır. Direnç kuvveti teorisinden faydalanarak hazırlanan numerik modelin küresel yüzücülerin gezingelerinin yüksek tutarlılıkla hesaplayabildiği gösterilmiştir. Sert kürelerin eylemsizlik kuvvetlerinden bağımsız olarak silindirik kanal içerisinde merkez eksene odaklanması deneysel olarak gösterilmiştir. Bu tezde sunulan bulgular hem kiral hem aksisimetrik yüzücülerin karakterizasyonuna dair bilgi birikimimize katkıda bulunarak, mikro yüzücüler ile başarılabilecek yeni uygulamaların önünü açma potansiyeline sahiptir.

To my brother, my saving grace…

ACKNOWLEDGEMENTS

I am so happy to see that I need to write an acknowledgement that many might consider a bit long, because that only shows how incredibly blessed I was for being surrounded by such a great number of amazing mentors, family and friends all along the road, who contributed to this thesis and to me as a person, each in their unique way.

I wish to thank my thesis supervisor, Prof. Serhat Yeşilyurt. It has been an honor and a privilege to have him as my mentor. He provided me with ample support and guidance throughout my studies, but most importantly, he did so without taking away from my freedom to explore and to follow where my curiosity leads me. He taught me to enjoy my work, to go beyond what is visible and see where it might lead to, and to be proud of it. He put my mental and physical well-being above all else and made sure that I was in the right mindset all the way. Without his exceptional guidance and support, completing this thesis would not have been possible.

Prof. Güllü Kızıltaş Şendur deserves my sincerest gratitude for never being too busy to help a student in need. She always made me feel welcome, both for long academic debates and for moral support. She is the kind of person that never shies away from going that extra mile and making sure that her students are doing well mentally as much as they are doing well academically. I have been very lucky to have benefitted from her wisdom and I will never forget the example she set for me if I ever have my own students one day.

I thank Prof. Ayhan Bozkurt for always having greeted me with a smile whenever I had a question. His feedbacks and contributions were essential in the completion of this thesis. I would also like to thank professors Mehmet Şahin and Yegan Erdem for taking the time to evaluate my work.

 Prof. Melih Papila has been a huge support over the years, and I am forever indebted to him for taking a personal interest not only in my development as a researcher but also in my well-being. He did everything he could to boost my self-confidence, to make me believe in myself, to help me get through hard times that are an inevitable part of such a long journey. Prof. Berrin Yanıkoğlu deserves no less praise, as she provided tremendous moral support. She encouraged me to go beyond my comfort zone and to test my abilities without fear, which resulted in invaluable and cherished experiences.

are too numerous to count, and the words wouldn't do her justice anyway. I am very lucky to have had such a strong and compassionate woman to look up to.

Not all family members are tied by blood, so I would also like to thank my "adopted family". Here are the people I wish to have by my side until the end of my life, for without them I don't think life would be as meaningful or as enjoyable as they have made it: I thank Damla Yılmaz and Fatma Istık, for more than 10 years of sincerest friendship, which was frankly nothing short of sisterhood. These amazing ladies have been my rock, my secret-keepers, and my companions in everything from the most joyful to most sorrowful moments. My big brother İlker "Abi" Sevgen, went beyond the sense of duty in helping me. I learned a lot from him in every step, and he shared every material and immaterial source he had at his disposal to make sure my experience as a PhD student was a smooth, successful, and enjoyable one. I thank Yağmur Büyüköztürk for piquing my curiosity, making me want to learn more, achieve more. She was also a constant source of laughter, even when she stayed up late just to keep me company. I thank both her and Kutay Büyüköztürk for sharing their home with me whenever I needed, and for devoting their time and intellect to help me achieve whichever task I was dealing with. I thank all these three, İlker Abi, Yağmur and Kutay for awesome Friday nights which I always looked forward to as they were always the highlight of my week, for amazing memories at distant lands, for making my last year as a PhD student the best year ever when it was supposed to be the hardest one. I thank Hadi Çağdaş Erk for an endless supply of jokes so bad that they were actually good, for never sparing his familiar smile after all these years, and for lending me his precious printers and saving me when I was alarmingly short on time. I thank Merve Zuvin for her company all these years. We have shared and endured so much, and finally got to the end together. I hope that life will give us more enjoyable moments in this new chapter of our lives. I am grateful to Kadir Uzun, for his cheerful presence, for always being there when it matters the most, for the most spontaneous and much needed escapes, and for sharing my passion for books. Since the beginning of our friendship we always seemed to find ourselves faced with an obstacle, whether it be a real crisis or just a deadline to be met, but it meant a lot to me to overcome them together with a smile on our faces.

TABLE OF CONTENTS

LIST OF FIGURES

LIST OF SYMBOLS

Re	Reynolds Number
p	Pressure
$\mathbf{u}$	Velocity
f	Frequency
l	Length Scale
μ	Viscosity
$\mathbf{\Omega}$	Angular Velocity Vector
$\mathbf{r}$	Position Vector
$\mathbf{r_0}$	Position Vector of the Centroid
S	Surface of the Swimmer Body
ω_i	Angular Velocity in i-direction
$\mathbf{\sigma}$	Stress Tensor
$\mathbf{n}$	Local Surface Normal
$\mathbf{F}_{net}$	Net Force
$\mathbf{T}_{net}$	Net Torque
λ	Wavelength
η	Efficiency
η_0	Reference Efficiency
m	Mobility
m_0	Reference Mobility
B	Radius of the Helical Tail
a	Thickness of the Helical Tail
z_0	Eccentricity

R_{ch}	Channel Radius
d	Helical Ribbon Thickness
w	Helical Ribbon Width
U_{sw}	Swimmer Velocity in x-direction (helices)
U_{sph}	Swimmer Velocity in x-direction (spheres)
R_a	Translational Resistance Coefficient of the Helical Tail
R_b	Coupling Resistance Coefficient of the Helical Tail
R_c	Rotational Resistance Coefficient of the Helical Tail
c	Separation between the Helical Tail and the Channel Wall
V	Swimmer Velocity in y-direction
τ_m	Magnetic Torque
μ_0	Permittivity of the Free Space
m	Magnetic Dipole Moment
B	Magnetic Field
M	Magnetization Vector
H	Magnetic Field Strength
D_{sph}	Diameter of the Sphere
D_{ch}	Diameter of the Channel
$\mathbf{e_k}$	Local Position Vector of the Sphere
$\mathbf{F^{tt}}$	Translation Resistance Matrix
$\mathbf{F^{tr}}$	Coupling Resistance Matrix
$\mathbf{F^{rt}}$	Transpose of Coupling Resistance Matrix
$\mathbf{F^{rr}}$	Rotation Resistance Matrix
$\mathbf{f_p}$	Forces due to Pressure Variation

$\mathbf{f_{visc}}$	Viscous Force
$\mathbf{f_{mag}}$	Magnetic Force
$\mathbf{f_{hist}}$	Basset-Boussinesq History Force
$\mathbf{f_{mass}}$	Added Mass Force
$\boldsymbol{\tau_{mag}}$	Magnetic Torque
R	Distance between Center of the Sphere and Channel Axis
β	Proximity Parameter ($R/(R_{ch}-R_{sph})$)
δ	Closest Distance from Sphere Surface to Channel Wall
υ_θ	Rotation Rate of the Sphere about x-axis (Helical Trajectories)
C	Lift Force Gain

LIST OF ABBREVIATIONS

AMS   Artificial Micro Swimmers

SBT   Slender Body Theory

APS   Approximate Perturbative Solution

SRT   Slender Ribbon Theory

BEM   Boundary Element Method

CFD   Computational Fluid Dynamics

DOF   Degree of Freedom

PDMS   Polydimethyl Siloxane

1   INTRODUCTION

Targeted drug delivery is one of the most coveted applications of modern medicine. Delivering potent drugs (e.g. chemotherapeutic drugs) only to the disease-ridden parts of the body instead of using them systemically has the advantage of eliminating side effects and possibly allowing an increase of dosage due to the fact that only the targeted tissues or organs would be majorly affected. Furthermore, such an application could be life saving for the patients that have multiple symptoms that require opposite treatments. For example, tumors are known for throwing blood clots that cause organ or respiratory failures and are one of the most significant secondary causes of mortality. However, the majority of cancer patients receiving chemotherapy or radiation therapy develop thrombocytopenia, which significantly increases the risk of internal bleeding. Therefore, such patients cannot be treated with anticoagulants and need invasive treatments to dissolve or dislodge a simple blood clot, which is again life threatening in their delicate state. Thus, targeted drug delivery might be the answer that decreases the mortality rate in diseases where the treatment itself can be as dangerous as the disease.

A wide range of techniques have been explored towards achieving this aim and some attempts produced promising results. Among these, applications featuring bio-inspired artificial micro swimmers (AMS) dominate the literature and are considered to be one of the best candidates for this task. The idea is to introduce swimmers into the circulatory system and use them to navigate the drugs only to the targeted organs or tissues. Nonetheless, navigating artificial swimmers inside blood vessels accurately where the blood flow velocity can reach 45 cm/sec is not an easy task (Figure 1.1). Blood vessels with smaller diameters have the slowest blood flow due to their higher relative

cross-sections (Figure 1.1). For this reason and to be able to reach remote body parts, the swimmer that can be used for such applications must be miniaturized. This requirement brings about another challenge.
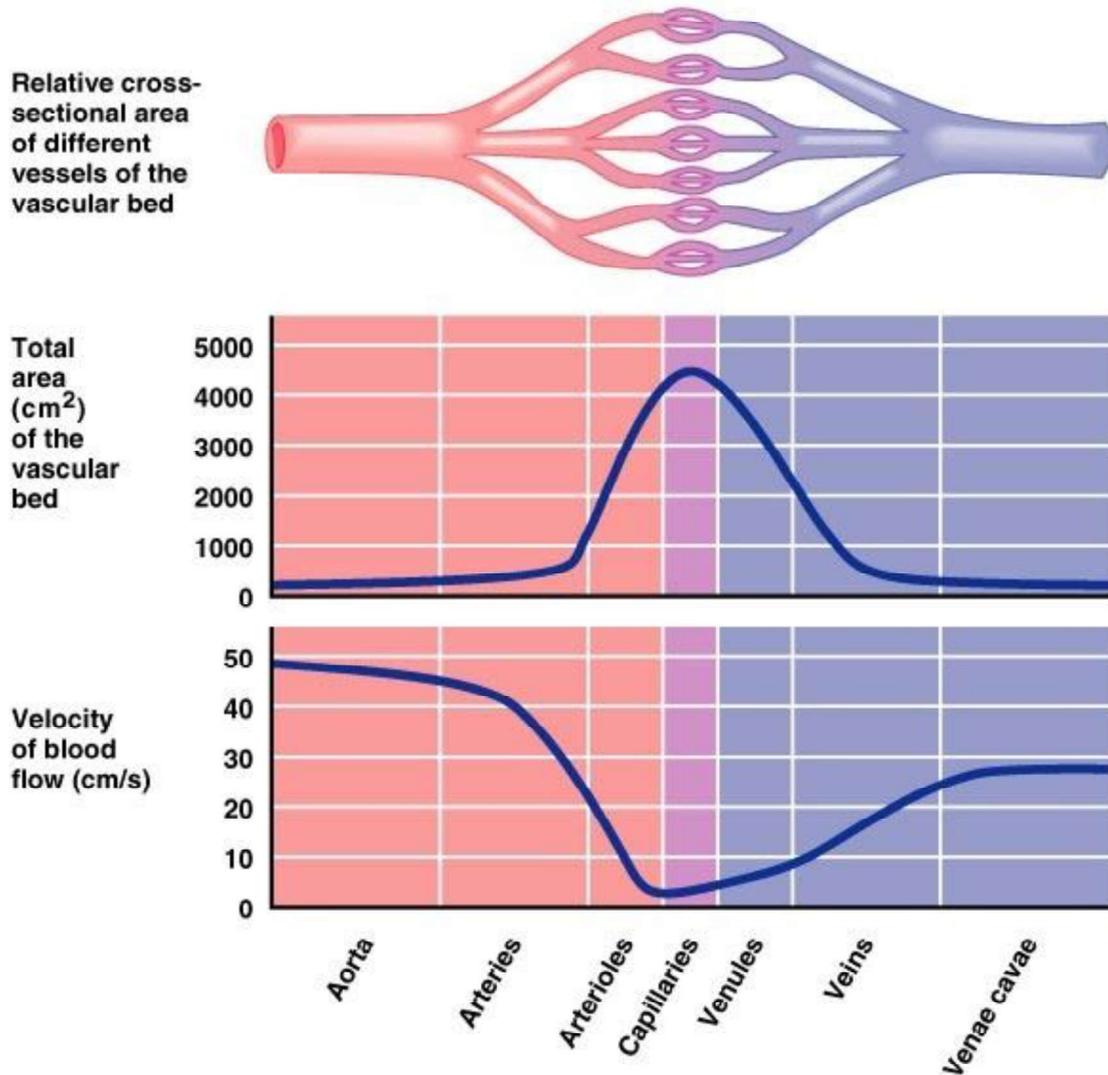
Figure 1.1 Blood vessels of various cross-sectional areas and corresponding blood flow velocity inside different types of vessels.

Due to their miniature sizes, AMS swim in low Reynolds number (*Re*) regime, where prevalent propulsion methods are rendered useless. Purcell's [1] Scallop Theorem explains that the kinematic reversibility of the fluid flow at low Reynolds number regime due to the disappearance of the time relation in the Navier-Stokes equation results in zero net displacement when the motion performed by the swimmer is reciprocal. Small swimmers in low *Re* environments must adapt strategies to break the symmetry of the

2

motion, or the fluid flow with respect to time. Bacteria, microbes, spermatozoa swim in low *Re* conditions and propel themselves with ease, therefore, scientists look at the nature for an answer to this problem. It is observed that the small organisms propel themselves by means of flagella, cilia or complex body deformations. This is how, inspired by nature, creating such appendages artificially or designing swimmers that can propel themselves via surface or body deformations became a wide research area and a promising solution to the drug delivery problem.
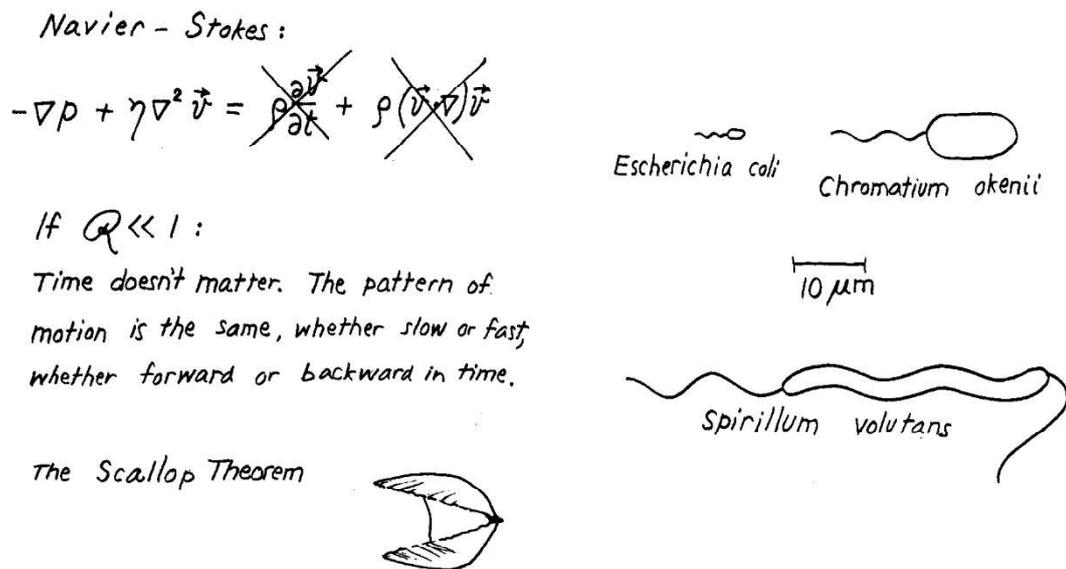
Figure 1.2 Purcell's Scallop Theorem and bio-inspired solutions [1]

As the research on this area gained momentum, the application area of the artificial swimmers expanded accordingly. Micro swimmers are now used as diagnostic tools and help in medical imaging [2]. Researchers found new ways the break the symmetry and escape the Scallop Theorem by surface engineering or by using alternative fluidic environments [3-4]. Artificial helical flagella and self-propelling spherical particles are in abundance in the literature. However, there are still many unknowns about their swimming performances in different environments.
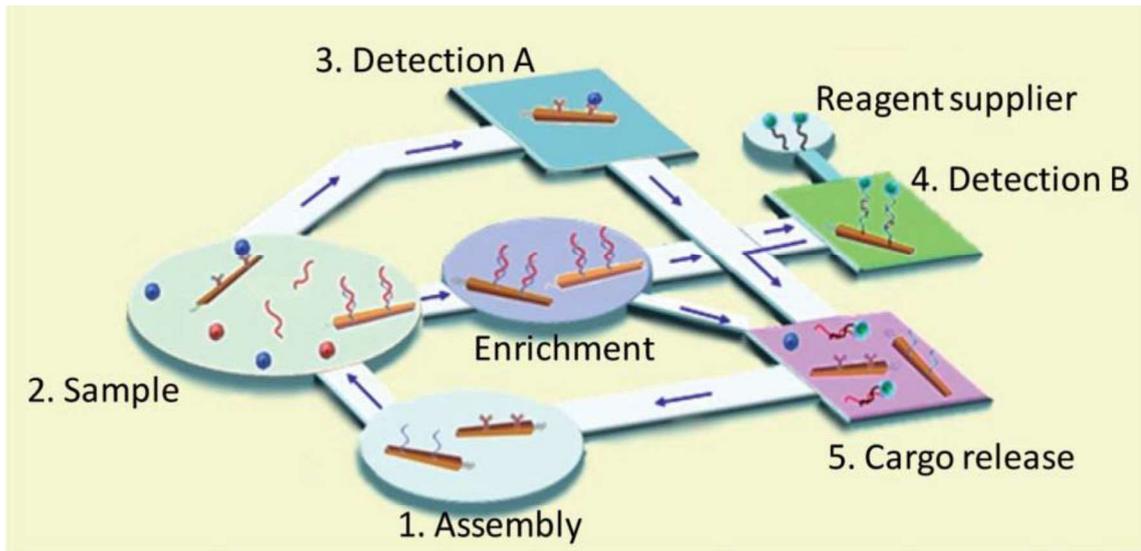
Figure 1.3 Artificial transporter picks the targeted molecule, transports it, tags it and releases it [2].

In the first chapter of the thesis, a literature review to construct a comprehensive background is presented. Following the literature review, motivation of the work covered in this thesis is discussed.

In the second chapter of this thesis, a computational study that aims to fill one of these gaps is presented. Swimming performance of helical structures swimming at low *Re* environments inside cylindrical conduits are largely dependent on their geometric properties. Identification of the geometric parameters that enhance the velocity or efficiency of a swimmer may become crucial in the accuracy of the desired applications. However, an extensive analysis of the geometric parameters constructing the helix and a guideline to manipulation of geometric proportions to a specific end is missing. Helices are hard to produce in small scales, therefore, predicting their performance prior to production is also important. The work presented in chapter two demonstrates a very efficient and highly accurate computational fluid dynamics (CFD) model that can be used to analyze the performance of a helical swimmer of arbitrary cross-section. Comprehensive results obtained using the CFD model proposed are also presented to serve as a guideline.

The third chapter focuses on the swimming behavior of spherical particles in cylindrical channels. First, the experimental study conducted to identify different swimming modes is presented. Then, implementation of a numerical model that can be

used to predict the behavior of magnetically actuated rigid spheres inside cylindrical conduits is explained. Accuracy of the model in various actuation modes is discussed and problems to be solved for improvement are identified.

The two chapters together establish a comprehensive analysis of swimming behavior of micro swimmers swimming in low *Re* environments regardless of their shape, whether they are chiral or axisymmetric. The tools proposed in this thesis can be applied to chiral and axisymmetric structures of alternative shapes and cross-sections. It is demonstrated that through identification of key parameters and governing dynamics, computationally efficient and highly accurate models can be constructed.

1.1. Literature Review

Artificial micro swimmers (AMS) present a huge potential for medical applications, such as drug delivery and minimally invasive surgical operations [5–9]. Various approaches for the design of AMS are inspired by microorganisms, such as bacteria or spermatozoa, that move by means of beating or rotary motion of cilia and flagella in aqueous solutions [10–12]. Advances in fabrication techniques allow producing a diverse range of shapes that serve as bio-mimetic artificial propellers [8, 9, 13–18]. External magnetic fields have been used extensively for the actuation of AMS with helical tails. Ghosh and Fischer [19] manufactured micron long SiO_2 helical micro swimmers, actuated by Helmholtz coils and navigated to demonstrate controllable trajectories. Li *et al.* [20] demonstrated the swimming of helical nano swimmers, which are as small as 100 nm in diameter and 600 nm in length based on the electro-deposition of Pd/Cu nanorods into nanoporous membranes as described by Liu *et al.* [21]. Gao *et al.* [22] deposited Ti and Ni layers directly onto the spiral water-conducting vessels obtained from various plants, and tested the swimming performance of these magnetically actuated helical swimmers at different frequencies using Helmholtz coils. Zhang *et al.* [23] employed micro manufacturing techniques to produce 42 nm thick helical ribbons 1.8 μm in width and 49.7 μm in length. Similarly, artificial bacterial flagella of 16 microns in length and 5

microns in diameter are manufactured by Qiu *et al.* [24] and used for temperature controlled, targeted drug administration. Maier *et al.* [25] demonstrated swimming of DNA-based flagellar bundles featuring magnetic beads. In another study featuring multiple flagella, Beyrand *et al.* [14] examined different swimming modes such as tumbling, rolling, and wobbling along with the capability of the AMS in cargo transport. Lastly, magnetotactic bacteria are utilized as self-propelled natural micro robots and controlled by time-varying magnetic fields [26] to perform complex micro assembly tasks [27]. Further examples on various fabrication and actuation methods of micro swimmers are reviewed by Peyer *et al.* [28]. Advances in drug delivery featuring artificial micro swimmers are reported by Gao and Wang [29].
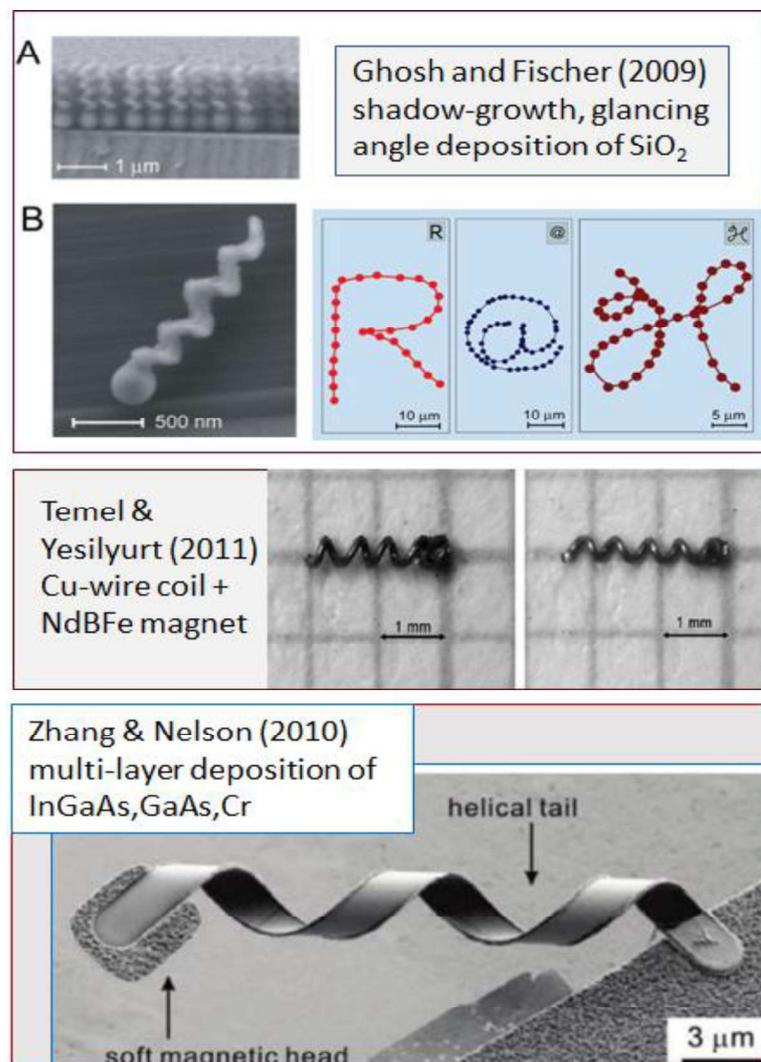
Figure 1.4 Various artificial helical micro swimmers. Ghosh and Fisher [19] presented the use of glancing angle deposition method to produce helical swimmers and demonstrated their accurate control, Temel and Yesilyurt [30] created swimmers with Cu wire and permanent magnets and magnetically actuated them, Zhang and Nelson [31] manufactured helical ribbon by multilayer deposition.

6

In addition to experiments that demonstrate the efficacy of helical swimming, helical tails have been studied by several authors theoretically and computationally. Sir James Lighthill's Slender Body Theory (SBT) [32] predicts the swimming velocity accurately for unconfined, infinitely long, thin helical filaments. On the other hand, Felderhof's approximate perturbative solution (APS) [33] includes the effect of confinement for infinitely long cylinders with helical perturbations, and solves for the velocity and efficiency correctly for small helical amplitudes compared to the confinement radius. Man and Lauga [34] used resistive force coefficients to analyze the wobbling behavior of helices that rotate with an external magnetic field and showed that swimming is more efficient for larger wavelengths and number of waves due to decreasing wobbling of the swimmer. Koens and Lauga [35] report the development of slender ribbon theory (SRT) and resistance coefficients for helical ribbons which are defined by two length scales for the cross-section, namely, thickness and width, for only slender geometries, whose thickness is much smaller than other dimensions.

Computational studies on helical swimmers have utilized mostly the boundary element method (BEM). Liu *et al.* [36] investigated helical filaments swimming inside a circular channel with BEM by varying the helical pitch angle and the ratio of the filament thickness to the arc length of one helical turn, and reported the swimming characteristics under constant torque and constant angular velocity applications with respect to the confinement. Spagnolie and Lauga [37] presented a numerical study to predict the optimal shape for elastic flagella of both finite and infinite sizes in terms of hydrodynamic efficiency and compared the results to Lighthill's findings on optimal flagellum [38]. The authors [37] concluded that for infinitely-long flagella, helical shapes are the optimal in three dimensions, whereas modified saw-tooth profiles are found to be more efficient in two dimensions, which are variations on the geometries suggested by Lighthill [38]. Spagnolie *et al.* [39] demonstrated that the effect of viscoelasticity on the swimming characteristics is dependent on the shape of the helical tails. Performance of confined helical tails with different cross-sections and pitch angles is studied by Li and Spagnolie [40] to determine optimum helical shapes for efficient swimming and pumping. Montenegro-Johnson *et al.*[41] developed a BEM tailored for ribbons and sheets, that accurately captures the swimming dynamics of slender swimmers with lengths comparable to their widths. Keaveny and Shelley [42] investigated propagating helices with elliptic cross-sections by calculating the tractions on the swimmer body using

numerical solutions of the boundary integral equations. Keaveny *et al.* [43] also utilized the boundary integral formulations to replicate the swimming speeds measured experimentally for various helical swimmers, and suggest variations on the design (such as centerline optimization) to maximize speed. In addition to BEM, Acemoglu and Yesilyurt [44] used a CFD model to study swimming of a model microorganism with a helical tail in cylindrical channels and reported effects of geometric parameters of the helical tail on the swimming velocity and efficiency.

In addition to swimming of helical tails, various studies are conducted to understand and predict the behavior of spherical particles swimming inside conduits or near boundaries, both in the presence of a flow and in a quiescent fluid. Brenner and Happel [45] investigated the frictional drag on a sphere subjected to a Poiseuille flow using the method of reflections. They concluded that an optimum distance between the sphere center and central axis of the cylindrical conduit exists, where the drag is minimized. However, their results are valid in asymptotic cases where the distance between the sphere and the channel wall is much larger than the sphere radius. Goldman et al. [46] took near wall effects of nearly planar wall, their results can only apply when the channel radius is considerably greater than the sphere radius. Bungay and Brenner [47] studied the motion of spherical particles in a tightly fitting cylindrical conduit and proposed an improvement on the existing lubrication theories, which is still widely used in cases the sphere and the channel wall are in close proximity. Higdon and Muldowney [48] used spectral boundary element method to obtain friction coefficients of spheres swimming inside cylindrical conduits. They presented tabulated results for a range of D_{ch}/D_{sph} ratios, which can be used to predict swimming behavior of spheres that swim under zero net torque condition, at any distance from the channel wall. For the cases when sphere is too close to the channel wall, they employed the lubrication theory. As zero torque conditions are applied, rotational friction coefficients and coupling friction coefficients are not reported.

More recently, Bhattacharya et al. [49] reported a basis transformation model that overcomes the limitations of the asymptotic models. They presented translational, rotational and translation-rotation coupling friction coefficients for spheres at an arbitrary radial position, and for various D_{ch}/D_{sph} ratios. The model predicts that based on the D_{ch}/D_{sph} ratio and the distance of the sphere from the channel wall, a sphere rotating at a constant angular velocity might roll in one direction or slide in the opposite direction due to the adverse pressure gradient. Zhu et al. [50] opted for boundary element method to

study the motion of spherical squirmers in capillary tubes. They focused more on the work necessary to swim, trajectory followed by the particles, and on the comparison of pusher and puller type swimmers. They concluded that the puller type swimmers are following a more stable trajectory, and that the presence of a confinement increases the amount of work done to achieve swimming.
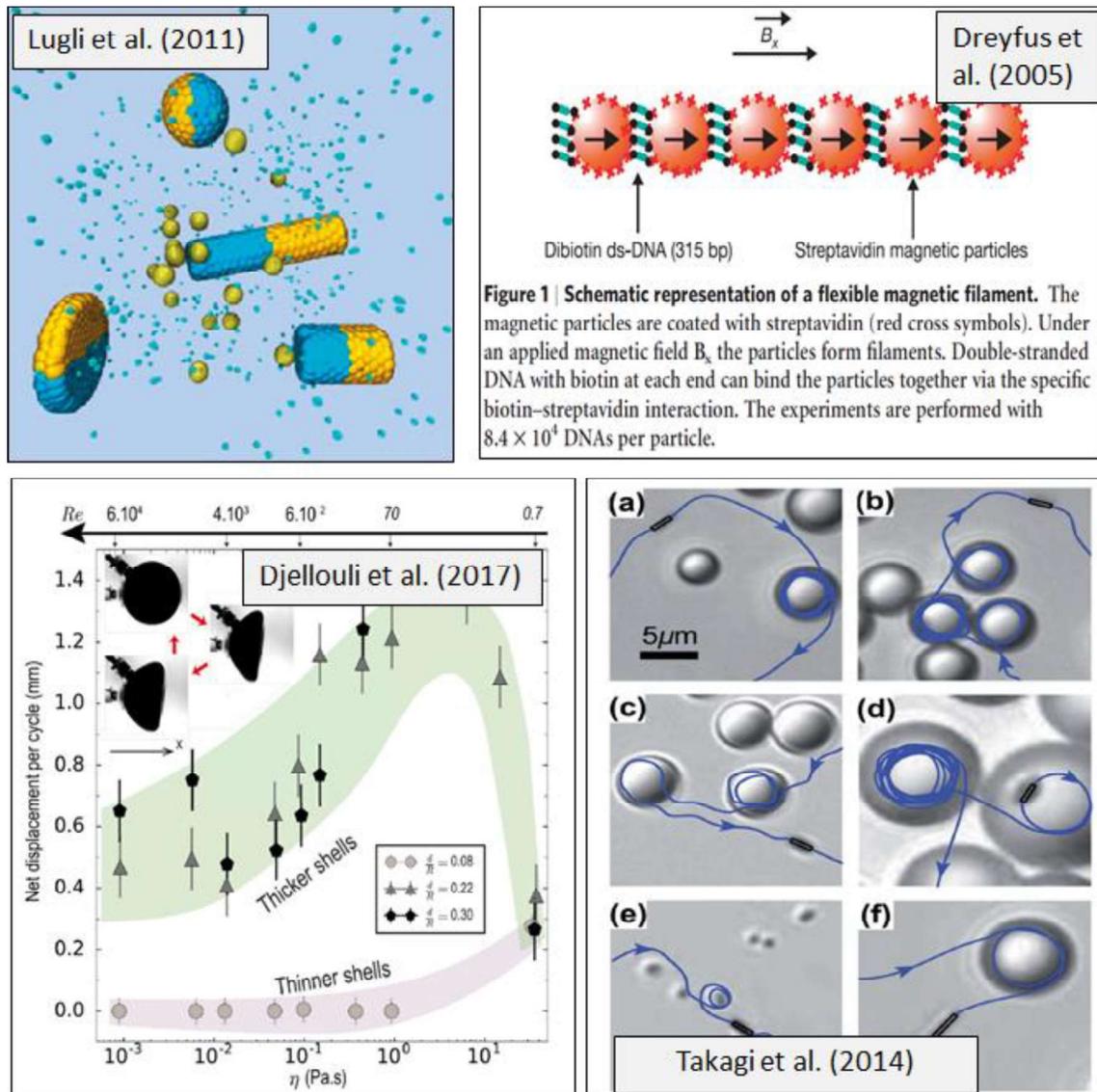
Figure 1.5 Strategies to break symmetry with spherical particles: Lugli et al. [51] analyse the shape dependence on the performance of the Janus particles that utilize asymmetric chemical reactions to achieve propulsion, Dreyfus et al. [52] used DNA to bind magnetic particles, Djellouli et. al. [53] exploit surface deformations and Takagi et al. [54] break the symmetry using hydrodynamic interactions with the boundaries.

In addition to general analyses on the motion of spheres inside confinements, peculiar behavior such as the anomalous rolling of spheres near inclined planes are reported in the literature, namely, the motion of a sphere rotating as though climbing the inclined plane despite falling downwards. One of the earliest mentions of a similar behavior is reported by Cox et al. [55], where the authors deduct that, sphere should slip as it rolls near a boundary, which is demonstrated by Liu et al. [56] experimentally. The authors found that, when a sphere is dropped near a planar wall, depending on the nature of the fluid used (Newtonian vs. Non-Newtonian) and the angle of inclination of the wall, the sphere might perform rolling, sliding or anomalous rolling. When the wall is vertical, sphere is found to display anomalous rolling in both Newtonian and Non-Newtonian fluids, and that it shies away from the wall. They observed that the sphere transitions to normal rolling in Newtonian fluids, once the inclination of the planar wall is beyond a critical angle, however, that anomalous rolling still persisted in Non-Newtonian fluids. More studies reporting the behavior of the spherical particles approaching a boundary or falling near a boundary [52–56], and studies on collective behavior of multiple particles [57-58] can also be found in the literature.

Construction of the equation of motion for a swimming sphere has an extensive trail in the literature dating back to 1880s. Basset [64], Boussinesq [65] and Oseen [66] studied the motion of a sphere settling under the gravity force in a quiescent fluid. In such a fluid, only disturbance to the flow occurs due to the settling motion of the sphere, which of low Reynolds number and thus allows deduction of the resulting fluid force on the sphere using Stokes equations [67]. Tchen [68] extended their work to include unsteady flows in his PhD thesis, which prompted an immense number of studies suggesting corrections to his equations. Among the notable corrections, Corrsin and Lumley's [69] remark on the contribution of the pressure gradient on the net force acting on the particle, and Buevich's [70] correction on the term suggested by [69] should be listed. Soo [71] and Gitterman and Steinberg [72] offered their own solutions. In 1982, Maxey and Riley [67] derived the equation its widely used form to this day with corrections of Auton et al. [73] and Maxey himself. However, Maxey-Riley equation lacks the lift term that must be added to the equation in the presence of a boundary or rotational motion.

Expressions of the lift force found in the literature are not applicable to the sphere moving inside a cylindrical channel. Majority of the studies pursuing the lift force consider spherical particles subjected to Poiseuille flow or linear shear flow. As a rare

case considering the motion of a sphere in quiescent fluid, work of Rubinow and Keller [74] investigating the motion of a spinning sphere moving in a viscous quiescent fluid at low Reynolds numbers can be cited. They calculated the forces and the torques acting on the sphere and reported the presence of a lift force acting on the sphere orthogonal to its direction of translation, whose magnitude is proportional to $\omega \times \mathbf{U}$. They also argue that the lift force is independent of viscosity at small Reynolds numbers. However, due to the absence of a confinement, which is an important parameter affecting the lift force, their results are not applicable here.

Saffman [75] reported on the lift force acting on a sphere moving in a very viscous fluid and subjected to unbounded linear shear flow. He discussed the contributions to the lift force due to the shear and due to the rotation. He also derived an equation for the lift force acting on small spheres in linear shear flow, which is valid when the particle Reynolds number is much smaller than the square root of the Reynolds number based on the velocity gradient, which must be of the same order as the rotational Reynolds number. All three Reynolds numbers should also be much smaller than unity. Absence of a boundary and presence of a flow renders his results inapplicable to our case. Drew [76] reported that the wall-induced lift force on the sphere moving at low Reynolds number in a viscous flow is smaller than the lift that could be created by an unbounded shear flow, which indicates that the presence of a boundary affects the lift force acting on the sphere. Cox and Brenner [77] studied motion of particles with arbitrary shape, including spheres, and explored the effects of the presence of a boundary around the flow field. They investigated the lateral migration observed when spherical particles suspended in vertical tubes are subjected to laminar flows. The authors reported that Rubinow-Keller equation [74] does not apply to this problem, as the disturbances to flow considered by Rubinow and Keller [74] are local, and that the force Cox and Brenner calculated [77] is greater than the force calculated by Rubinow and Keller [74]. This result also underlines the contribution of the confinement to the lift force. Ho and Leal [78] calculated inertia-induced effects on rigid spheres in 2D. They concluded that such spheres settle in the middle of two bounding planes when subjected to simple shear flow, and at 0.6^{th} distance from the central axis when subjected to Poiseuille flow. The study is conducted for naturally buoyant spheres and the results are valid for spheres sufficiently away from the wall. Vasseur and Cox [79] extended this analysis to spheres subjected to Poiseuille flow and Couette flow between two flat planes, where they investigated particles that are non-

neutrally buoyant, neutrally buoyant and almost neutrally buoyant. Non-neutrally buoyant particles are observed to move towards the closest boundary if the velocity of the Poiseuille flow and the sedimentation velocity of the particle have the same sign. In Couette flow, these particles are reported to move towards the moving wall when the velocity of the flow and the sedimentation velocity of the particle have opposite signs. Equilibrium position of neutrally buoyant particles between two flat planes are reported for two cases, where the particles are allowed to freely rotate and where their rotation is prevented, and it is demonstrated that the equilibrium position of the spheres depends on the presence (or absence) of a rotary motion. For almost neutrally buoyant particles, the equilibrium position also depends on the density difference between the fluid and the particle. These results are valid for low but finite Reynolds numbers.

Distance between the spherical particle and the confinement boundary is another crucial parameter affecting the lift force. Cox and Hsu [80] considered spheres suspended in a laminar flow near a vertical wall. They observed the dependence of particle equilibrium position on the ratio of flow velocity to particle's sedimentation velocity similar to the findings of Vasseur and Cox [79] and report that their results agree with Vasseur and Cox [79] when the particle is not far from the wall. Mclaughlin [81] studied the sphere moving parallel to a flat wall in linear shear flow with Reynolds number small compared to unity. He calculated the lift force acting on such a particle and found an expression for the lift force, which is applicable when the particle is sufficiently away from the wall, complementing the findings of Cox and Hsu [80]. Cherukat and McLaughlin [82] derived a solution for the lift when the gap between the sphere and the infinite plane wall is comparable to or even smaller than the radius of the sphere in case the sphere is subjected to shear flow. The expression for the sphere rotating and translating in contact with a rigid boundary under shear flow is obtained by Krishnan and Leighton [83]. Their expression includes contributions from both ambient shear and translation-rotation coupling.

Studies on experimental observation of the lift force are scarce. Leighton and Acrivos [84] report that they could observe the lift experimentally in particles between two parallel horizontal surfaces at Reynolds numbers smaller than 0.01. They argue that even though in the low Reynolds number regime the inertial forces are dominated by the viscous forces, the inertial forces are not completely absent ant therefore could be accountable for the observed lift. Motivated by that, they studied the lift force on a

stationary sphere subjected to shear flow as the sphere is in contact with the wall. They concluded that the contribution to the lift from viscous forces are zero, and despite the fact that the lift observed in the experiments are of a magnitude that is measurable, its true nature could not be determined. Hall [85] experimentally measured the lift force on the stationary spherical particles subjected to turbulent flow near a boundary and demonstrated that the lift force measured is much greater than the lift forces calculated using existing solutions in the literature.

Some expressions on the lift force are not applicable due to the high Reynolds number flows featured in the studies. Schonberg and Hinch [86] investigated spherical particles subjected to Poiseuille flow between two infinite plates with the Reynolds number is close to unity. The authors reported that the spherical particle settles closer to the wall with an increase in Reynolds number. Lee and Balachndar's work [87], which is one of the most recent studies, also analyzed the sphere moving near a flat boundary under linear shear flow for a Reynolds number range between 1-100.

1.2. Motivation

Understanding the swimming characteristics of micro swimmers in low Reynolds number environments is crucial to the success and accuracy of medical applications that will utilize them. The number of studies featuring chiral and axisymmetric swimmers increase at an immense rate. However, there are still many aspects that need to be analyzed in great depth to grasp their potentials and shortcomings and design applications that could possibly exploit both the advantages and shortcomings.

Both chiral and axisymmetric particles can be made to break time reversal symmetry that is explained in the Scallop Theorem [88] in many ways. Chiral structures achieve asymmetry due to their geometry, and axisymmetric particles can be modified to produce asymmetric flows around them, interact with boundaries or go through surface deformations. To have a grasp of the entirety of the field covering micro swimmers, one must investigate both types of structures, and then utilize the one that fits a certain

application better. Therefore, researchers should attempt filling any gap of knowledge in the field.

This thesis work attempts to treat two aspects of micro swimmers that needs to be studied further. Firstly, effects of geometric parameters on the velocity and efficiency of the chiral structures such as helices and ribbons are investigated. Swimming performance of confined chiral structures depend on various geometric parameters. Manufacturing intricate structures at small scales with desired geometric proportions is hard; it is time and money consuming and requires great expertise. One may not always be able to acquire the dimensions desired due to the limitations of the techniques available. For example, one may have to produce a helix of a certain width, which might decrease its velocity performance. Having a guideline in such a case would allow a researcher to enhance the velocity by modifying another geometric parameter, such as width. Furthermore, having a computational tool that could analyze the resulting geometry prior to manufacture could help reduce the cost in both time and money.

Secondly, an alternative to chiral structures is presented by mobilizing a rigid sphere inside cylindrical conduits. Helical structures convert rotational motion to linear translation; therefore, they are very important in micro swimming applications. Spherical particles, with their axisymmetric geometry, cannot be mobilized easily in bulk fluids. At low Reynolds number, they cannot swim in bulk by rotary motion due to the lack of a non-reciprocal motion. They can be pulled by an external force, but the linear drag acting on spherical particles is proportional to the length scale, whereas the rotational drag on the sphere is proportional to the third power of the length scale, which makes a significant difference at small scales. However, it is possible to mobilize spherical particles via rotary motion by introducing asymmetric forces using hydrodynamic interactions between the spherical particles and confinements. Once the obstacle of moving them effectively is overcome, spherical particles become advantageous for they are much easier to produce, and they can be very easily miniaturized to fit the application. Therefore, it is important to understand their swimming behavior inside confinements. Swimming of spherical particles inside cylindrical channels is not observed experimentally at great length. Therefore, in the second part of this thesis, an experimental study identifying swimming modes of the magnetically actuated spheres inside cylindrical conduits is conducted. The experimental results show that a simple, chemically inactive axisymmetric particle can also be manipulated to follow trajectories and even be focused non-inertially. A numerical

model to predict their trajectories is also prepared. As stated above for helices, being able to analyze the system while designing it has great advantages.

Combination of the two parts of the thesis construct a comprehensive study of swimming performance of micro swimmers in cylindrical conduits regardless of their shape (chiral vs. axisymmetric). Both parts are applicable to micro swimmers in low Reynolds number environments and present computational tools to understand and analyze their swimming behavior. Furthermore, both of these tools can be used to analyze shapes that are not in the scope of this thesis with minor modifications. Lastly, the results of each study deliver novel insights to the field.

2 SWIMMING OF HELICAL STRUCTURES

In this chapter, effects of geometric parameters on the swimming performance of helical rods, ribbons, filaments and Archimedean screws are demonstrated; wavelength, amplitude, radius and eccentricity (for rods), confinement radius, helix thickness and width (for ribbons and screws) are included in the study. A CFD model is developed to obtain the swimming velocity, torque, angular velocity, and efficiency of the helical structures inside circular channels. First, the helical rods are discussed and the swimming velocities are compared with the SBT [32], which does not include the wall effects, and APS [33], which includes the wall effects only for small amplitudes of the helix. Comparisons also serve as a validation of the model with theoretical results. Then, ribbons and screws are discussed to demonstrate the effects of thickness and width for the structures with rectangular cross-sections. Ribbons are of particular interest due to advantages of bulk-micro manufacturing techniques in mass production of such structures, as demonstrated by Zhang *et al.* [23] with the "self-scrolling helical ribbon." Effects of ribbon width are compared for the ribbons attached to a magnetic head and coated with magnetic materials. Resistance coefficients are obtained for the full experimental swimmer [23] with a head attached to the finite length tail, and compared with the experimental values and previous numerical results [35, 41, 43] as a validation and to understand the effects of the swimmer geometry. Resistance coefficients for the helical structures studied in the scope of this work are also reported and used in the interpretation of the velocity and efficiency profiles of these structures.

A fraction of the data reported in this chapter are previously published by Demir and Yeşilyurt [89].

2.1. Methodology

2.1.1. CFD Model

In this section, governing equations and boundary conditions applied in the CFD model are presented. Mesh convergence analysis of the model is conducted, and the process followed in obtaining the resistance coefficients and their validation is explained.

2.1.1.1. Governing equations and boundary conditions

Low Reynolds number swimming of helical structures is governed by incompressible Stokes equations which is given in the non-dimensional form as follows

$$-\nabla p + \frac{1}{Re}\nabla^2 \mathbf{u} = 0 \quad \text{and} \quad \nabla \cdot \mathbf{u} = 0 \tag{1-2}$$

where $\mathbf{u}$ and p denote the velocity vector and pressure respectively. The Reynolds number, Re, is based on the rotation frequency, f, and a length scale, ℓ, such as the diameter of the channel: i.e. $Re = \rho\ell^2 f/\mu$, where ρ is the density and μ is the viscosity of water.

No-slip boundary conditions are used on the stationary channel wall and on the helical body moving with the velocity:

$$\mathbf{u} = \mathbf{U} + \mathbf{\Omega} \times (\mathbf{r} - \mathbf{r}_0), \quad \mathbf{r} \in S \tag{3}$$

where $\mathbf{U}$ is the swimming velocity, $\mathbf{\Omega}$ is the angular velocity, $\mathbf{r}$ is the position, $\mathbf{r}_0$ is the position of the centroid, and S represents the surface of the structure. Lateral and angular velocities of the helical body are specified as unknown, except for the angular velocity of the helix in the direction of its axis, $\omega = 2\pi$, which is kept constant in constant-ω

simulations, but remained unknown in the constant torque, T, case. Force-free and torque-free swimming conditions are used to calculate the unknown velocity components:

$$\mathbf{F}_{net} = \int_S \boldsymbol{\sigma} \cdot \mathbf{n} \, dA = 0 \tag{4}$$

$$\mathbf{T}_{net} = \int_S (\mathbf{r} - \mathbf{r}_0) \times \boldsymbol{\sigma} \cdot \mathbf{n} \, dA - \begin{bmatrix} T \\ 0 \\ 0 \end{bmatrix} = 0 \tag{5}$$

where $\boldsymbol{\sigma}$ is the stress tensor and $\mathbf{n}$ is the local surface normal.

Swimming of an infinite helical body inside a circular channel is modeled by using periodic velocity and stress at the inlet and outlet of the one-wavelength long part of the fluid domain in the channel:

$$\{\mathbf{u}, \boldsymbol{\sigma}\}_{x=0} = \{\mathbf{u}, \boldsymbol{\sigma}\}_{x=\lambda} \tag{6}$$

A relative metric is specified to assess the efficiency of helical structures with respect to the base cases in Table 1. For helical rods, the base case is defined arbitrarily, but for helical ribbons and screws the ribbon manufactured by Zhang *et al.* [23] is used as the base case. Since the rate of work to move an object at the swimmer speed is proportional to $\mathbf{U} \cdot \mathbf{U}$ and the required power is $\mathbf{T} \cdot \boldsymbol{\Omega}$, the relative efficiency is independent of the angular velocity or the torque input studies and defined follows:

$$\frac{\eta}{\eta_0} = \frac{\mathbf{U} \cdot \mathbf{U}}{\mathbf{T} \cdot \boldsymbol{\Omega}} \frac{\mathbf{T}_0 \cdot \boldsymbol{\Omega}_0}{\mathbf{U}_0 \cdot \mathbf{U}_0} \tag{7}$$

Mobility coefficient for the low Reynolds Number swimmer prescribes the forward velocity of the swimmer for a given torque in that direction as a convenient metric for comparing the effects of geometric parameters of the swimmer. Similar to the relative efficiency, the mobility coefficient is normalized with the reference case:

$$\frac{m}{m_0} = \frac{U}{T} \frac{T_0}{U_0} \tag{8}$$

2.1.1.2. Simulation parameters

Swimming velocity, U, and efficiency, η, (7) of helical structures are obtained from the solution of governing equations (1)-(2) subject to boundary conditions (3)-(6) with the finite-element-method using COMSOL® Multiphysics [90]. Representations of helical bodies with circular and rectangular cross-sections are shown in Figure 2.1, where the geometric parameters are also depicted.

In order to identify the physical effects of geometric variables and to obtain sensitivities, parametric studies are carried out with respect to each geometric variable while others are kept at their base value unless noted otherwise. For the rods, the length scale is set to 100 μm for which the Reynolds number is 8.3×10^{-3} for swimmers in water. Wavelength, λ, and amplitude, B, of the helix, radius of the rod, a, and eccentricity of the helix, z_0, and the diameter of the channel, $2R_{ch}$, is used for the nondimensionalization of length scales. For ribbons, filaments and screws, dimensional values are adapted from the helical ribbon developed by Zhang *et al.* [23]. In addition to effects of λ and R_{ch}, thickness, d, and width, w, are studied and B is used for the nondimensionalization of the length scales. Complete list of geometric parameters and their range of values are given in Table 2.1. Since the velocities scale linearly with the frequency, it is kept at the base value of 1 Hz for all cases.
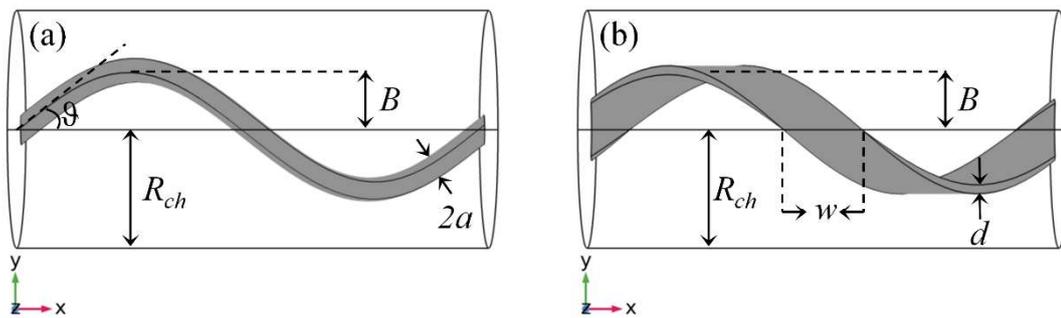
Figure 2.1 (a) Right-handed helical rod with a circular cross-section of diameter $2a$; (b) Helical ribbon with thickness d and width w.

Table 2.1 Base values and test ranges of geometric parameters.

Parameters	Helical rod		Helical ribbon		
	Base Value	Range	Dimensions based on Ref [23]	Base Value	Range
Wavelength, λ (= L_{ch})	1	0.1 - 10	11.04 μm	7.89	0.33-20
Amplitude, B	0.1	0.01 - 0.45	1.4 μm	1	constant
Channel radius, R_{ch}	0.5	constant	-	2	1.1-10
Radius, a	0.04	0.01 - 0.35	-	-	-
Eccentricity, z_0	0	0 - 0.35	-	0	constant
Length scale, ℓ	0.1 mm	-	1.4 μm		-
Frequency, f	1 Hz		1 Hz		
Reynolds number, Re	8.3×10^{-3}	-		1.63×10^{-6}	-
Thickness, d_0	-	-	42 nm	0.03	0.01-1.95
Width, w_0	-	-	1.8 μm	1.29	0.01-7.71

2.1.1.3. Mesh convergence

The CFD model uses P1-P1 type tetrahedral finite elements and brick elements in double boundary layer mesh around the helix and on the channel wall in cases where the helix is very close the channel wall as shown in Figure 2.2

Convergence of the mesh is demonstrated on the base configuration chosen for helical rods (Table 2.2). Linear system of equations is solved with the PARDISO solver, on a high-end workstation. The swimming velocity, CPU time, memory allocation and the discrepancy relative to the finest mesh are presented in Table 2.2. It is observed that the velocity converges to the reference velocity as the DOF increases even with about 25K DOF and further improvement in the mesh does not improve the results. The error in the swimming velocity increases as the element size increases and the number of DOF decreases. The base mesh, which is adopted in this study, has 253K DOF (Figure 2.2), yields a swimming velocity with 0.16% error in significantly lower CPU time with reasonable memory requirement (Table 2.2).

The same mesh-size combination for automatic triangulation of surfaces and generation of tetrahedrals is used for the ribbons as well and mesh convergence is observed (Figure 2.3). For helices with much smaller dimensions than the base ribbon, such as the ribbon with the smallest thickness ($d = 0.01$) and 200K-DOF mesh (Figure 2.4), and the filament with the width and thickness of $d = w = 0.03$ and 400K-DOF mesh (Figure 2.5), error in the velocity is less than 0.35% compared to the finest mesh with more than one million DOF for each case.
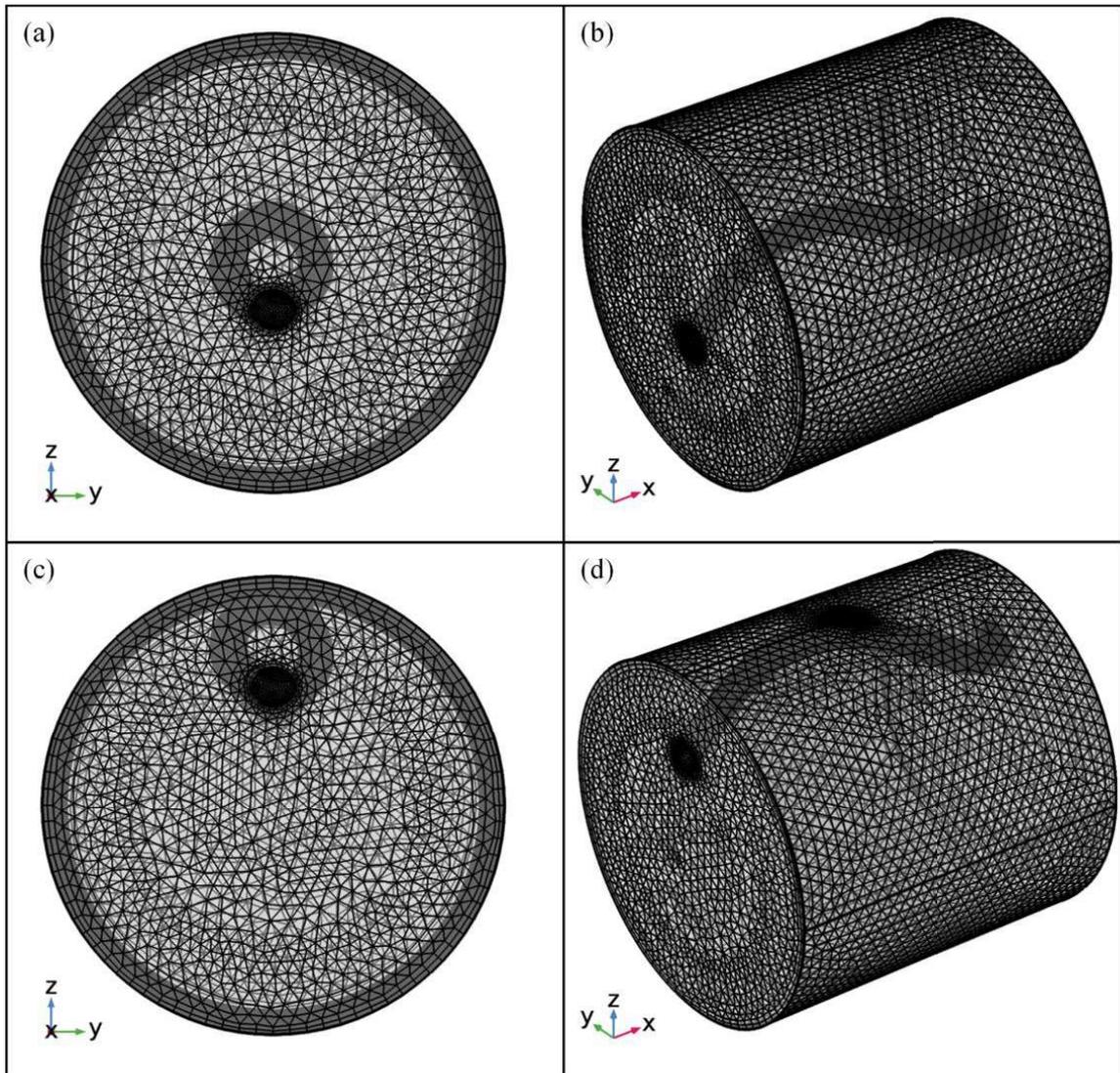
Figure 2.2 Finite-element meshes for the reference case (a) and (b); mesh refinement at the surface for the eccentric swimmer (c) and (d).

Table 2.2 Convergence of the finite-element mesh for the base structure.

Number of DOF	U	CPU Time (mm:ss)	RAM (GB)	Error (%)
1096845	0.16697	26:40	65.45	Reference
757096	0.16728	12:08	39.5	+ 0.19
407102	0.16623	03:18	17.7	- 0.44
253761	**0.16724**	**01:31**	**10.53**	**+ 0.16**
120590	0.16708	00:24	5	+ 0.07
69439	0.16540	00:08	4.31	+ 0.94
43758	0.16540	00:05	3.6	+ 0.94
34622	0.166179	00:04	3.05	+0.47
25900	0.16866	00:03	2.83	-1.01
20148	0.170136	00:02	2.95	-1.9
19704	0.171465	00:02	2.94	-2.69
18576	0.175954	00:02	2.89	-5.38
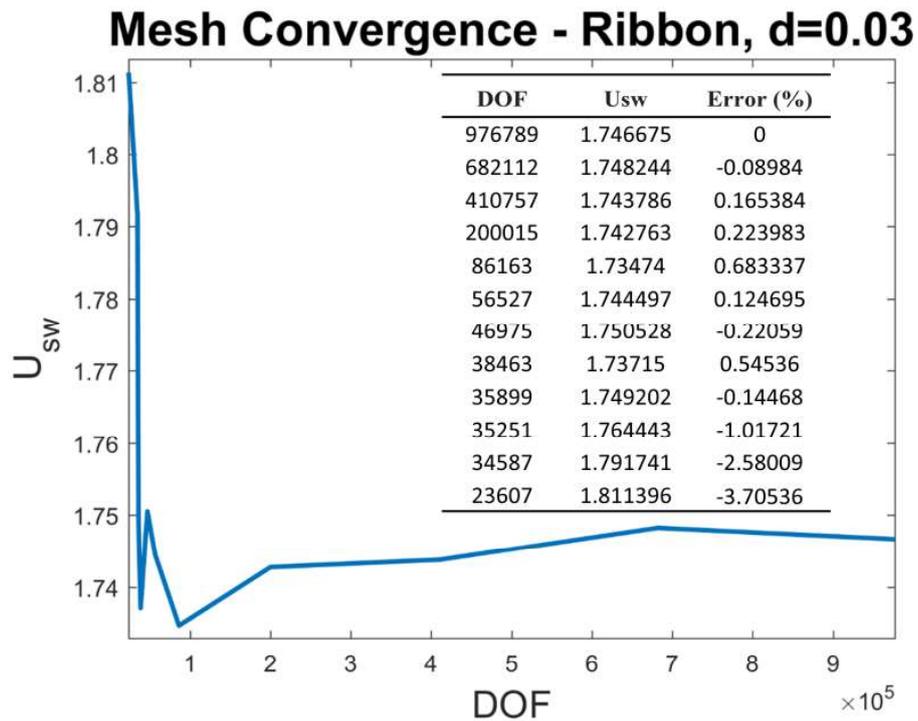
Figure 2.3 Convergence of the finite-element mesh for the ribbon.

Mesh Convergence - Ribbon, d=0.01

DOF	Usw	Error (%)
1328786	1.707421	0
726827	1.709896	-0.14493
490661	1.708094	-0.03944
248016	1.713329	-0.34602
136921	1.713744	-0.37033
108894	1.723313	-0.93077
103916	1.724065	-0.97479
101906	1.730763	-1.36707
96858	1.735584	-1.64943
73354	1.742062	-2.02886
72762	1.745359	-2.22193
70194	1.747224	-2.33119
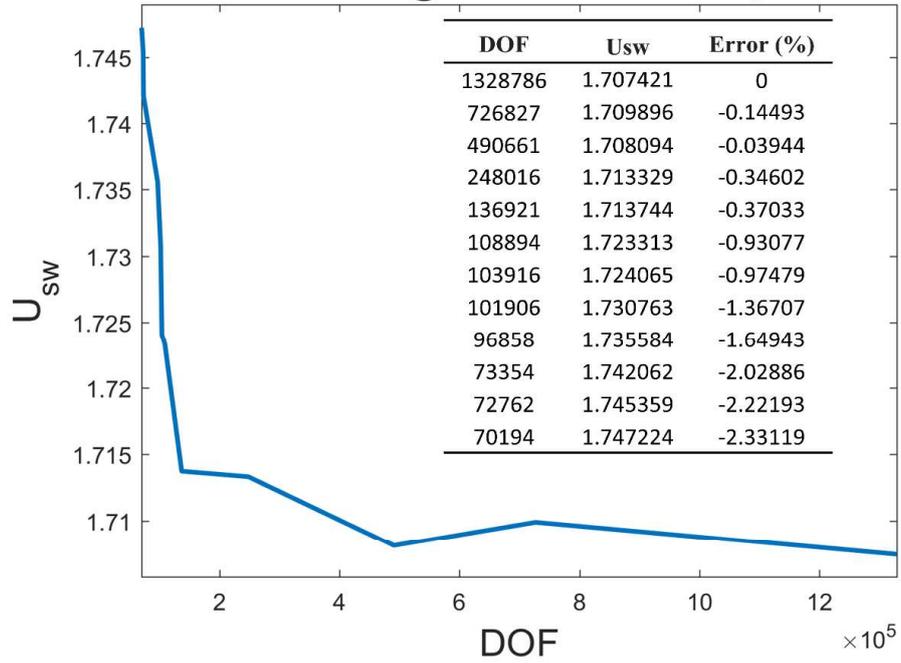
Figure 2.4 Convergence of the finite-element mesh for the ribbon with minimum thickness.

Mesh Convergence - Filament, d=w=0.03

DOF	Usw	Error (%)
968549	2.402004	0
668189	2.403177	-0.04884
401409	2.396871	0.21368
259973	2.4042	-0.09143
182549	2.420257	-0.75994
68125	2.429708	-1.15338
37493	2.459482	-2.39292
27665	2.480499	-3.26792
19073	2.500915	-4.11785
16973	2.512555	-4.60246
15977	2.558854	-6.52998
15765	2.558782	-6.52698
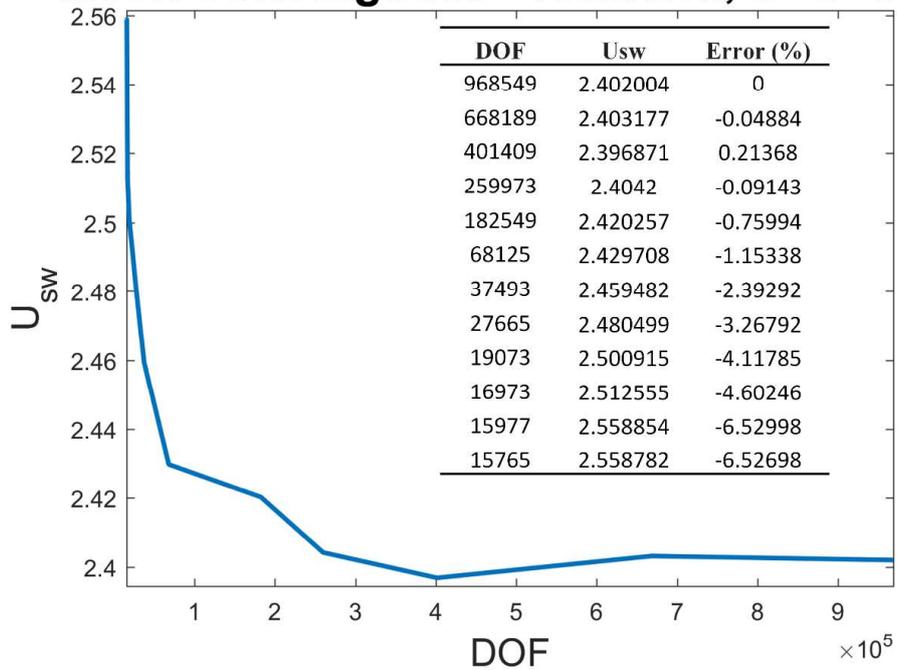
Figure 2.5 Convergence of the finite-element mesh for the filament.

2.1.1.4. Validation of resistance coefficients

Zhang *et al.*[23] provide the resistance coefficients for the experimental swimmer, which describe the relationship between the velocities and forces according to the following relationship:

$$\begin{bmatrix} F \\ T \end{bmatrix} = \begin{bmatrix} R_a & R_b \\ R_b & R_c \end{bmatrix} \begin{bmatrix} U \\ \omega \end{bmatrix} \tag{9}$$

In (9), the coefficient R_a describes the drag experienced by the swimmer due to its translation, R_b is the resistance between the translational speed and the torque, or the angular velocity and the force, and R_c represents the rotational drag.

Previous theoretical [35] and numerical studies [41, 43] report discrepancies in the resistance coefficients as shown in Table 2.3, in part due to uncertainties in the dimensions of the experimental ribbon [43]. Koens and Lauga [35] report results from the analysis based on the slender ribbon approximation for the same swimmer with a spheroid head. Whereas numerical results with BEM are reported by Keaveny *et al.* [43] for a 49.7 microns long swimmer with a payload attached, and RiBEM results are reported presented by Montenegro-Johnson *et al.* [41] for the swimmer with 1.4 microns of helical radius and 38 microns axial length with a magnetic head of the same dimensions as the experiments. Here, resistance coefficients of the swimmer are obtained from the CFD model of the exact swimmer in Ref. [23] placed inside a large channel with a radius and length about ten times the length of the swimmer with closed ends. Consistently with previous theoretical and numerical work, the length of the helical tail is set to 38 μm, radius of the helix is taken 1.4 μm, and a magnetic head of dimensions 4.5 μm x 4.5 μm x 200 nm (referred to as "large head" in Ref. [23]) is attached to the helical tail.

According to Table 4, R_a, which represents the translational resistance, is lower than the experimental value for all methods; however, the CFD result lies between the experimental and numerical results. In the CFD model, R_a approaches to the experimental value as the radius of the channel is increased to mimic bulk swimming conditions. Moreover, according to simulations, coupling coefficient R_b is sensitive to the position of the magnetic head: as the centerline of the head deviates from the centerline of the helix,

R_b increases. The CFD result for R_b is for the case when the centerlines overlap. Lastly, R_c values, that represents the rotational drag, from numerical studies are about 4 to 5 times as large as the experimentally reported value. According to CFD results the value of the R_c decreases as the helix diameter increases as also reported by [35].

Table 2.3 Values of the resistance coefficients from experimental and numerical studies.

	Experimental [23]	CFD	SRT [35]	BEM [43]	RiBEM [41]
R_a [10^{-7} N s m^{-1}]	1.5	1.28	1.04	0.937	0.932
R_b [10^{-14} N s]	-1.6	-1.75	-1.32	-1.63	-1.47
R_c [10^{-19} N m s]	2.3	11.81	6.81	10.1	9.91

2.2. Results

In this section, results obtained from the CFD model are presented. First, the circular cross-sections will be considered. Results for these will also be validated using existing theoretical models. Then the results for the ribbons and screws are presented. The results regarding these are validated by the resistance coefficients reported by Zhang et al. [23].

2.2.1. Circular Cross-Sections

Swimming performance of the helical rods are investigated for constant angular velocity application. Results are presented in this section categorized by the geometric parameter in focus.

2.1.1.1. Wavelength

For constant rotation rate, $\omega = 2\pi$, swimming velocities from CFD simulations are compared against theoretical results from the slender body theory [32] (SBT) and the approximate perturbative solution [33] (APS). The effect of the wavelength, λ, on the swimming velocity, U, is shown in Figure 2.6a. First, U increases with λ up to a peak value, then decreases. For small (large) wavelengths, the pitch angle of the helix is very large (small) and thus there is not enough propulsion from the drag anisotropy as observed in previous studies as well, e.g. [91]. Second, CFD results agree with SBT and APS asymptotically at small and large wavelengths respectively. Former captures the overall trend in the swimming velocity but agrees with the CFD results only for small λ values, as the theory is based on the force distribution and interactions over a slender body and does not account for the confinement. On the other hand, APS is more accurate at large wavelengths as expected, since the analysis addresses the swimming of cylindrical rods with helical perturbations in circular channels; as λ increases, helical shape approaches to the perturbative limit. In between the two extremes, body-body and body-wall hydrodynamic interactions act together.

Relative external torque, T/T_0, that sustains the rotation of the helical rod at $\omega = 2\pi$ is shown in Figure 2.6b. Except for small wavelengths, T/T_0 increases almost linearly with λ according to CFD simulations. However, the T/λ saturates to a constant value as λ increases following a decline at small λ as shown in Figure 2.6c.
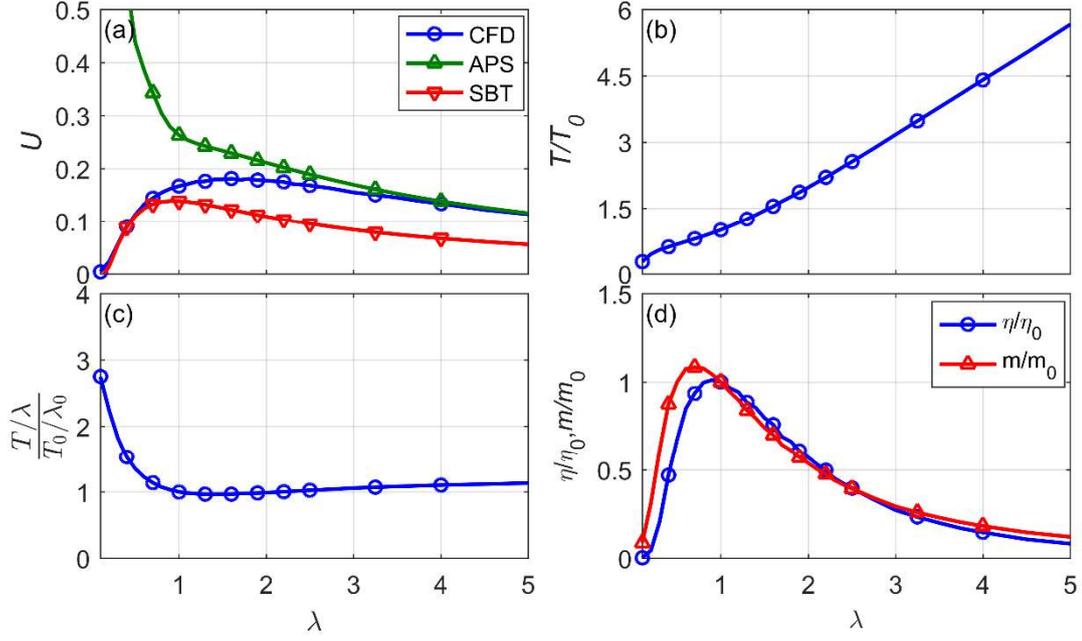
Figure 2.6 Effect of the wavelength, λ, on the swimmer velocity, U (a), torque (b), torque per wavelength (c), and efficiency & mobility (d).

Optimum wavelengths that maximize the efficiency and the mobility are slightly different (Figure 2.6d). For constant ω, the efficiency can be written as the mobility multiplied by the velocity, thus we observe that mobility peaks at a lower λ than the efficiency, $\lambda = 0.7$ vs. 0.9, where η/η_0 becomes slightly larger than unity.

The results can be interpreted with the help of resistance coefficients. Resistance coefficients R_a, R_b, and R_c are non-dimensionalized as follows, and depicted in Figure 2.7:

$$\bar{R}_a = R_a / (6\pi\mu B) \tag{10a}$$

$$\bar{R}_b = R_b / (\pi B^2) \tag{10b}$$

$$\bar{R}_c = R_c / (8\pi\mu B^3) \tag{10c}$$

Translational resistance coefficient $\bar{R}_a$ increases with increasing wavelength, which is expected to cause a drop in the translational velocity. However, this effect is counteracted by the increase in the magnitude of the translation-rotation coupling resistance $\bar{R}_b$. The increase in $\bar{R}_c$, which is the rotational resistance coefficient, is apparent in the increasing amount of torque required to turn the helix as the wavelength increases.

When the net force on the swimmer is zero, nondimensional form of equation 9 reduces to:

$$\overline{U} = -\frac{\overline{R}_b}{\overline{R}_a}\overline{\omega} \tag{11}$$

which allows predicting the velocity profile using the resistance coefficients. At constant rotational velocity and under zero net force, lateral velocity of the helical rod is proportional to negative of the ratio of translation-rotation coupling coefficient to the translational resistance coefficient as observed in Figure 2.8, which shows an identical trend to the velocity profile observed in Figure 2.6a.
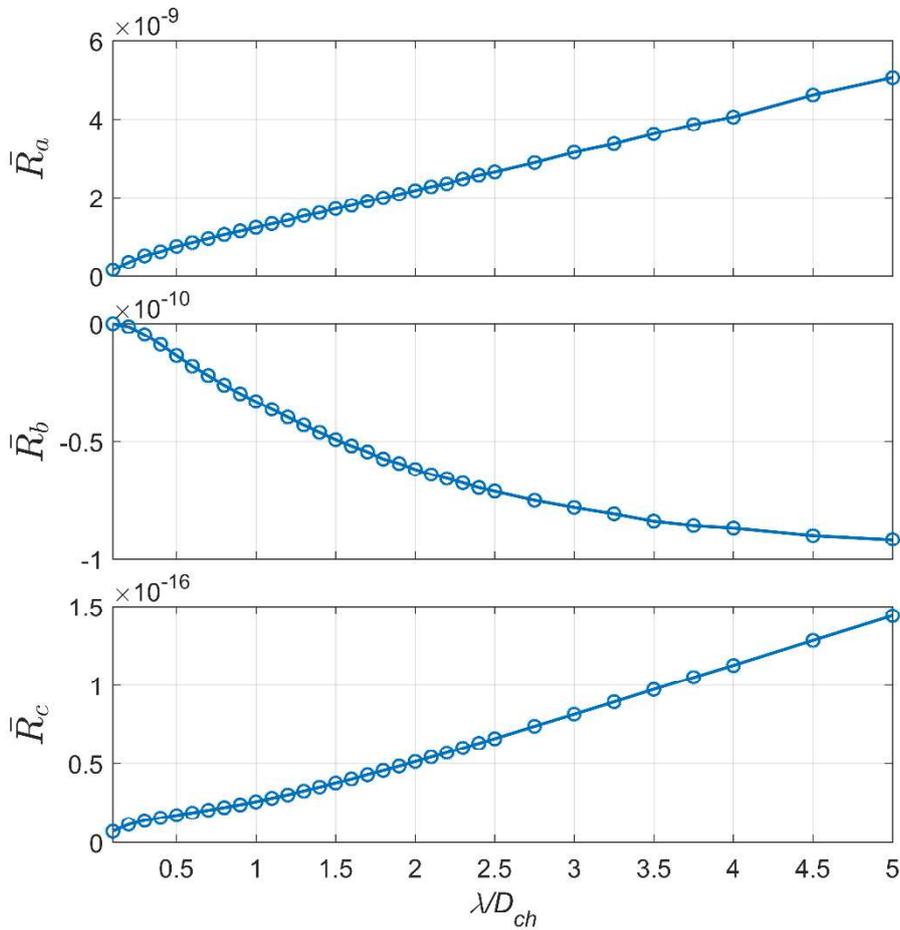
Figure 2.7 Translational, translation-rotation coupling, and rotational resistance coefficients plotted against normalized wavelength λ/D_{ch}.

$-\bar{\omega}(\bar{R}_b/\bar{R}_a)$

λ/D_{ch}
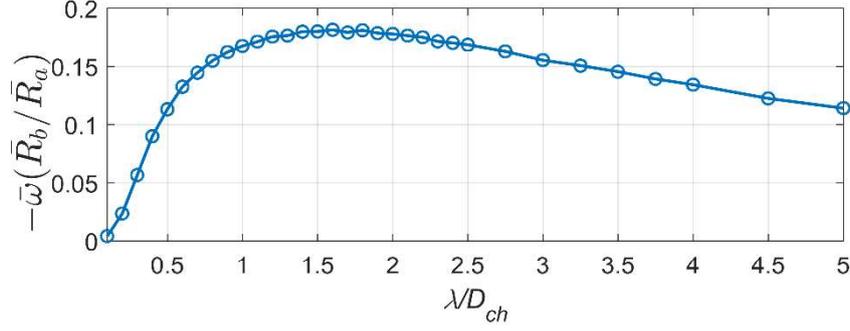
Figure 2.8 Velocity profile with respect to the changing wavelength, obtained using the resistance coefficients.

2.1.1.2. Rod Thickness

The effect of the rod thickness, a, on the swimming velocity, U, is shown in Figure 2.9a. First, U varies moderately with a, and goes through a minimum at $a = 0.15$. Increase in U becomes more notable as a increases further; for $a = 0.35$, U is almost twice as high as its minimum value. As $a \to 0$, U converges to a non-zero value, which agrees with the SBT, and that is slightly greater than the velocity of the base helix. Agreement with the SBT theory indicates that wall interactions do not play an important role as $a \to 0$. Moreover, the offset between the CFD and the APS remains significant due to relatively large amplitude of the base helix, $B = 0.1$, that violates the assumptions of APS.
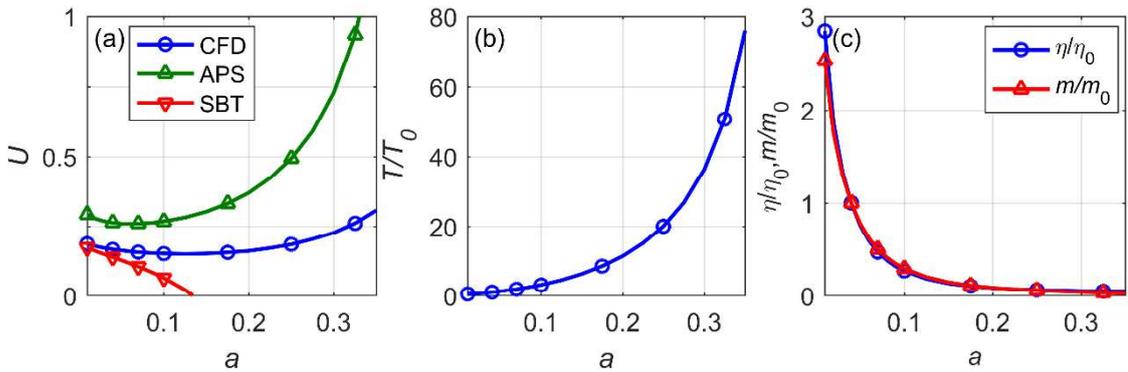
Figure 2.9 Effect of the radius of the rod, a, on the swimmer velocity, U (a), normalized torque (b), normalized efficiency and normalized mobility (c).

As *a* increases, torque needed to rotate the helical rod at a constant angular velocity increases dur to the increased perimeter of the helical structure. Furthermore, the clearance between surfaces of the channel and the helix, *c*, decreases and leads to increase in the shear stress proportionally to 1/c, thus the required torque increases as well (Figure 2.9b). Due to increasing torque, efficiency and the mobility of the helical rod decrease sharply as *a* increases as shown in Figure 2.9c. The two are almost identical since the velocity does not change dramatically and the sensitivity of *U* is very small, i.e. $|\partial U/\partial a|$ ~ 0. Thus, for effective helical swimming, the rod diameter must be kept as small as possible to reduce the torque requirement and increase the overall efficiency and mobility.

Similar to the case of increasing wavelength, $\overline{R}_c$ increases with increasing thickness, effect of which is observed in the increasing torque demand (Figure 2.10). $\overline{R}_b$ and $\overline{R}_a$ increase in magnitude, but they do so at different rates, thus a minimum velocity is observed ((Figure 2.10). Figure 2.11 shows the velocity profile obtained using the resistance coefficients and equation 11, which is observed to be identical to the profile seen in Figure 2.9a.
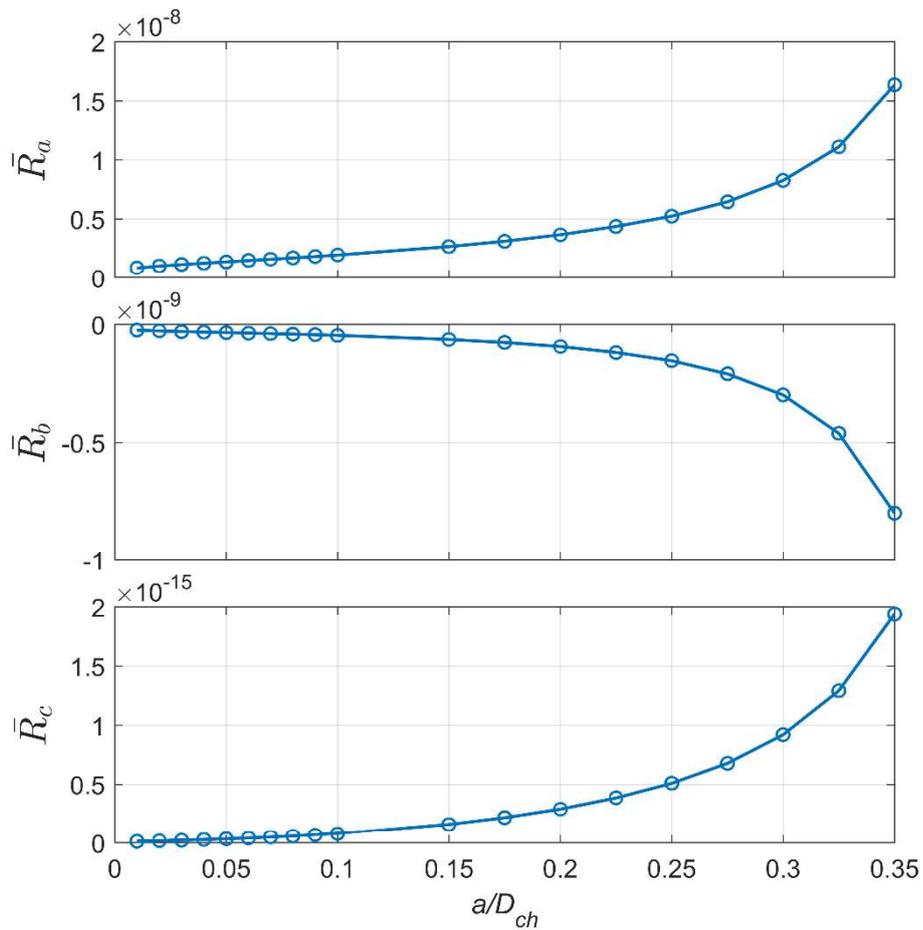
Figure 2.10 Translational, translation-rotation coupling, and rotational resistance coefficients plotted against normalized rod thickness a/D_{ch}.
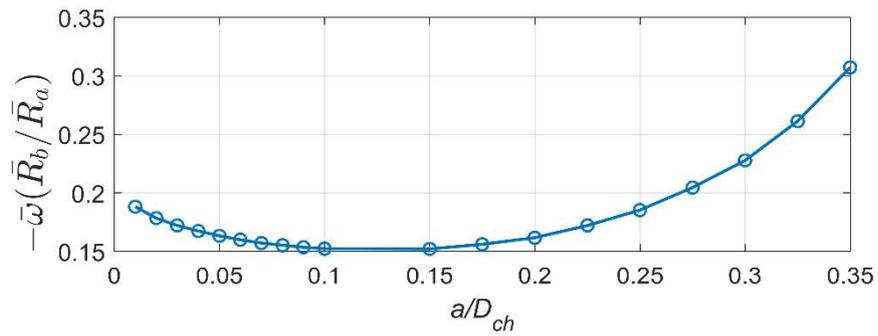
Figure 2.11 Velocity profile with respect to the changing rod thickness obtained using the resistance coefficients.

2.1.1.3. Helix Radius

As shown in Figure 2.12a, U reaches its maximum value when B is about 0.43, or when the rod is very close to the wall, i.e. $c = 1/2 - B - a = 0.03$. For small amplitudes, theoretical results are very close to CFD results as both theories predict that the swimming velocity would be zero as $B \to 0$. However, as shown in Figure 2.12b for $B < 0.05$, U from the CFD model is closer to the APS than SBT, as the wall interactions are more important in this asymptotical limit.

For small values of B, torque increases slowly (Figure 2.12c) as B increases. However, as the helical rod approaches to the channel wall, required torque to sustain constant rate of rotation increases sharply to overcome the shear on the body near the wall, which grows with inverse clearance, $1/c$. Efficiency peaks around a moderate amplitude, $B = 0.15$ (Figure 2.12d), when the rod is sufficiently away from the channel wall, and the relative mobility peaks at $B = 0.09$ with a value only slightly over unity. Therefore, amplitudes in the range of 0.1 to 0.25 are beneficial from efficiency point of view, but mobility-wise optimal B is about 0.1.
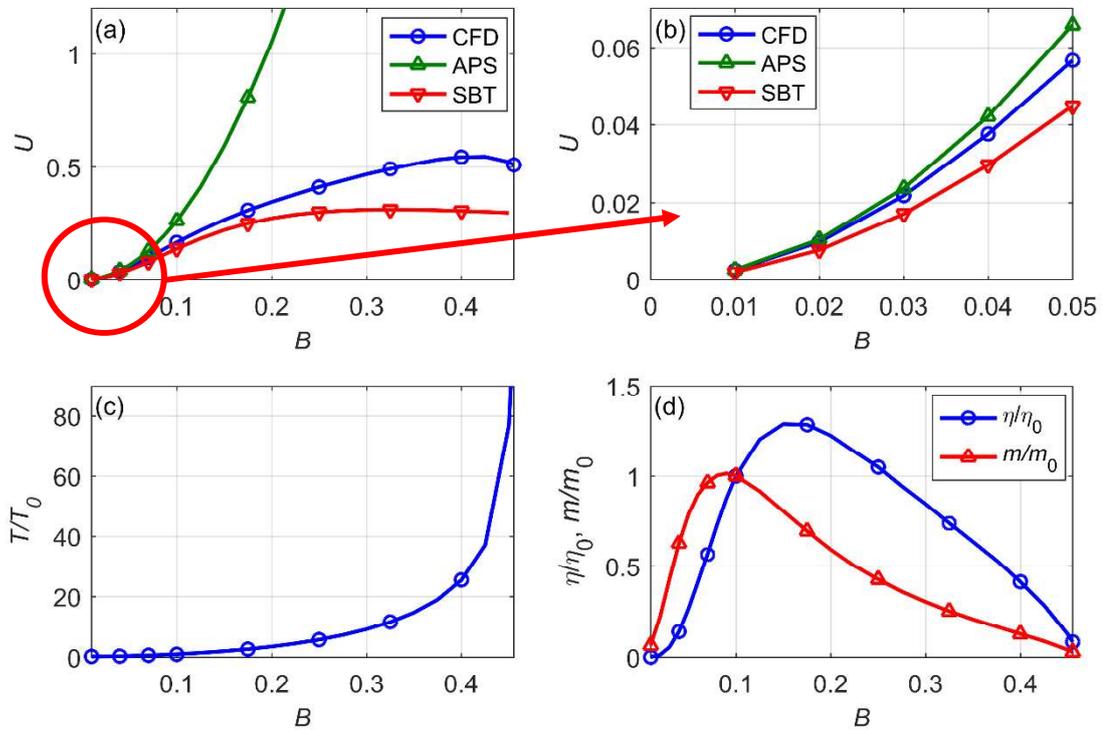
Figure 2.12 Effect of the helical amplitude, B, on the swimming velocity, U (a-b), normalized torque (c), normalized efficiency and normalized mobility (d).
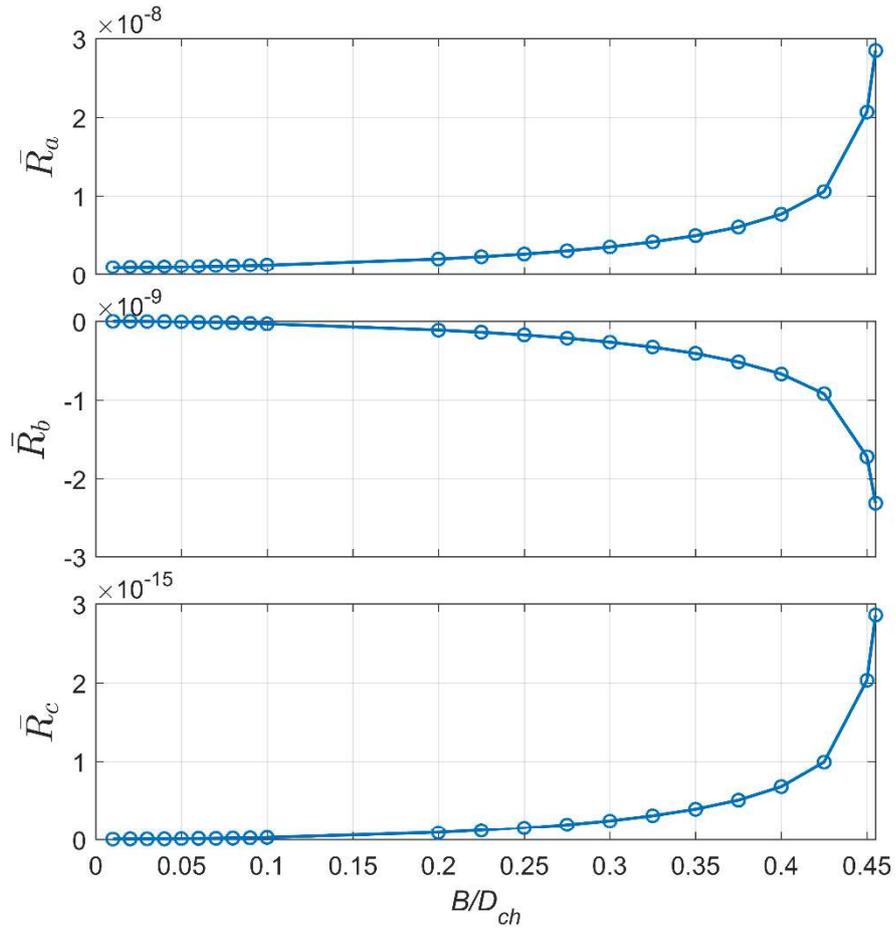
Figure 2.13 Translational, translation-rotation coupling, and rotational resistance coefficients plotted against normalized helix radius B/D_{ch}.
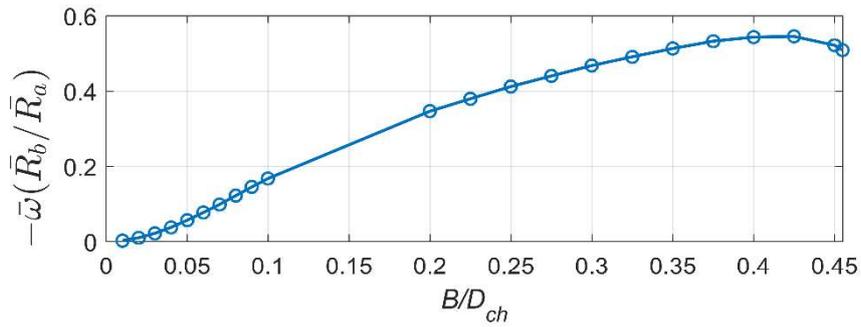
Figure 2.14 Velocity profile with respect to the changing helix radius, obtained using the resistance coefficients.

Resistance coefficients calculated for increasing values of B show remarkably similar trends to the coefficients calculated for increasing a values however, all resistance coefficients are observed to be of higher magnitudes (Figure 2.13). Increase in the torque

requirement with increasing B is captured by the increase in the rotational resistance coefficient $\overline{R}_c$ (Figure 2.13). $\overline{R}_a$ and $\overline{R}_b$ both increase in magnitude (Figure 2.13) but the difference in their rate of increase produces a velocity profile with a peak around $B = 0.43$ is observed as depicted in Figure 2.14.

2.1.1.4. Eccentricity

Helical rod is placed with an offset, z_0, from the center of the channel in CFD simulations. In Figure 2.15a, swimming velocity, U, follows an increasing trend as the helical rod gets closer to the channel wall. Due to eccentricity in the **z**-direction, a slight change in the lateral velocity in the **y**-direction, V, is also observed (Figure 2.15a). The swirling flow due to the rotation of the body inside the circular channel exerts a force on the body itself in the counter-clockwise direction such that a force-free body would orbit around the center of the channel. Thus, at a fixed position, z_0, in the **z**-direction, a negative **y**-velocity, V, is observed for small z_0 values. Moreover, for larger values of z_0 the traction force from the rotation of the body overcomes the push from the swirling flow and the lateral velocity changes direction. Increase in the torque is not very sharp as the helical rod approaches to the wall as shown in Figure 2.15b due to counteracting forces that lead to changing direction of the lateral velocity. Further increase in z_0 results in sharply increasing torque. Efficiency increases as the helical rod is set closer to the wall and decreases sharply when the swimmer is too close to the wall as shown in Figure 2.15c, with a peak around $z_0 = 0.325$ (Figure 2.15c). Mobility increases very slightly as z_0 increases but drops sharply near the wall.

Increase in the coupling resistance coefficient $\overline{R}_b$ with increasing z_0 indicates that the helical rod obtains better traction due to its increased proximity to the wall (Figure 2.16). Due to this increased contribution to lateral velocity, velocity profile depicted in Figure 2.17 shows that the rod achieves higher velocities when it swims near the wall.
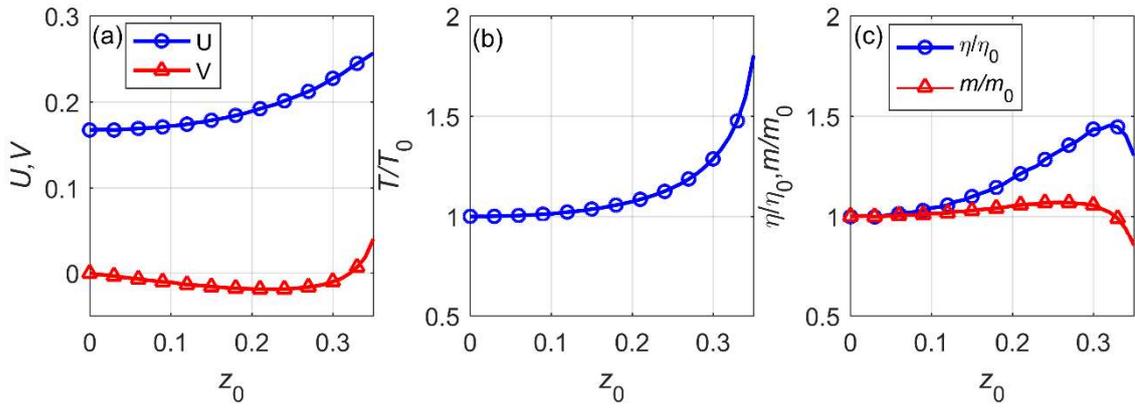
Figure 2.15 Effect of eccentricity on the velocity U and on the lateral velocity in the y-direction, V (a), normalized torque (b), normalized efficiency and normalized mobility (c).
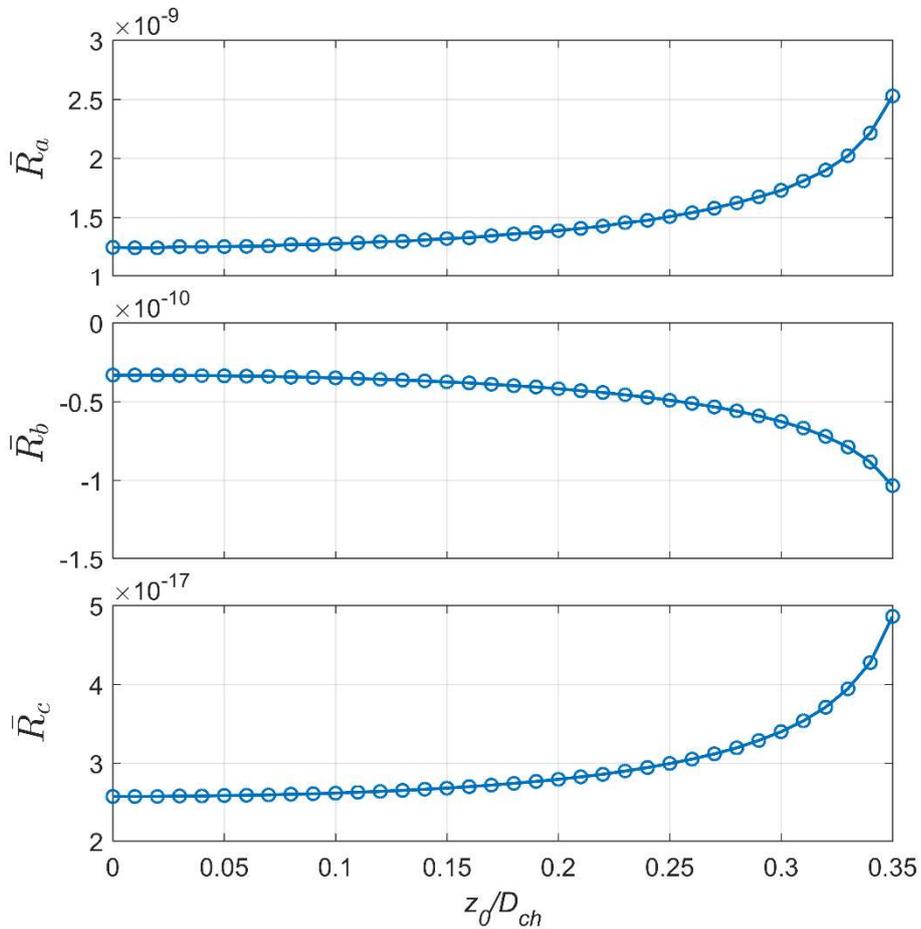

Figure 2.16 Translational, translation-rotation coupling, and rotational resistance coefficients plotted against normalized eccentricity z_0/D_{ch}.
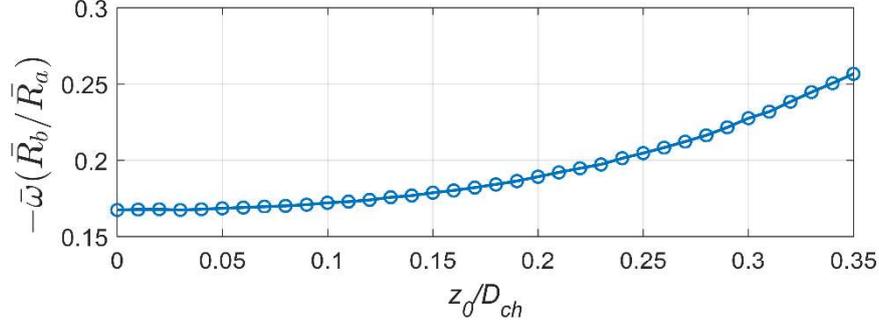
Figure 2.17 Velocity profile with respect to the changing eccentricity, obtained using the resistance coefficients.

2.2.2. Rectangular Cross-Sections

In lengths of 10-100 μm, micro swimming robots can offer great advantages in medical procedures in the circulatory system [5, 6]. At those scales, bulk micro-manufacturing techniques favor production of helical structures with a width, *w*, much larger than its thickness, *d*, as demonstrated by Zhang *et al.* [23]. Understanding of the effects of the geometric parameters on the swimming velocity and torque, bears importance on the optimal design of such artificial flagella. Geometric parameters of the helical ribbon are shown in Figure 2.1b and their base values are provided in Table 2.1. Moreover, in addition to ribbons with $d \ll w$ based on the definitions in Figure 2.1b, thin filaments with $d = w \ll B,$ and Archimedean screws with $d \gg w$ are also included in this study for the sake of completeness.

Helical swimmers are actuated typically by a rotating magnetic field that exerts a magnetic torque either on the magnetic head as demonstrated by [23], or on the whole tail, which is coated by a magnetic material as demonstrated by [19]. First method implies that the applied torque is constant for the whole swimmer regardless of the tail geometry, and the second method implies that the torque is proportional to the surface area of the tail. For swimmers with a constant total length, both conditions are considered here: as constant torque per helical wave, T/λ = constant, and constant torque per surface area, $T/w\lambda$ = constant, respectively. Swimming velocity, torque and efficiency are normalized with the values obtained for the standard ribbon rotating at constant angular velocity, ω

36

= 2π, inside a channel of radius twice as much as the amplitude of the base ribbon. Under constant torque, swimming velocities of helices can be also viewed as the mobility coefficients [42], which is given by the ratio of the swimming velocity and the torque.

2.2.2.1. Wavelength

2.2.2.1.1. Constant ω

As λ is varied other dimensions are kept at the base values: $B = 1$, $R_{ch} = 2$, $d = 0.03$ and $w = 1.29$, for the ribbon and the filament, and $d = 1.29$, $w = 0.03$ for the screw. Figure 2.18 depicts the effect of λ on the normalized swimming velocity U/U_0, torque, T/T_0, and the efficiency, η/η_0, with respect to the standard ribbon as the base case. Swimming velocity of filaments and ribbons are similar but significantly slower than screws, which achieve higher swimming velocities at all wavelengths than ribbons and filaments (Figure 2.18a) at constant ω. Having the same thickness, filaments swim faster than ribbons. According to Figure 2.18b, thin filament swims most efficiently, followed by the screw and the ribbon. Despite having the highest swimming velocity, screws are not as efficient as thin filaments at the base dimensions. Moreover, the wavelength of the original ribbon design [23] is optimal inside a circular channel with a radius twice the amplitude of the helix while other dimensions are kept the same.

Screws achieve higher swimming velocities at the cost of larger torque requirement as shown in Figure 2.18c and Figure 2.18d. For the filament and the ribbon, T/T_0 increases linearly with λ, however, for the screw T/T_0 increases with λ with two different slopes. Normalized torque per unit length, T/λ, increases sharply as $\lambda \rightarrow 0$, and converges to a constant value as $\lambda/\lambda_0 \gg 1$ as shown in Figure 2.18d. T/λ converges to a constant value for the thin filament just as $\lambda/\lambda_0 \approx 0.5$, whereas for the ribbon and the screw convergence is not completed even for $\lambda/\lambda_0 = 2.5$. The effect of λ on the convergence of T/λ is an indicator of the hydrodynamic interactions between the successive helical turns. Having a localized flow field due to its small cross-section, hydrodynamic interactions between the successive loops of the helix are not significant for sufficiently large wavelengths. On

the other hand, hydrodynamic interactions between the helical turns is the strongest for screws followed by ribbons.
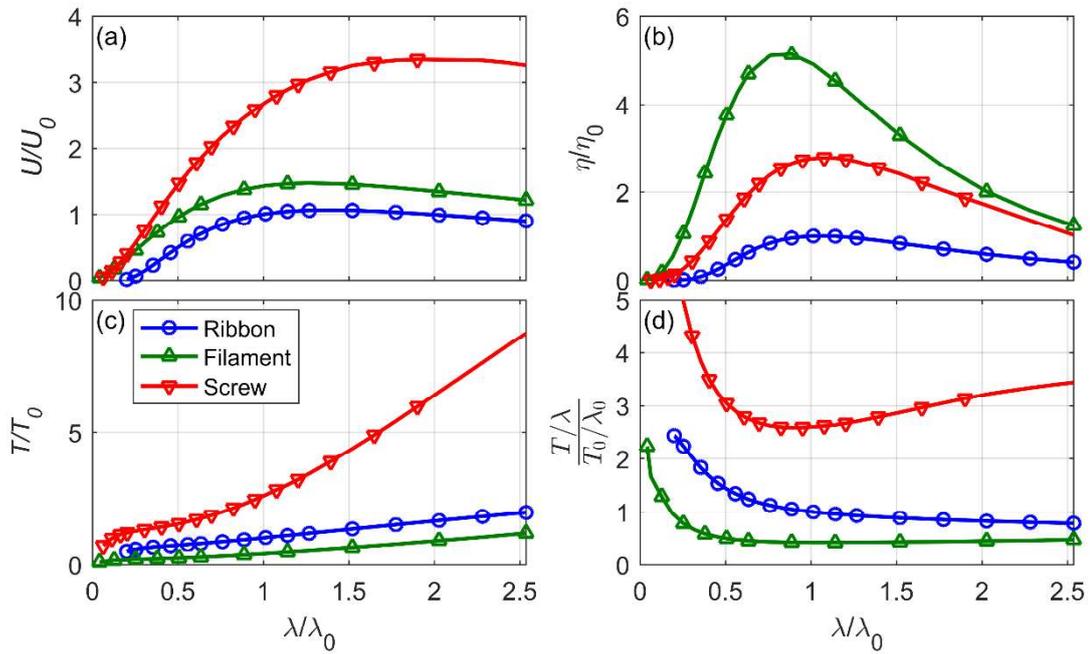
Figure 2.18 Effect of wavelength on the swimming velocity (a) efficiency (b), torque (c) and torque per unit length (d) for constant ω –blue line with round markers for the ribbon, green line with triangle markers for the filament and the red line with inverted triangle markers for the screw.

2.2.2.1.2. Constant T/λ

For constant T/λ, the thin filament outperforms the ribbon and the screw, and achieves swimming velocities almost as four times as the velocities of the screw and the ribbon (Figure 2.19a), due to having smaller cross-section and achieving higher ω under the same torque compared to screws and ribbons as shown in Figure 2.19b. Albeit the fastest at constant ω, the screw swims only slightly faster than the ribbon at constant T/λ for small λ and even slightly slower with increasing λ as the angular velocity decreases due to increased rotational drag. Velocity of the ribbon remains almost constant as λ increases due to slowly increasing ω.
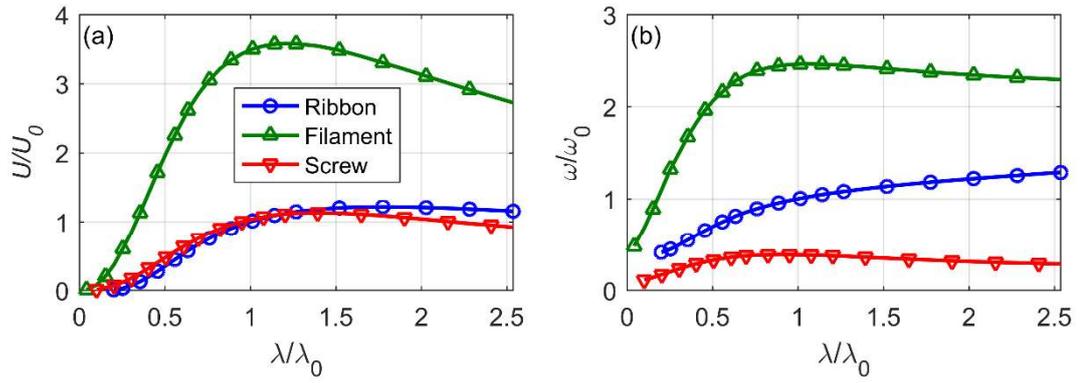
Figure 2.19 Effect of wavelength on the swimming velocity (a), and angular velocity (b) for constant torque per length.
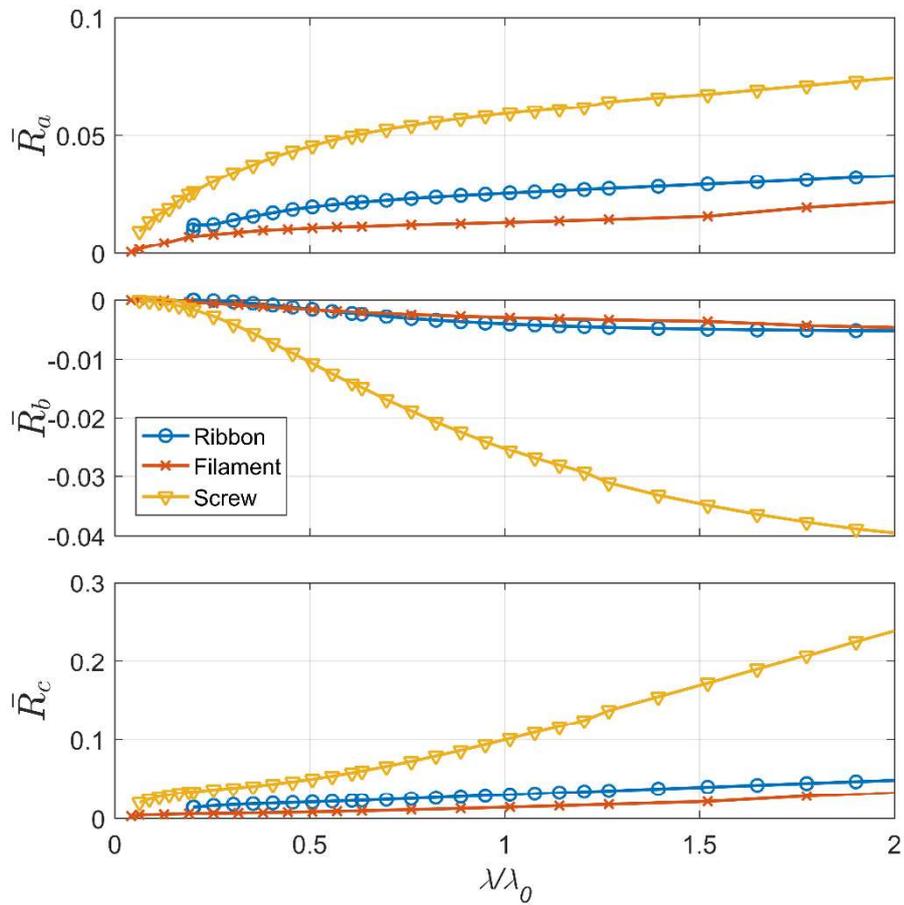
Figure 2.20 Translational, translation-rotation coupling, and rotational resistance coefficients plotted against the normalized wavelength λ/λ_0.

Figure 2.20 depicts the resistance coefficients for all three types of helical structures with rectangular cross-sections, namely, ribbons, filaments and screws. It is observed that the translational resistance coefficient $\overline{R}_a$ is the highest for the screw type due to its increased cross-sectional area, which causes the inferior swimming performance of the screw type structure under constant T/λ. However, while swimming at constant angular velocity and under zero net force, screws achieve higher velocities due to the higher magnitude of $-\overline{R}_b / \overline{R}_a$ ratio compared to the filaments and ribbons (Figure 2.21). $\overline{R}_b$ values are very similar for the ribbon and the filament, however, due to the lower translational resistance experienced by the filament compared to the ribbon, $-\overline{R}_b / \overline{R}_a$ ratio of the filament is slightly higher, thus its lateral velocity at constant angular velocity is higher than that of the ribbon. Furthermore, $\overline{R}_a$ and $\overline{R}_c$ are the lowest for the filament, therefore, it outperforms both the screws and ribbons under constant T/λ application.
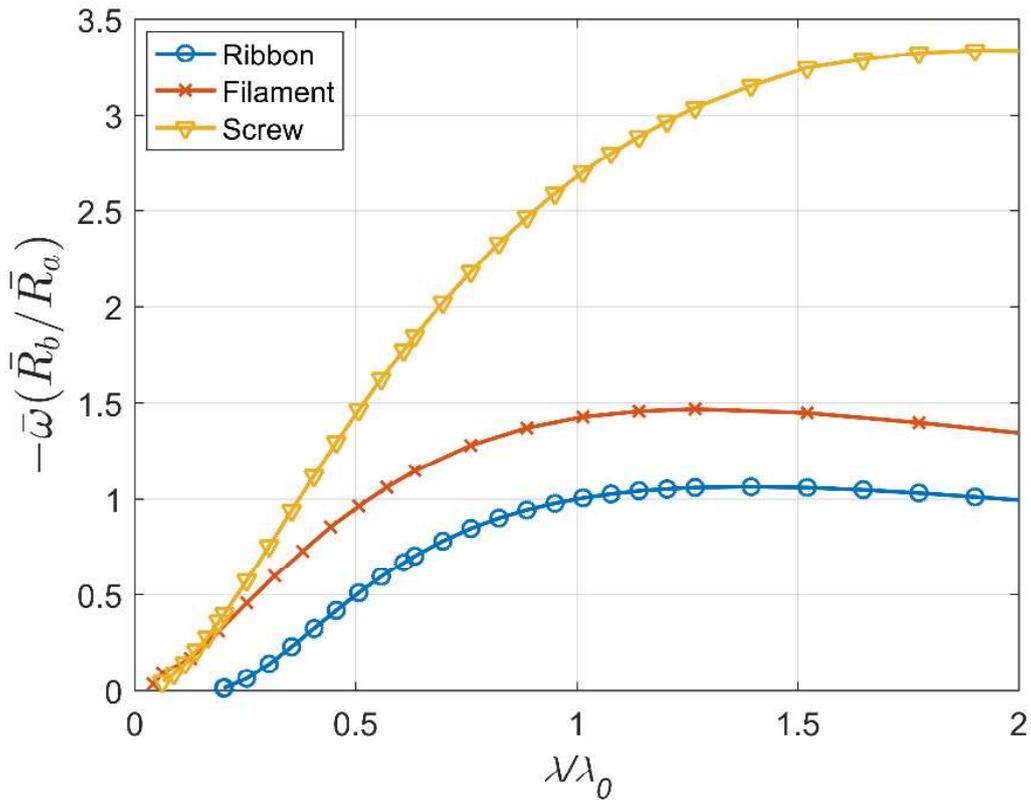
Figure 2.21 Velocity profile with respect to the changing wavelength, obtained using the resistance coefficients.

2.2.2.2. Channel radius

2.2.2.2.1. Constant ω

In Figure 2.22, U/U_0, T/T_0 and η/η_0 are plotted against R_{ch} as λ; d and w are kept constant at the base values (Table 2.1). Since the pre-set value of d for the screw is the same as the value of w for the ribbon, the smallest value of R_{ch} is 1.65 for screws and 1.07 for the ribbon and the filament. At constant ω, the Archimedean screw swims the fastest compared to the ribbon and the thin filament for all R_{ch} values. As R_{ch} increases, swimming velocities of the screw and the filament decrease, and the velocity of the ribbon increases for up to $R_{ch} \approx 1.7$ and decreases for larger R_{ch}. Positive influence of the confinement on the swimming velocity has been reported for helical swimmers by other studies [36, 40, 44, 98, 99] in the literature as well. Typically, as $R_{ch} \rightarrow 1$, the U is expected to approach to the corkscrew limit, $(\omega/2\pi)\lambda$, due to increased traction from the wall, whereas the torque increases to the traction-limit as well due to increasing shear with $1/c$, where $c = R_{ch} - d/2 - 1$ is the clearance between the surface of the helical body and the channel wall. Increase in the traction is apparent in the increasing magnitude of $\overline{R}_b$ with respect to decreasing channel radius (Figure 2.23). For $R_{ch} > 2$, T does not vary significantly for the ribbon and the filament, as the rotational drag, $\overline{R}_c$ saturates beyond this value of channel radius (Figure 2.23). According to Figure 2.22c, order of helical structures from the highest to the lowest efficiency does not change and the maximum efficiency is attained for $R_{ch} \approx 2$, i.e. twice the amplitude of the helix. Magnitude of the $-\overline{R}_b / \overline{R}_a$ ratio is the highest for the screw type helix, therefore, at constant angular velocity it outperforms the ribbon and filament type helices (Figure 2.24).
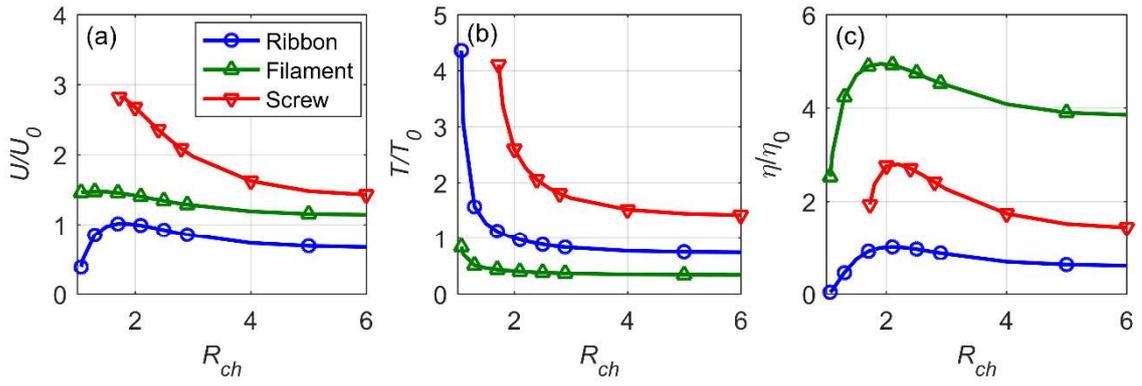
Figure 2.22 Effect of the channel radius on the swimming velocity (a), torque (b), and efficiency (c) for constant ω.
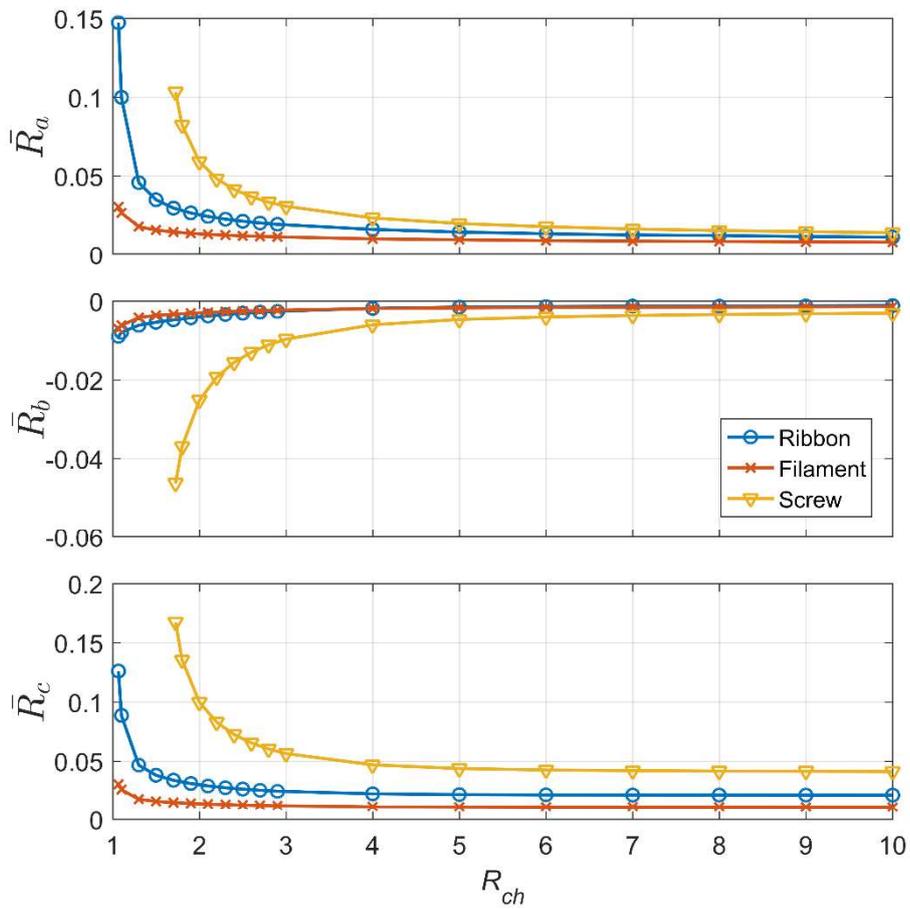
Figure 2.23 Translational, translation-rotation coupling, and rotational resistance coefficients plotted against channel diameter R_{ch}.
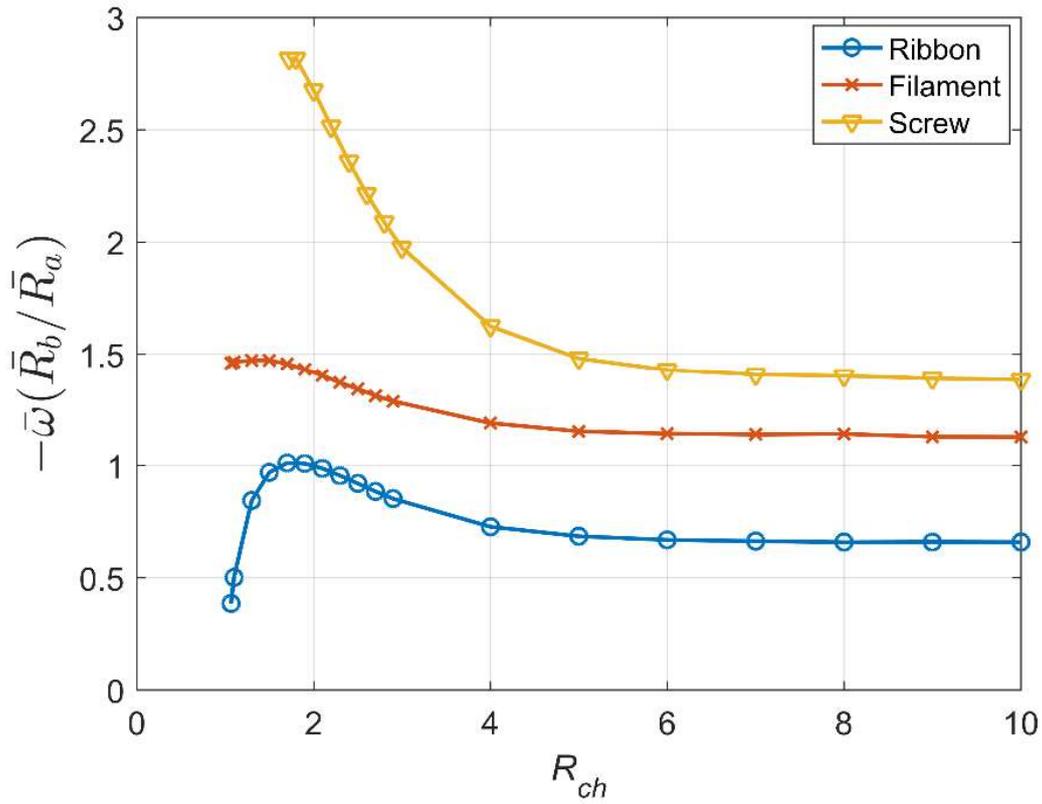
Figure 2.24 Velocity profile with respect to the changing channel radius, obtained using the resistance coefficients.

2.2.2.2.2. Constant T

In Figure 2.25a, U increases with R_{ch} and saturates for $R_{ch} > 2.5$ for all helices, however the thin filament swims almost 3 times faster than the ribbon and the screw due to its lower translational and rotational drag (Figure 2.23). Ribbon and screw type helices attain very close velocity values with a cross-over at $R_{ch} \approx 2$; for $R_{ch} < 2$, ribbons are slightly faster than screws due to their decreased resistance to translation and rotation compared to the screws (Figure 2.23). ω increases monotonically with and R_{ch} saturate for $R_{ch} > 4$ (Figure 2.25b) demonstrating that hydrodynamic interactions between the body and the channel wall are weaker when R_{ch} is sufficiently large. For constant T, filaments rotate about 2.5 times faster than ribbons, and about 5 times faster than screws

for which the hydrodynamic resistance is the largest. Ribbons rotate slower than filaments because of larger shear force at the surface.
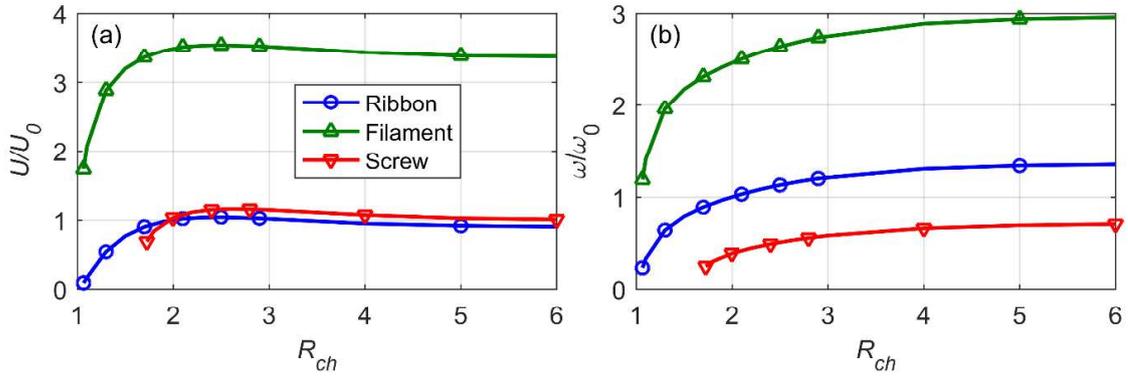
Figure 2.25 Effect of the channel radius on the swimming velocity (a), and angular velocity (b) for constant torque.

2.2.2.3. Thickness

2.2.2.3.1. Ribbons

For constant ω, velocity of the swimmer increases for all wavelengths as d increases up to $d/R_{ch} \approx 0.75$, and the maximum velocity is slightly above 2.5 times the reference value as shown in Figure 2.26a. U is significantly lower for $\lambda/\lambda_0 = 0.5$ than for $\lambda/\lambda_0 > 1$ for all thickness values, and relatively insensitive to λ/λ_0 for large wavelengths as also discussed in section 2.2.2.1 for ribbons. As the thickness increases, swimming velocity is larger for larger wavelengths similarly to screws as shown in Figure 2.18a.
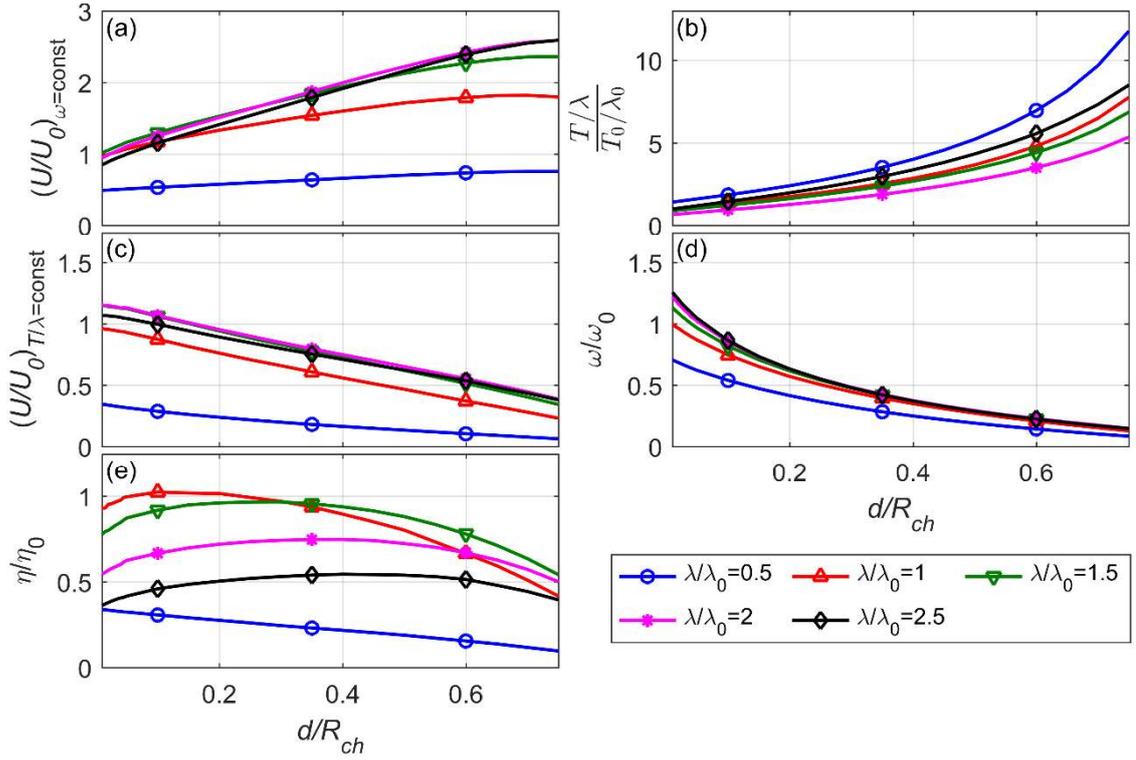
Figure 2.26 Effects of thickness and wavelength of the ribbon on the swimming velocity for constant ω (a) and for constant torque (c); torque per wavelength for constant ω (b); angular velocity for constant torque (d); and efficiency (e).

Increasing the thickness of ribbons is beneficial for swimming velocity as $-\bar{R}_b / \bar{R}_a$ ratio increases with increasing wavelength (Figure 2.28), however T/λ increases monotonically for all wavelengths as shown in Figure 2.26b due to the increase in resistance to rotation with increasing thickness (Figure 2.27). The monotonic increase of T/λ indicate that swimming velocity and the angular velocity decrease with increasing thickness of the ribbon when T/λ is kept constant (Figure 2.26c and 2.26d). Decreasing with the thickness, U is insensitive to λ for $\lambda/\lambda_0 > 1$ as shown in Figure 2.26c. As shown in Figure 2.26e, efficiency is slightly above unity for $\lambda/\lambda_0 = 1$ for $d/R_{ch} \sim 0.1$, which is almost 70 times as thick as the original design [23]. Overall, efficiencies of ribbons with larger wavelengths peak at higher values of d/R_{ch} and exceed the efficiencies of ribbons with smaller wavelengths, but η/η_0 remains below unity. It is observed that the coupling resistance coefficient $\bar{R}_b$ increases with increasing wavelength (Figure 2.27).
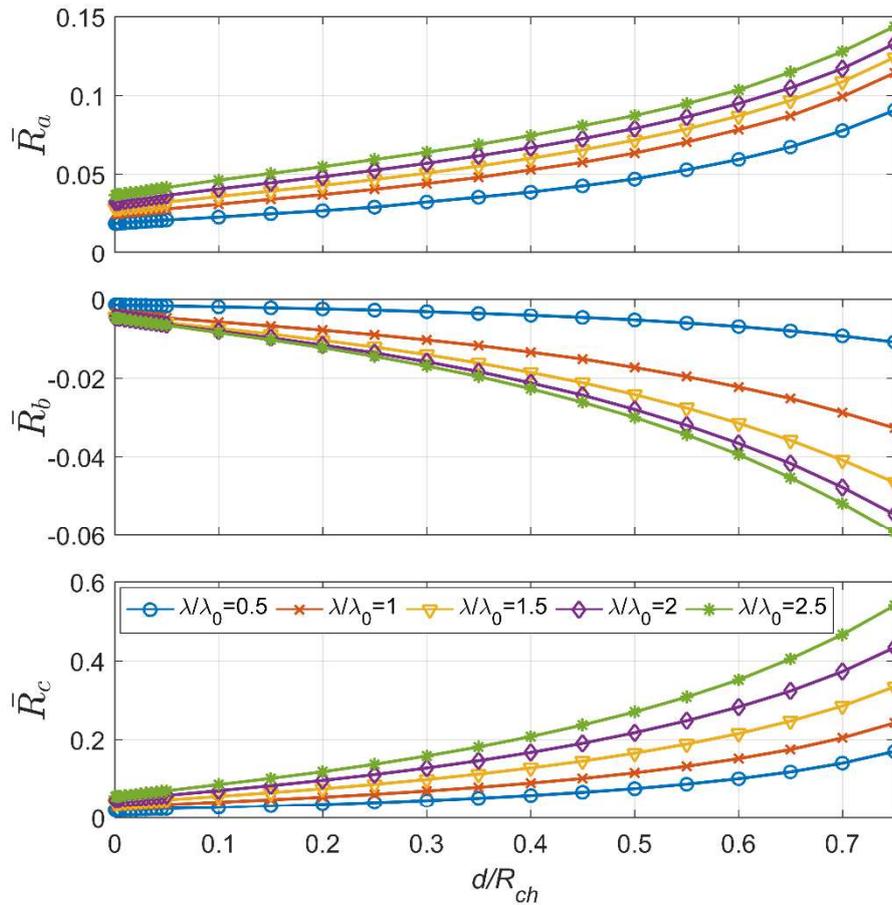
Figure 2.27 Translational, translation-rotation coupling, and rotational resistance coefficients plotted against normalized thickness d/R_{ch} for various wavelengths of the ribbon type swimmer.
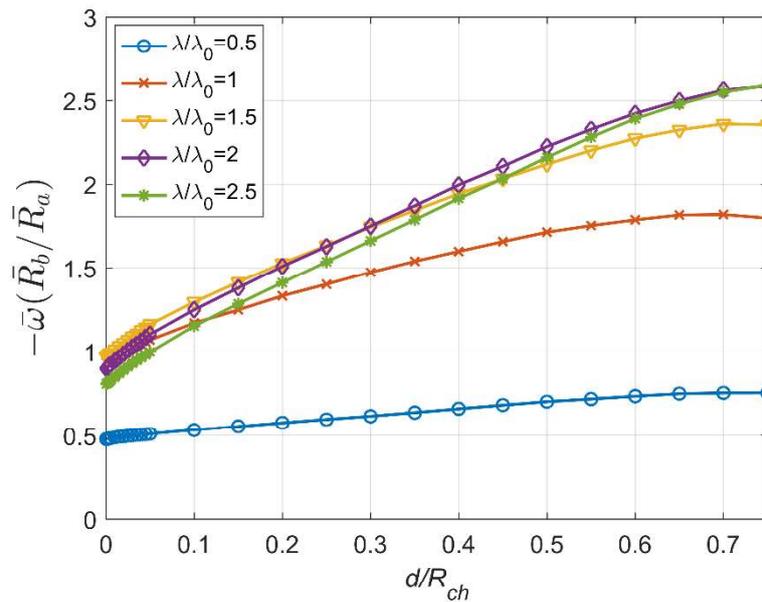
Figure 2.28 Velocity profile with respect to the changing thickness (ribbon type swimmer), obtained using the resistance coefficients.

2.2.2.3.2. Screws

Based on the definition in Figure 2.1, d is called thickness for the Archimedean screws also for the sake of consistency. Combined effects of λ and d on swimming performance of screws including the filament limit are shown in Figure 2.29. For constant ω, U increases with d starting from the filament limit, and reaches to the maximum at the limit of the range, $d/R_{ch} = 0.75$ for $\lambda/\lambda_0 = 2$ (Figure 2.29a). As d increases, U is higher for larger values of λ, but multiple cross-overs of velocity curves indicate that optimum λ varies with d. T/λ increases with thickness for all wavelengths (Figure 2.29b), however it does not vary monotonically with λ as also shown in Figure 2.18d for the base screw that has $d/R_{ch} = 0.65$. For constant T/λ, swimming velocity increases with decreasing thickness of the screw for all wavelengths. As $d/R_{ch} \rightarrow 0$, T/λ converges to a single value for all wavelengths and spreads out for different wavelengths as d/R_{ch} increases. Angular velocity is the maximum for $\lambda/\lambda_0 = 1$ and decreases with thickness (Figure 2.29d). Lastly, efficiency peaks around $d / R_{ch} \approx 0.025$, with the reference wavelength as the optimum (Figure 2.29e).
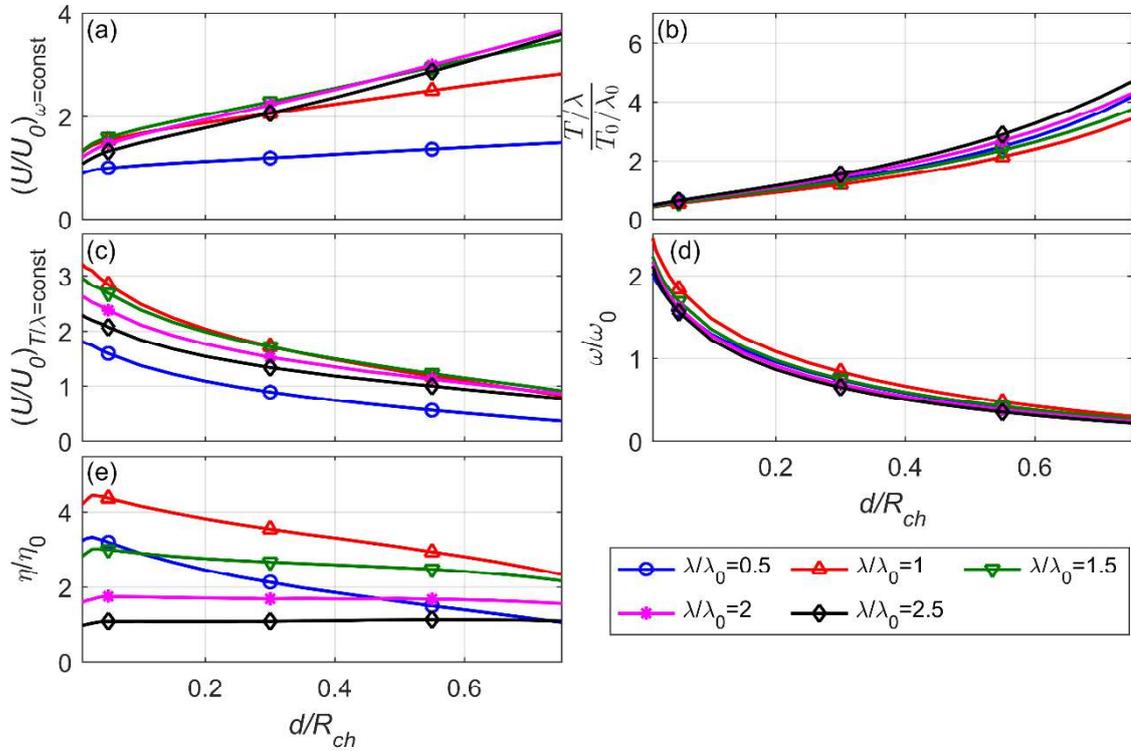
Figure 2.29 Effects of thickness and wavelength of the screws on the swimming velocity for constant ω (a) and for constant torque (c); torque per wavelength for constant ω (b); angular velocity for constant torque (d); and efficiency (e).
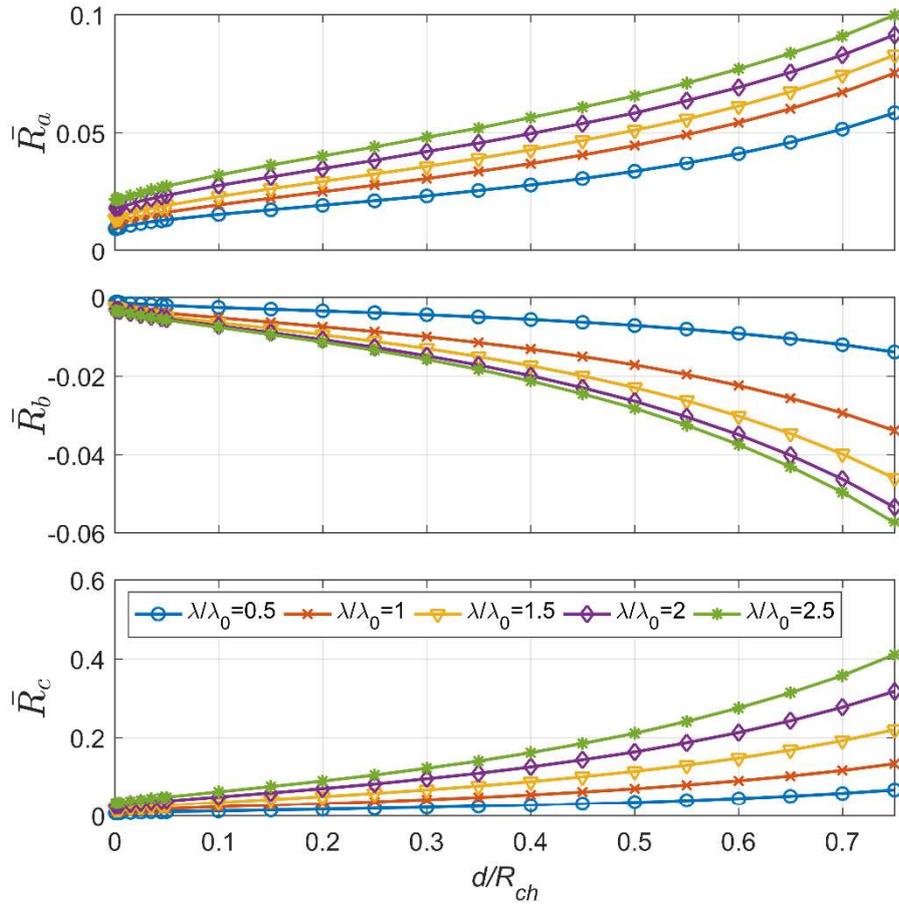
Figure 2.30 Translational, translation-rotation coupling, and rotational resistance coefficients plotted against normalized thickness d/R_{ch} for various wavelengths of the screw type swimmer.
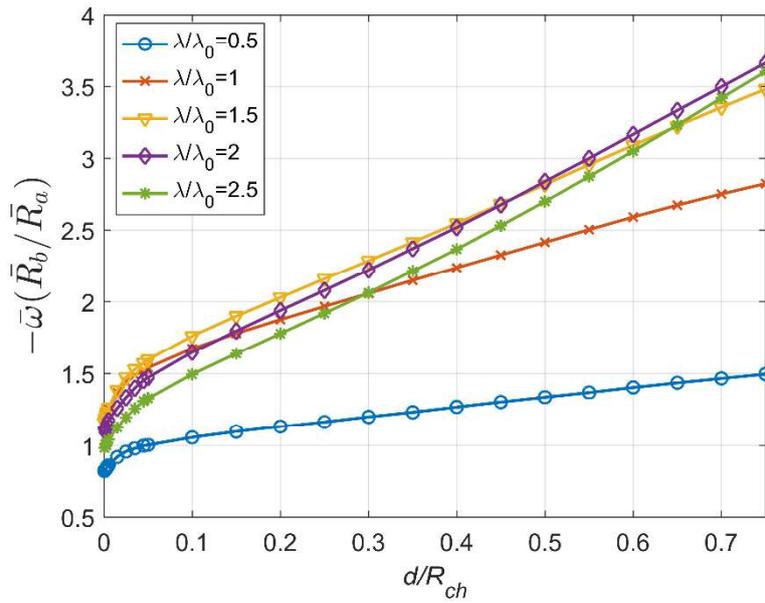
Figure 2.31 Velocity profile with respect to the changing thickness (screw type swimmer), obtained using the resistance coefficients.

2.2.2.4. Width

Effects of w are considered for constant ω, constant T/λ for swimmers with a magnetic head, and constant $T/w\lambda$ for swimmers with magnetic coating [19]. At the limit of $w/\lambda_0 = 1$, helical ribbon becomes a hollow cylinder having no means of propulsion as the fluid cannot be displaced axially to achieve locomotion, hence U monotonically decreases to zero with w as shown in Figure 2.32a. As $w \to d_0$, the ribbon converges to the filament, hence the velocity increases for constant-ω and constant-T/λ cases, but $U \to 0$ for the constant-$T/w\lambda$, for which the optimal value of the w/λ_0 is 0.25, which is also the point where the magnitude of the coupling resistance coefficient peaks (Figure 2.33). T increases monotonically with w for constant ω due to increasing surface area (Figure 2.32b). Angular velocity decreases with increasing width for constant-T/λ (Figure 2.32c) but increases with the width in the case of constant-$T/w\lambda$ and is linked with the improvement in the swimming velocity as well. However, as $w/\lambda_0 \to 1$ swimming mechanism of the ribbon is greatly compromised, and propulsion cannot be achieved. Efficiency decreases sharply from the filament limit to zero with increasing width (Figure 2.32d).
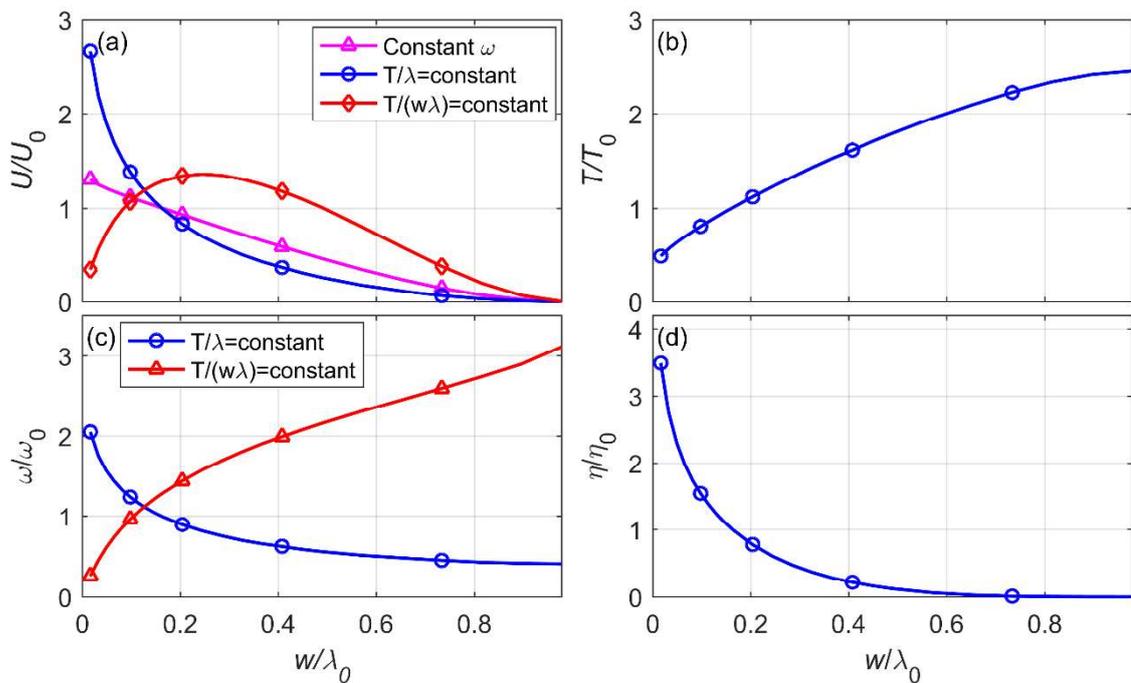

Figure 2.32 Effect of changing width, w, on swimming velocity (a), torque (b), angular velocity (c), and efficiency (d).
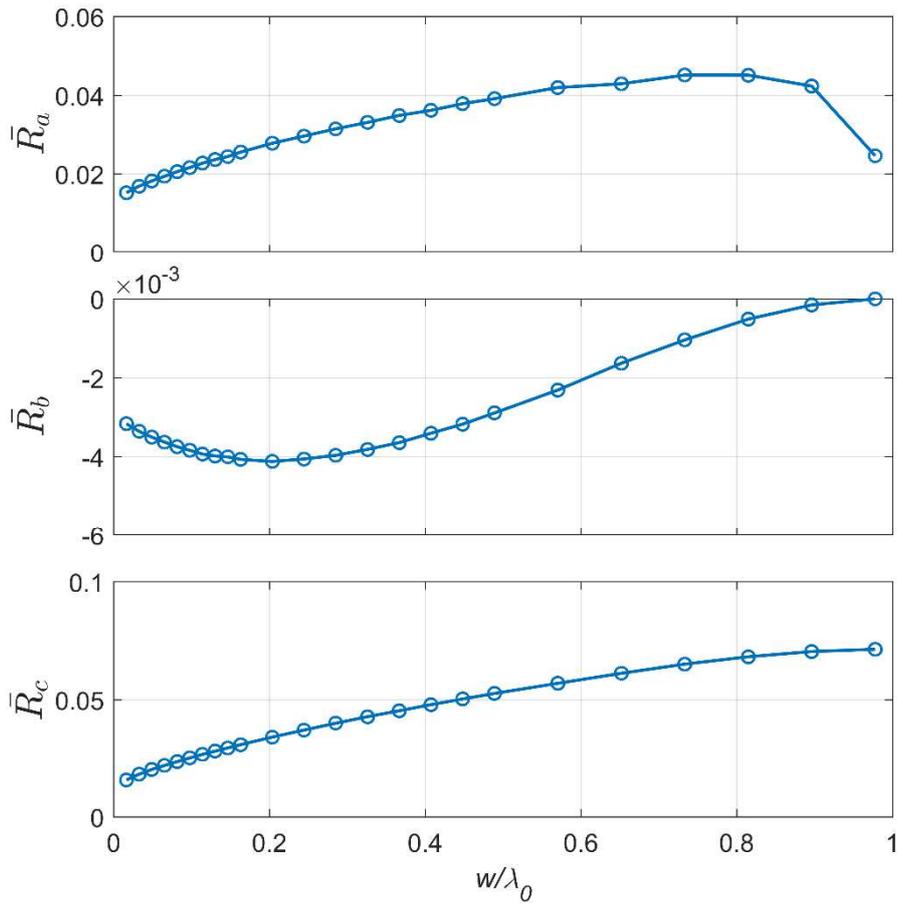
Figure 2.33 Translational, translation-rotation coupling, and rotational resistance coefficients plotted against normalized width w/λ_0.
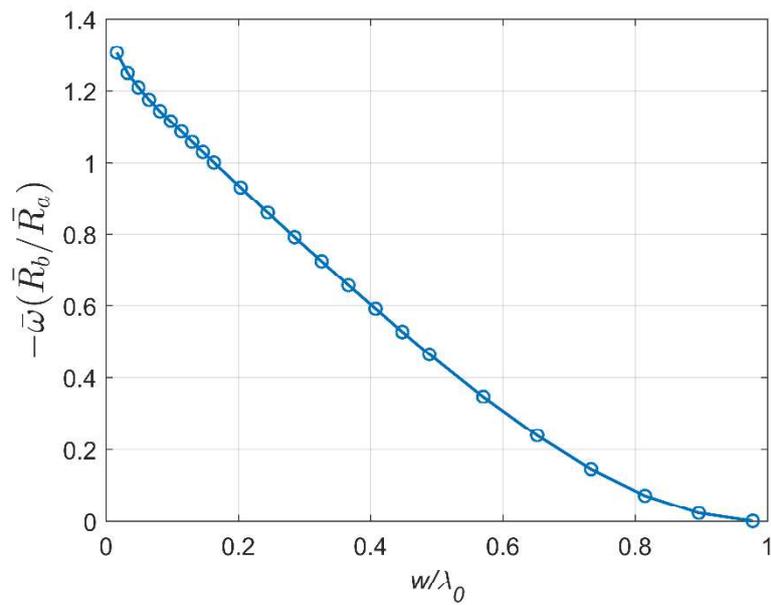
Figure 2.34 Velocity profile with respect to the changing width, obtained using the resistance coefficients.

2.3. Discussion

Effects of geometric parameters on the swimming performance of infinite helical structures are studied with a CFD model. Results are validated with theoretical studies reported in literature for helical rods and compared to experimental and previous numerical results for helical ribbons. Torque, angular velocity, mobility, and efficiency comparisons are presented for rods, ribbons, filaments and screws.

For helical rods, swimming velocity from the CFD model converges to results from the slender-body-theory [32] (SBT) for $\lambda/D_{ch} < 1/2$ and to results from the approximate perturbative solution [33] (APS) for $\lambda/D_{ch} > 3.5$. It is important to emphasize that SBT does not include the wall effects but the hydrodynamic force distribution only on the helical body and APS is valid only for cylindrical rods with a small-amplitude-helical wave inside circular channels. Therefore, results indicate that body-body hydrodynamic interactions are dominant for small wavelengths, and body-wall interactions for large wavelengths. Moreover, CFD results agree better with SBT especially for thin filaments as $a \rightarrow 0$ and the flow field becomes more localized, and with APS as $B\rightarrow 0$ as the flow between the rod and the channel is predicted very well with the theory. Furthermore, overall results show that confinement improves the velocity and efficiency at constant ω unless the clearance, c, between the surface of the helix and the channel wall is very small, typically for $c < 0.05$. As $c \rightarrow 0$, shear stress and the torque increases proportional to $1/c$, hence the efficiency drops sharply. However, improvement in the velocity continues as the radius of the rod or the eccentricity increases. Swimming velocity has a maximum with respect to B, and a minimum with respect to a.

In addition to helical rods, effects of thickness, d, width, w, λ and R_{ch} are investigated while B is used as the length scale in the nondimensionalization for helical ribbons with $w >> d$, thin filaments with $d\rightarrow 0$ and $w\rightarrow 0$ and Archimedean screws with $d >> w$. In addition to constant ω, constant torque per length of the swimmer, $T/\lambda = $ constant, and per surface area of the swimmer, $T/w\lambda = $ constant, are considered in the study for swimmers rotated by a magnetic head and by magnetic coating on the surface

respectively. Helical thin filaments are found to be the most efficient swimmers with the highest velocities for constant T/λ. Archimedean screws are the second in efficiency, but they are the fastest swimmers at constant ω. As confinement increases, or R_{ch} decreases: U increases for screws and filaments at constant ω, but the slight increase in U is followed by a sharp decrease for ribbons. At constant T/λ, U decreases for all helices with the increasing confinements. As the width of the ribbon increases, U decreases for constant-ω and constant-T/λ cases but has a maximum for the constant-$T/w\lambda$ case for $w/\lambda_0 \approx 0.25$. Efficiency of ribbons decreases with increasing w. Lastly, performance of helical ribbons is not too sensitive to thickness, in fact thicker ribbons are slightly slower but more efficient than the thinner ones. The thickness of the ribbon can be decided based on the manufacturing constraints for optimal width, wavelength and amplitude rather than the hydrodynamic performance.

3   SWIMMING OF RIGID SPHERES

Spherical particles can be used in various medical applications as modified cells and as colloids in bulk and inside channels. However, mobilizing them by an external force is not easy, as their linear drag is high. Especially at small scales, it is easier to move them via rotation, as their rotational drag is scaled with the third power of the length scale, whereas their linear drag is proportional to the length scale. Due to this disadvantage of the spherical particles, helical structures, which have the ability to convert rotary motion to linear translation are preferred in micro-swimming applications. However, the same conversion is possible for spherical particles alone if one takes advantage of the anisotropic hydrodynamic forces due to rotation of a sphere close to a wall. Due to the fact that spherical particles are less intricate structures than helical structures, which makes them easier to manufacture and miniaturized, spherical particles can be more advantageous compared to the helical structures once the mobility problem is solved.

In order to investigate the mobility of rotating spheres inside cylindrical channels, an experimental study is conducted. Neodymium spheres of diameters 1 mm and 1.9 mm are placed inside cylindrical glass channels of diameters 1.6 mm, 3 mm, and 5.7 mm such that which are of length 10 cm and filled with silicone oils of viscosity 1 Pa.s and 0.5 Pa.s . Sphere is rotated magnetically at different frequencies using two Helmholtz coil pairs and the motion of the sphere is recorded. Velocity profiles and trajectories of the spheres swimming inside channels of different radii at various frequencies are obtained by analyzing the recordings using image processing techniques. It is shown that the motion of the sphere is affected by the ratio of the channel/sphere radii greatly. The distance between the sphere and the channel wall plays a significant role on the motion

and the velocity of the swimmer. Experimental results are interpreted utilizing a resistance-based model and the coefficients presented by Bhattacharya et al. [6] and a CFD model that complements their findings. A kinematic model of the system is prepared and implemented to predict the velocity and trajectories of the spheres.

3.1. Methodology

3.1.1. Experimental Study

This section reports the experimental methodology adopted in the analysis of rotating and swimming spheres inside capillary tubes.

3.1.1.1. Experimental setup and operational parameters

Neodymium spheres of diameters 1 mm and 1.9 mm are placed into glass channels of diameters 1.6 mm, 3 mm and 5.7 mm (Table 3.1). The channels are filled with silicone oil of viscosities $\mu=1$ Pa.s and $\mu=0.5$ Pa.s (Figure 3.2). The tubes are placed into a vacuum chamber (0 PSIA, measured with Omega DPG5600B-30A PSIA) to fully degas the fluid, after which they are sealed. One tube at a time is placed horizontally inside the experimental setup consisting of three Helmholtz coil pairs connected to Maxon drivers controlled via LabVIEW software (Figure 3.3).

Two of the coil pairs (x and z pairs, Figure 3.3) are activated with sinusoidal out-of-phase currents to create a magnetic field rotating about the y-axis whereas the axis of the cylindrical channel is placed along the x-direction. The distance between the centers

of the sphere and the axis of the cylindrical channel is measured along the z-axis. Magnetic fields applied by individual coils are measured using Phidgets 1108 Magnetic Field Sensors to assure equal magnetic field strengths in both directions. The magnetic sphere is actuated at different magnetic field rotation rates ranging between [0.1-20 Hz] and its motion is recorded using a digital microscope from above to observe the movement in the xy-plane and response to the magnetic field. Movement in the xz-plane is captured with the help of a mirror, that is placed at a 45° angle next to the glass channel.

As a rotating magnetic field is applied to the magnetic sphere, its magnetic dipole moment tries to align with the direction of the applied magnetic field, which causes the rotation of the sphere. When the magnetic torque acting on the sphere is balanced by the viscous torque, the sphere rotates with the same rate as the rotating magnetic field and translates along x-axis. The sphere's direction of translation depends on the direction of the rotating magnetic field and the ratio of the channel diameter to sphere diameter. An example of the motion of the sphere inside the channel and coordinate system are given in Figure 3.1. The relationship between the magnetic dipole moment, $\mathbf{m}$, the magnetic field, $\mathbf{B}$, and the magnetic torque, $\tau_{\mathbf{m}}$ is given by the following equation:

$$\tau_{mag} = \mu_0 \mathbf{m} \times \mathbf{B} = \mathbf{M} \times \mathbf{B} \tag{12}$$

where μ_0 denotes the permeability of the free space and $\mathbf{H}$ is the magnetic field strength. As implied by the cross-product, actual magnetic torque acting on the sphere at any given instance depends on the sinus of the angle between the magnetic dipole moment vector of the sphere and the magnetic field vector, and the angle depends on the net torque acting on the sphere, taking both viscous and magnetic torques into account.
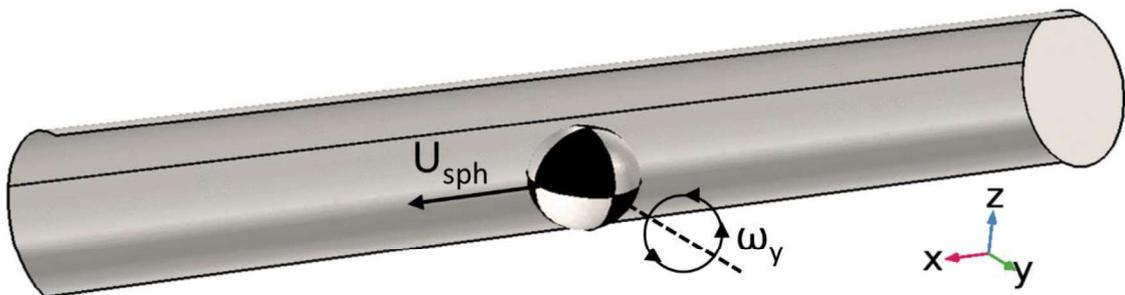
Figure 3.1 Coordinate system in the lab frame and an example of sphere's motion.

Table 3.1 Experimental parameters

	D_{sph} [mm]	D_{ch} [mm]
μ = 1 Pa.s	1	1.6
	1	3
	1.9	3
μ = 0.5 Pa.s	1.9	5.7

- Dsph= 1 mm, Dch=1.6 mm

- Dsph= 1 mm, Dch=3 mm

- Dsph= 1.9 mm, Dch=3 mm

- Dsph= 1.9 mm, Dch=5.7 mm

Figure 3.2 Cylindrical glass channels filled with silicone oil and magnetic spheres placed inside the channels.
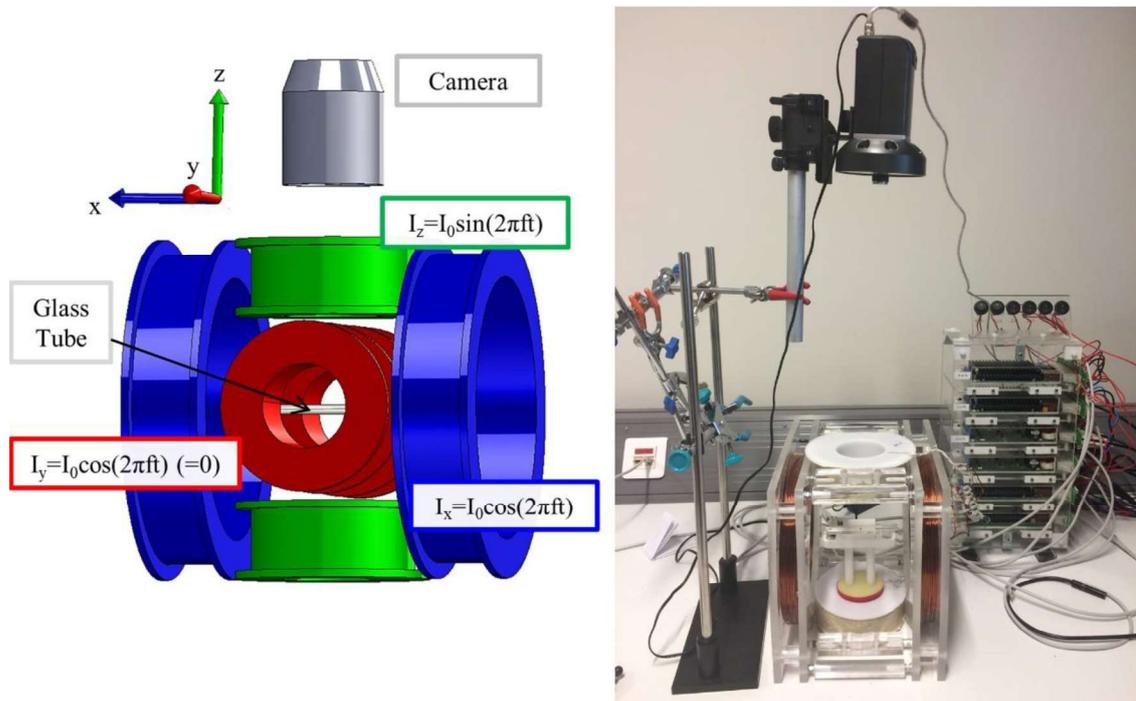
Figure 3.3 Experimental setup consisting of three Helmholtz Coil pairs, 6 Maxon drivers to control each of the coils separately using LabView, a high-resolution microscopic camera to record the experiments for image processing.

3.1.1.2. Image processing

To obtain the velocities of the spheres in three-dimensional space, an image processing code written in MATLAB is employed. The image processing code extracts a single frame of the experiment video and filters out the background in the first step. Afterwards, the image is converted to black and white in the second step. In the third and most crucial step, it increases contrast using the specified filtering parameters, after which only a black sphere against a black background is visible. The code then calculates the centroid of the sphere. This process is repeated in a loop until every frame of the video is processed. Position data of the centroid is stored in a file, which can be used to visualize the data in plots.

While the microscopic camera records the sphere's motion in the xy-plane, a mirror placed at a 45° angle next to the cylindrical glass channel allows recording the motion of

the sphere on the xz-plane simultaneously. For the case of the helical motion, image recorded from the mirror is also processed, thus the sphere's movement in all three axes are obtained to plot the helical trajectory. Both images are processed separately using the image processing code and the stored data is used to plot 3D trajectories of the spheres.

3.1.2. RFT Study

This section presents the kinematic model that is used to predict the swimming characteristics of the rigid spheres moving inside cylindrical channels.

3.1.2.1. Kinematic model

In order to predict the trajectories of the rigid spheres, we need the linear and angular velocities, U and ω, which can be obtained from the force balance. Instantaneous velocity of the sphere in the cylindrical coordinate frame can be deduced from the time derivative of its position defined in the channel frame as follows:

$$\frac{d\mathbf{r}}{dt} = \mathbf{u} \tag{13}$$

To track the direction of the magnetic dipole moments and their alignment with the external magnetic field, time derivative of the sphere position in this sphere frame can be determined from the equation:

$$\frac{d\mathbf{e_k}}{dt} = \omega \times \mathbf{e_k}, \, k = 1, 2, 3 \tag{14}$$

58
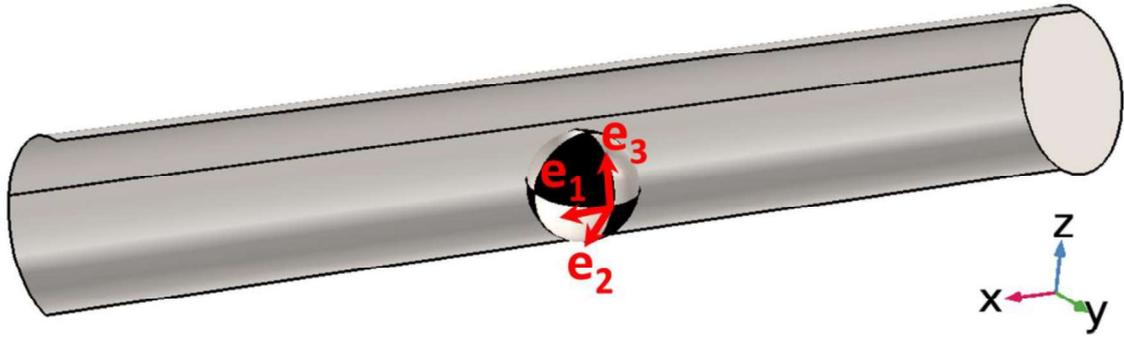
Figure 3.4 Visualization of the sphere inside the channel and coordinate frames in the channel and on the sphere

Governing equations for this motion based on the force and torque balances are used to identify **u** and **ω**. The sphere performs force-free and torque free swimming, where inertial and external forces will be counteracted by the viscous forces and torques respectively. While identification of some of the components defining the force acting on the sphere are straight forward, a few of them require careful treatment.

Construction of the equation of motion for a swimming sphere has an extensive trail in the literature dating back to 1880s. Basset [64], Boussinesq [65] and Oseen [66] studied the motion of sphere settling under gravity in a quiescent fluid. In such a fluid, only disturbance to the flow occurs due to the settling motion of the sphere, which of low Reynolds number and thus allows deduction of the resulting fluid force on the sphere using Stokes equations [67]. Tchen [68] extended the works of Basset, Boussinesq and Osseen [64–66] to include unsteady flows in his PhD thesis, which prompted an immense number of studies suggesting corrections to his equations. Among the notable corrections, Corrsin and Lumley's [69] remark on the contribution of the pressure gradient on the net force acting on the particle, and Buevich's [70] correction on the term suggested by [69] should be listed. Soo [71] and Gitterman and Steinberg [72] offered their own solutions. In 1982, Maxey and Riley [67] gave the equation its widely used form to this day with corrections of Auton et al. [73] and Maxey himself, and can be implicitly expressed as follows [94]:

$$m_{sph}\mathbf{a}_{sph} = \mathbf{f}^{p} + \mathbf{f}^{added\ mass} + \mathbf{f}^{visc} + \mathbf{f}^{hist} + \mathbf{f}^{buoyancy} + \mathbf{f}^{weight} \quad (15)$$

There are two important remarks that need to be made here: 1) Maxey-Riley equation does not consider the effects on the sphere due to the sphere-channel interactions

as the equation is for a sphere in a nonuniform flow, moving in bulk; and as a consequence, 2) there is no term that describes the lift force that the sphere experiences due to rotary motion in the presence of a boundary. A summary of important works on the lift force observed in the presence of a boundary or a flow is provided in the literature survey [74-94]. Throughout the extensive review, no expression for the lift force acting on the spheres moving inside cylindrical conduits could be found. However, for the inertial regime, lift force is necessary to predict the trajectory of the spheres accurately, which will be discussed further in the results section.

In the case where all the forces are determined, and zero force condition is applied, force balance can be summarized with the equation:

$$\sum_m \mathbf{f}_m = 0, \, m = \{viscous, gravity, magnetic, history, added\ mass, lift\} \tag{16}$$

The viscous force, counteracting all other forces acting on the sphere, can be calculated by utilizing resistive force theory (RFT). Resistive force theory relates the translational and rotational velocities of the sphere to the forces and torques experienced by it with a linear system of equations as follows:

$$\begin{bmatrix} \mathbf{F^{tt}} & \mathbf{F^{tr}} \\ \mathbf{F^{rt}} & \mathbf{F^{rr}} \end{bmatrix} \begin{bmatrix} \mathbf{u} \\ \boldsymbol{\omega} \end{bmatrix} = \begin{bmatrix} \mathbf{f} \\ \boldsymbol{\tau} \end{bmatrix}_{visc} \tag{17}$$

where $\mathbf{F^{tt}}$, $\mathbf{F^{tr}}$, and $\mathbf{F^{rr}}$ are 3x3 matrices consisting of translational, translation-rotation coupling and rotational resistance coefficients of the sphere respectively, and $\mathbf{F^{rt}}$ is the transpose of the matrix $\mathbf{F^{tr}}$. $\mathbf{F}$, $\mathbf{T}$, $\mathbf{u}$ and $\boldsymbol{\omega}$ are 3x1 vectors containing the viscous force, viscous torque, velocity and angular velocity components in x, y, and z-directions. $\mathbf{f}_p$ and $\boldsymbol{\tau}_p$ are the forces and torques experienced by the sphere due to the pressure gradients created in the presence of a flow, which are set to zero in this case as this study is restricted with the motion of the sphere inside quiescent fluids. $\mathbf{f}_{ex}$ and $\boldsymbol{\tau}_{ex}$ represent all other forces that are either externally applied or inertial in nature.

Resistance coefficients are calculated from the CFD solution of Stokes equation with no-slip boundary condition as explained in the next section. Here it should be noted that the nonlinear lift force discussed in detail above, cannot be absorbed into the resistance coefficients as equation 17 is a linear expression of relationship between the resistance coefficients, velocities, forces and torques.

Gravitational force acting on the sphere when the cylindrical conduit is inclined is defined as follows, where α is the angle the central axis of the cylindrical channel makes with x-axis, m_{sph} is the mass of the magnetic sphere and **g** is the gravity vector in -z-direction:

$$\mathbf{f}_g = (\sin\alpha)m_{sph}\mathbf{g} \tag{18}$$

Only external force applied to the sphere is the magnetic force due to the magnetic fields applied to actively mobilize the sphere. Magnetic force on the sphere is calculated using the equation:

$$\mathbf{f}_{mag} = \nabla(\mathbf{m}\cdot\mathbf{B}) \tag{19}$$

Unsteady forces such as the history force and added mass force play an important role in the swimming of microorganisms. They use sudden velocity jumps or directional changes to attack preys or escape immediate threats. Jakobsen [95] reports that *Balonion comatum*, a ciliate plankton, increases its velocity five-fold in a time period shorter than the time needed to advance the organism more than one body length. Such motions create unsteady disturbances in the flow field that can affect the velocity and the trajectory of the swimmers even after the motion causing the disturbance ceases. However, in the scope of the study reported here, these unsteady forces can be neglected, as the density of the particle used in this study is not comparable to the density of the fluid used in the experiments [96]. Wang and Ardekani [97] model a spherical unsteady swimmer and show that the Boussinesq-Basset history term and the added mass term can be neglected when the product of Strouhal and Reynolds number is smaller compared to unity:

$$\mathbf{f}_{hist} + \mathbf{f}_{mass} \rightarrow 0, SlRe = \left(\frac{1}{2}m_f + m_s\right)\omega / 6\pi\mu r_{sph} \ll 1 \tag{20}$$

In this study, highest angular velocity Highest *SlRe* that occurs throughout the experiments is 0.1886, which is obtained when the viscosity of the silicone oil is 1 Pa.s, magnetic field rotation frequency is 20 Hz and r_{sph} is 0.95 mm. However, as this rotation frequency is above the step-out frequency, above which the sphere rotation loses synchronicity with the rotating magnetic field, angular velocity of the sphere does not reach 20 Hz. Therefore, actual *SlRe* value is below 0.1886 for this motion. Thus, the effects of history and added mass are not included in the kinematic model.

Torque swimming condition of the spheres is described by the expression:

$$\sum_m \boldsymbol{\tau}_m = 0, \, m = \{viscous, magnetic\} \tag{21}$$

where the viscous torques balance the external torques.

Instantaneous position of the sphere is calculated using Crank-Nicholson method at time intervals of $\Delta t = 1/1000/f$ for high accuracy.

3.1.2.2. CFD model

A CFD model of the of the sphere moving inside the cylindrical channel is developed, which solves incompressible Stokes equations, that are given as follows in non-dimensional form:

$$-\nabla p + \frac{1}{Re} \nabla^2 \mathbf{u} = 0 \quad \text{and} \quad \nabla \cdot \mathbf{u} = 0 \tag{22}$$

where $\mathbf{u}$ and p denote the velocity vector and pressure respectively. The Reynolds number, Re, is based on the rotation frequency of the sphere, f, and a length scale, ℓ, such as the diameter of the channel: i.e. $Re = \rho \ell^2 f / \mu$, where ρ is the density and μ is the viscosity of the fluid.

No-slip boundary conditions are used on the channel wall and on the sphere surface moving with the velocity:

$$\mathbf{u} = \mathbf{U} + \boldsymbol{\omega} \times (\mathbf{r} - \mathbf{r_0}), \quad \mathbf{r} \in S \tag{23}$$

where $\mathbf{U}$ is the velocity, $\boldsymbol{\omega}$ is the angular velocity of the sphere, $\mathbf{r}$ is the position, $\mathbf{r}_0$ is the position of the centroid, and S represents the surface of the body.

COMSOL Multiphysics [90] software is used to solve incompressible Stokes equations with finite element method. P1+P1 discretization of the fluids and MUMPS direct solver is employed for the simulations. Triangular surface mesh is applied to the sphere surface and tetrahedral elements are used to mesh all domains. Smaller mesh

elements are used in the region where sphere gets close to the channel to capture the more complex dynamics in this region.

To validate the use of the CFD model in predicting the resistance coefficients, a comparison with the resistance coefficients reported by Higdon and Muldowney [48] is conducted. Higdon and Muldowney [48] calculated diagonal elements of the resistance matrix for the force free swimming condition for various D_{sph}/D_{ch} ratios using the following relationship:

$$\begin{bmatrix} F_x \\ F_y \\ F_z \end{bmatrix} = C\mu r_{sph} \begin{bmatrix} F_{xx}^{tt} & 0 & 0 \\ 0 & F_{yy}^{tt} & 0 \\ 0 & 0 & F_{zz}^{tt} \end{bmatrix} \begin{bmatrix} U_x \\ U_y \\ U_z \end{bmatrix} + C\mu r_{sph} \begin{bmatrix} R_p \end{bmatrix} \begin{bmatrix} 0 \\ 0 \\ U_0 \end{bmatrix} \tag{24}$$

In the scope of this thesis, second term on the right-hand side becomes zero since the fluid is quiescent. Zhu et al. [50] studied the motion of spherical particle in capillary tube using boundary element method and they used the resistance coefficients reported by Higdon and Muldowney [48] for the eccentric sphere-cylindrical channel configuration with $D_{sph}/D_{ch} = 0.4$ to validate their results. Resistance coefficients for the same configuration are calculated using the CFD model and validated against the same set of solutions reported by Higdon and Muldowney [48]. Results are plotted against β, which quantifies the sphere-wall proximity with the following equation:

$$\beta = \frac{R}{r_{ch} - r_{sph}} \tag{25}$$

where R is the distance measured from the center of the sphere to the central axis of the cylindrical channel. Average degrees of freedom (DOF) for the results reported in Figure 3.5 is 500K as mesh convergence of the results are observed beyond this value (Figure 3.6). Percentage errors for all three components of the drag force are found to be less than 0.5 at 500K DOF.
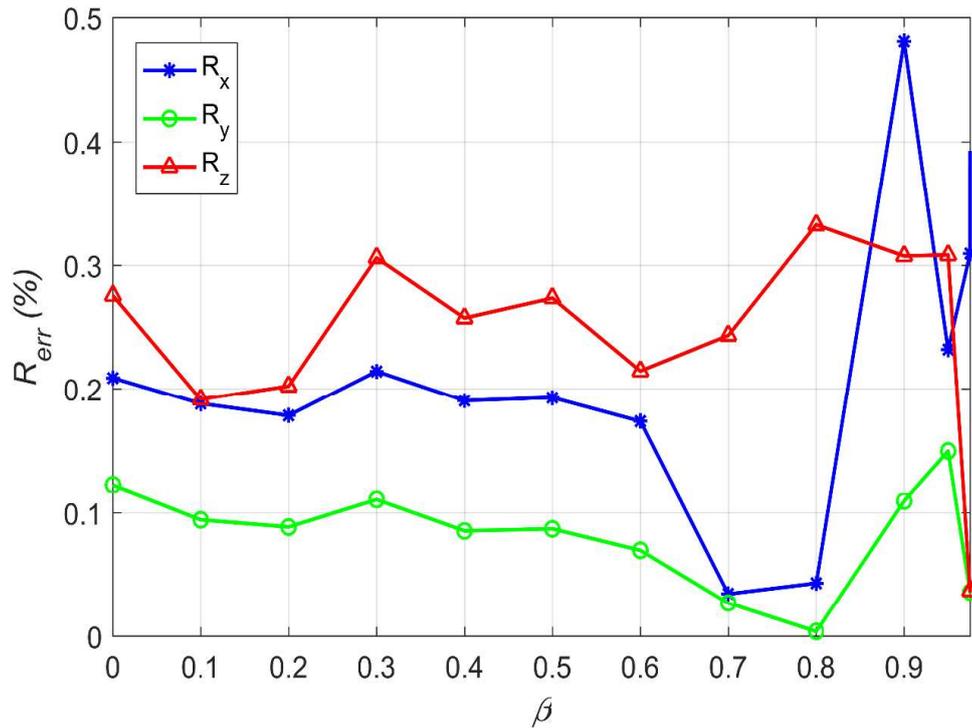
Figure 3.5 Relative error between the resistance coefficients calculated using the CFD model and Higdon and Muldowney's [48] work for $D_{sph}/D_{ch} = 0.4$ as chosen in Zhu et al.'s work [50] for comparison.
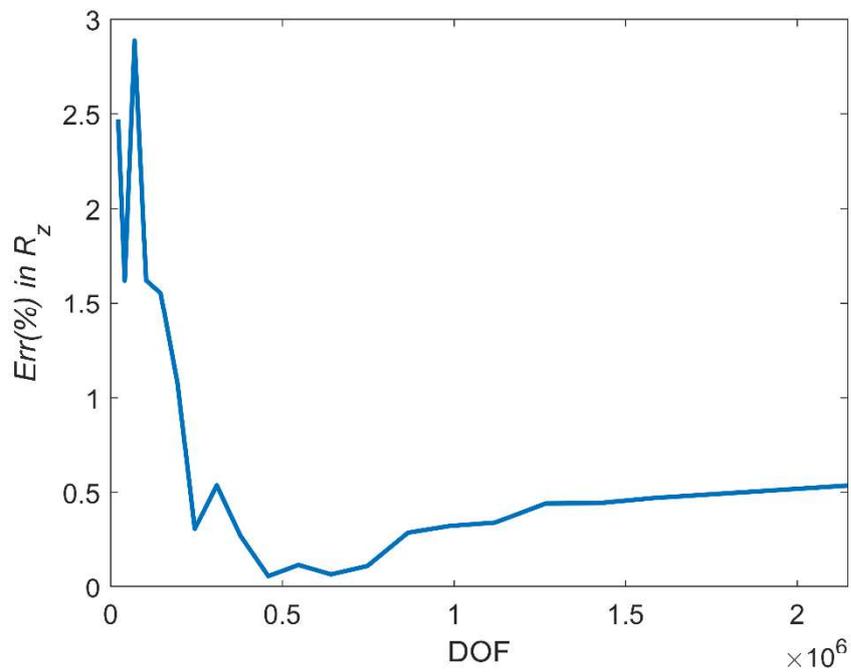
Figure 3.6 Mesh convergence study for the CFD model used in calculating the resistance coefficients. Results are represented with the error in R_z.

Following the validation, the CFD model is used to obtain full matrices of translation, rotation, and rotation-translation coupling resistance coefficients of the spheres in configurations D_{ch}/D_{sph} =1.6 and D_{ch}/D_{sph} =3, for a range of β values. Work reporting the entries of full matrices of resistance coefficients, including the translation-rotation coupling coefficients in the literature is limited to Bhattacharya et al. [49], where the authors used separable basis solutions to calculate translational, rotational and coupling resistance coefficients of a spherical particle swimming inside cylindrical conduits of various D_{ch}/D_{sph} ratios. Resistance coefficients calculated in this study are validated against the results reported by Bhattacharya et al. [49]. CFD solutions are obtained for the sphere whose center is positioned at (0, 0, R_{ch}-R_{sph}-δ). The reference position is matched to (ρ, θ, x) in cylindrical coordinates (Figure 3.7).
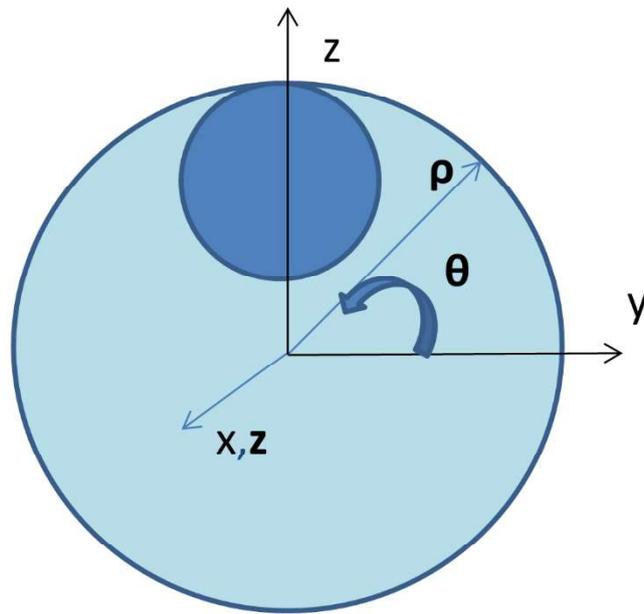
Figure 3.7 Cartesian coordinate axes used in the CFD model vs. cylindrical coordinate axes (bold) used by Bhattacharya [49]. β-axis is denoted as θ-axis to avoid confusion with β in equation 25.

The CFD study showed that the translation in directions (and rotation about those) other than the direction of the principal axes are negligible. Therefore, only the diagonal elements of the translational and rotational resistance matrices are considered. Significant rotation-translation coupling is observed only for translation along ρ-axis and rotation about θ-axis (and vice versa). With only the dominant terms, the resistance matrix takes the form:

$$
\begin{bmatrix}
F_{\rho\rho}^{tt} & 0 & 0 & 0 & G' & 0 \\
0 & F_{\theta\theta}^{tt} & 0 & G & 0 & 0 \\
0 & 0 & F_{xx}^{tt} & 0 & 0 & 0 \\
0 & G & 0 & F_{\rho\rho}^{rr} & 0 & 0 \\
G' & 0 & 0 & 0 & F_{\theta\theta}^{rr} & 0 \\
0 & 0 & 0 & 0 & 0 & F_{xx}^{rr}
\end{bmatrix}
\begin{bmatrix}
U_\rho \\ U_\theta \\ U_x \\ \omega_\rho \\ \omega_\theta \\ \omega_x
\end{bmatrix}
=
\begin{bmatrix}
F_\rho \\ F_\theta \\ F_x \\ T_\rho \\ T_\theta \\ T_x
\end{bmatrix}_{visc}
\tag{26}
$$

The resistance coefficients are obtained from the CFD model by using the boundary conditions listed in Table 3.2. Coefficients obtained for the channel diameter to sphere diameter ratio of 3 are plotted against various β values and compared to the values reported in Bhattacharya et al. [49] in Figure 3.8 after being normalized using equations 27-30:

$$
\overline{F}^{tt} = F^{tt} / (6\pi\mu r_{sph})
\tag{27}
$$

$$
\overline{F}^{rr} = F^{rr} / (8\pi\mu r_{sph}^3)
\tag{28}
$$

$$
\overline{F}^{tr} = F^{tr} / (\mu r_{sph}^2)
\tag{29}
$$

$$
\overline{F}_{ij}^{rt} = \overline{F}_{ji}^{tr}
\tag{30}
$$

All of the resistance coefficients calculated using the CFD model except for $\overline{G}$ are in perfect agreement with the coefficients reported in Bhattacharya et al. [49]. This coefficient relates rotation about x-axis to the force experienced in y-direction and relates the torque experienced in x-direction due to translation in y-direction. Bhattacharya et al. [49] attribute their results to the tug-of-war between the lubrication stresses increasing with the increased proximity to the wall as β increases and the force created in the azimuthal direction (y-direction) due to the angular variation in the pressure fields. The coefficients calculated using the CFD model, however, are found to be in good agreement with the lubrication theory at very high β values and its application demonstrated by Higdon [48]. Furthermore, the kinematic model explained in the previous section predicts the experimental results presented in the next section very accurately. Therefore, this discrepancy between the two results remains to be explained. Resistance coefficients for both channel diameter to sphere diameter ratios adopted in the scope of this thesis are depicted in Figure 3.9.

Table 3.2 Operational parameters used to obtain the resistance coefficients from the CFD model. Left column indicates the prescribed translational and angular velocities applied to the sphere surface as a moving wall boundary condition. Right column presents the equations obtained with the applied condition.

Inputs						Outputs
U_ρ	U_θ	U_x	ω_ρ	ω_θ	ω_x	Equations
1	0	0	0	0	0	$F_{\rho\rho}^{tt} = F_\rho$, $G^{'} = T_\theta$
0	1	0	0	0	0	$F_{\theta\theta}^{tt} = F_\theta$, $G = T_\rho$
0	0	1	0	0	0	$F_{xx}^{tt} = F_x$
0	0	0	1	0	0	$G = F_\theta$, $F_{\rho\rho}^{rr} = T_\rho$
0	0	0	0	1	0	$G^{'} = F_\theta$, $F_{\theta\theta}^{rr} = T_\theta$
0	0	0	0	0	1	$F_{xx}^{rr} = T_x$
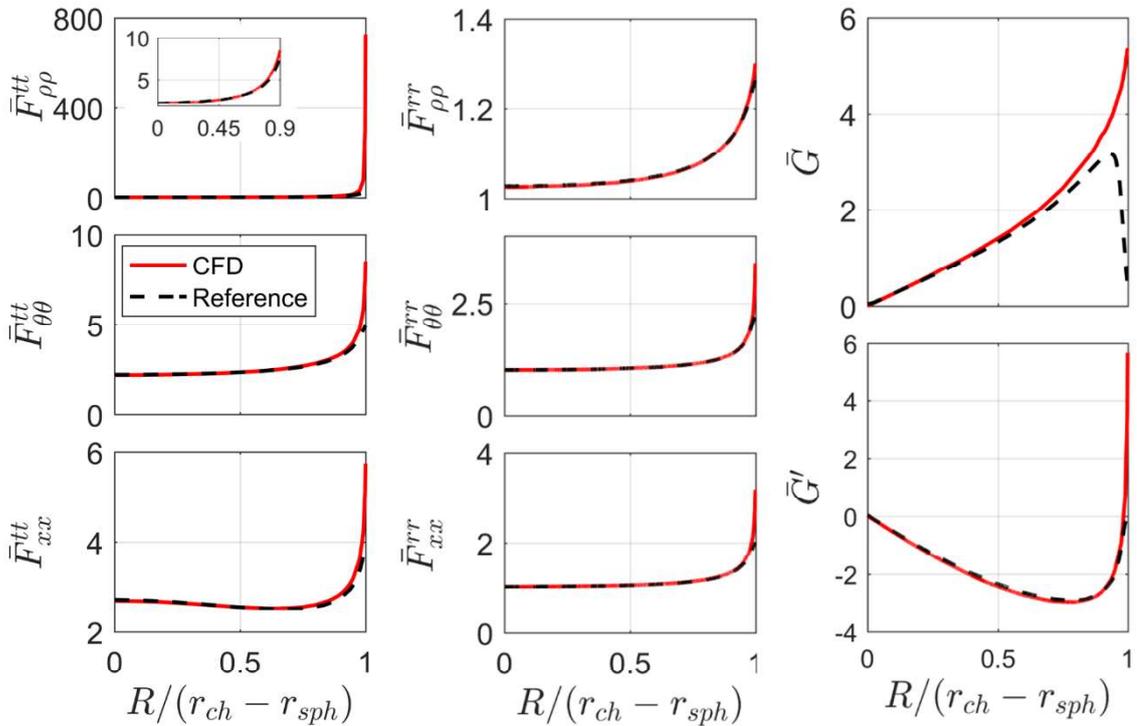
Figure 3.8 Comparison of the resistance coefficients obtained from the CFD model to the coefficients reported in Bhattacharya's work [49] for D_{ch}/D_{sph} = 3. Direct comparison for the case D_{ch}/D_{sph} = 1.6 is not possible as Bhattacharya [49] did not provide data for this ratio.
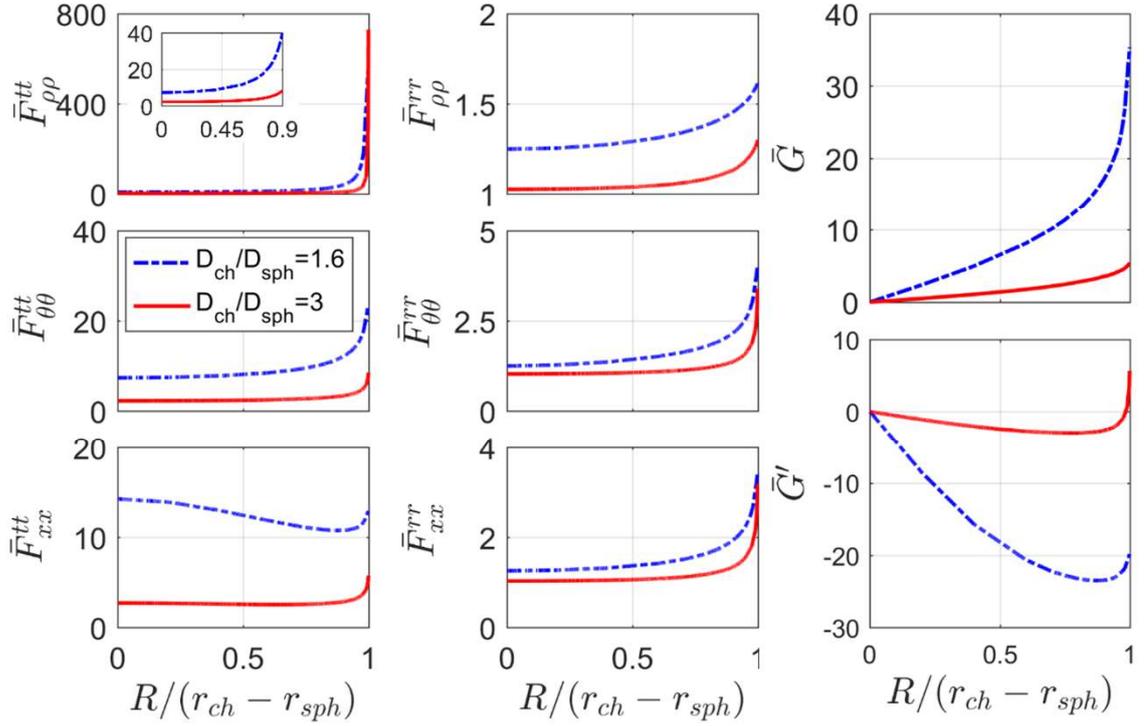
Figure 3.9 Resistance coefficients obtained using CFD model for D_{ch}/D_{sph} = 1.6 and D_{ch}/D_{sph} = 3.

3.2. Results

3.2.1. Experimental Results

This section reports the velocities and trajectories of the spheres obtained through image processing. Average lateral velocities of the spheres inside cylindrical channels are plotted against the frequency. Spheres are subjected to magnetic fields rotating about either x-axis or y-axis. Upon rotation about y-axis, spheres are observed to be "rolling", i.e. translating in positive x-direction as they are rotated clockwise about y-axis when D_{ch}/D_{sph} = 3. Translation in opposite to the rolling direction, which is referred to as "sliding", is observed as a response to clockwise rotation about y-axis when D_{ch}/D_{sph} = 1.6. When magnetic field rotating about x-axis is used to actuate the spheres, depending

on the strength of the magnetic field gradient along x-axis, the sphere either orbits the central axis of the cylindrical channel or translates along x-axis following a helical trajectory. In the tighter configuration, spheres are observed to be sliding along the channel wall while following a helical path. At small frequencies, the spheres in D_{ch}/D_{sph} = 1.6 configurations are observed to migrate towards the channel axis, i.e. move in the negative radial direction. As the frequency of the rotating magnetic field is increased and magnetic field gradient along the x-axis is modified, spheres are successfully focused on the central axis of the cylindrical channel.

3.2.1.1. Rotation about y-axis

Velocity of the (U_{sph}) sphere with 1mm diameter translating along x-axis inside the cylindrical channel of diameter 3 mm is plotted against the magnetic field rotation frequency in Figure 3.10a. Blue curve (with star markers) depicts the results for silicon oil with viscosity 1 Pa.s, and the red curve (circular markers) is for μ= 0.5 Pa.s. At higher viscosity, the velocity increases linearly with increasing rotation frequencies up to 8 Hz, where it reaches the maximum velocity of 1.16 mm/s. As the rotation frequency is increased beyond this value, magnetic moment of the sphere fails to rotate synchronously with the rotating magnetic field, thus the sphere decelerates almost linearly with increasing frequency up to 16 Hz. Above 16 Hz, the decrease in the velocity slows down, and the velocity converges to zero around 50 Hz.

In the lower viscosity silicone oil, lateral velocity increases linearly up to the frequency of 3 Hz, however, the increase becomes slower after this point and continues up to 16 Hz, where the maximum velocity of 1.09 mm/s is reached. Beyond 16 Hz, velocity drops slowly to zero as the frequency increases. Up to 3 Hz, velocities achieved in silicone oil of two different viscosities are similar.
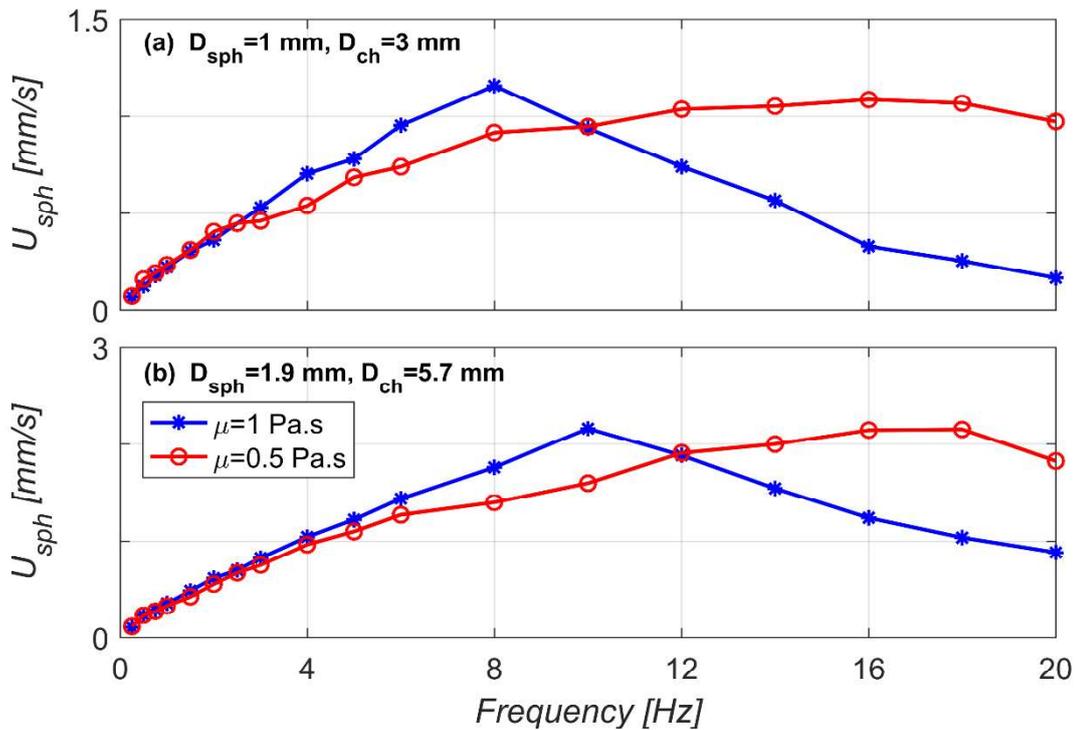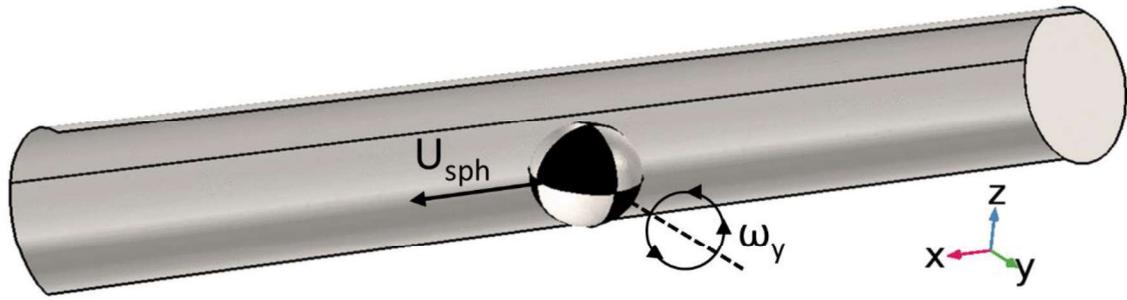
Figure 3.10 Swimmer velocity vs. magnetic field rotation frequency plotted for the silicone oil viscosities of μ= 1 Pa.s and μ= 0.5 Pa.s for the configurations a) D_{sph} = 1 mm, D_{ch} = 3 mm, and b) D_{sph} = 1.9 mm, D_{ch} = 5.7 mm where D_{ch}/D_{sph} ratio is 3

Figure 3.10b depicts the velocity profile for the 1.9 mm sphere inside the channel with 5.7 mm diameter, for two different viscosities of the silicone oil. Similar velocity profiles compared to Figure 3.10a are observed, however, it must be noted that the bigger sphere (Figure 3.10b) achieves higher lateral velocities despite the similar D_{ch}/D_{sph} ratio due to its weight. Highest velocity is reached at 10 Hz, with U_{sph} = 2.16 mm/s in higher viscosity silicone oil. Maximum velocity in 0.5 Pa.s silicone oil is 2.15 mm/s and observed at 18 Hz. Effect of different viscosity becomes observable at frequencies higher than 4 Hz.

Spheres' lateral velocities are lower than ωr_{sph} at all frequencies. In fact, they are one tenth of the contact rolling velocities at the highest (Figure 3.11). This behavior is

attributed to the lost traction due to the increasing pressure difference between the front and the wake of the sphere. As the sphere rotates faster, pressure builds up and pushes the sphere back, however, due to the relatively larger D_{ch}/D_{sph} ratio, it does not reach levels that would change the direction of translation (Figure 3.12).
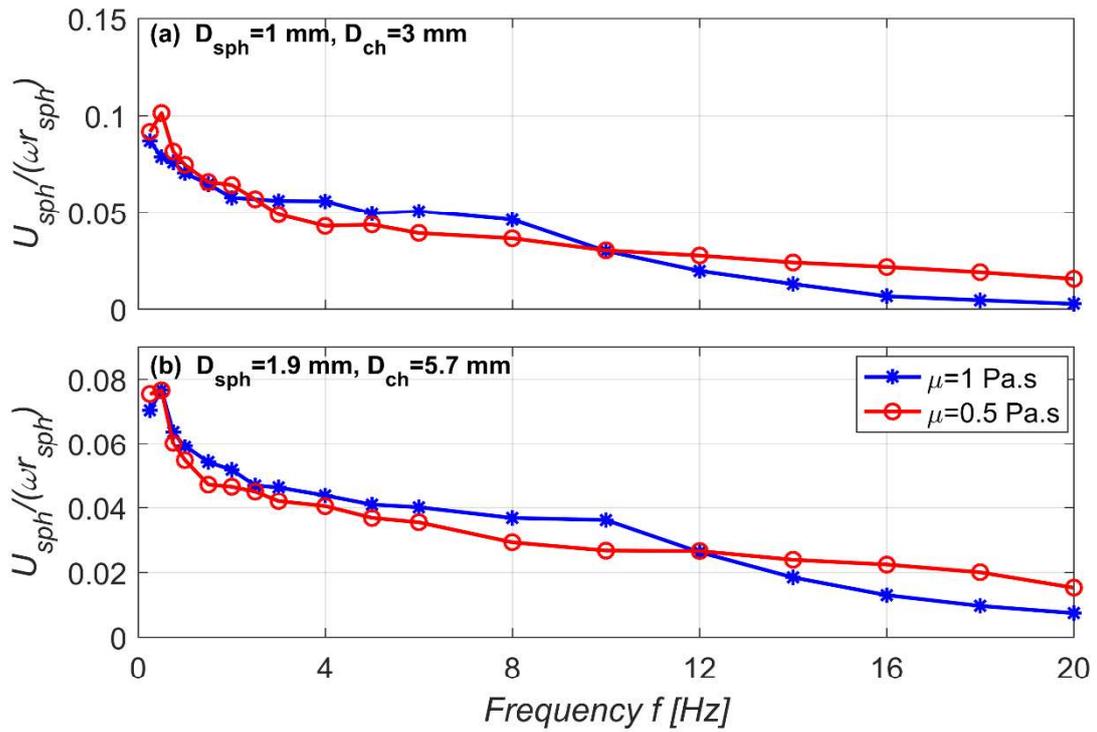
Figure 3.11 Swimmer velocity normalized with contact rolling velocity vs. magnetic field rotation frequency plotted for the silicone oil viscosities of μ= 1 Pa.s and μ= 0.5 Pa.s for the configurations a) D_{sph} = 1 mm, D_{ch} = 3 mm, and b) D_{sph} = 1.9 mm, D_{ch} = 5.7 mm where D_{ch}/D_{sph} ratio is 3
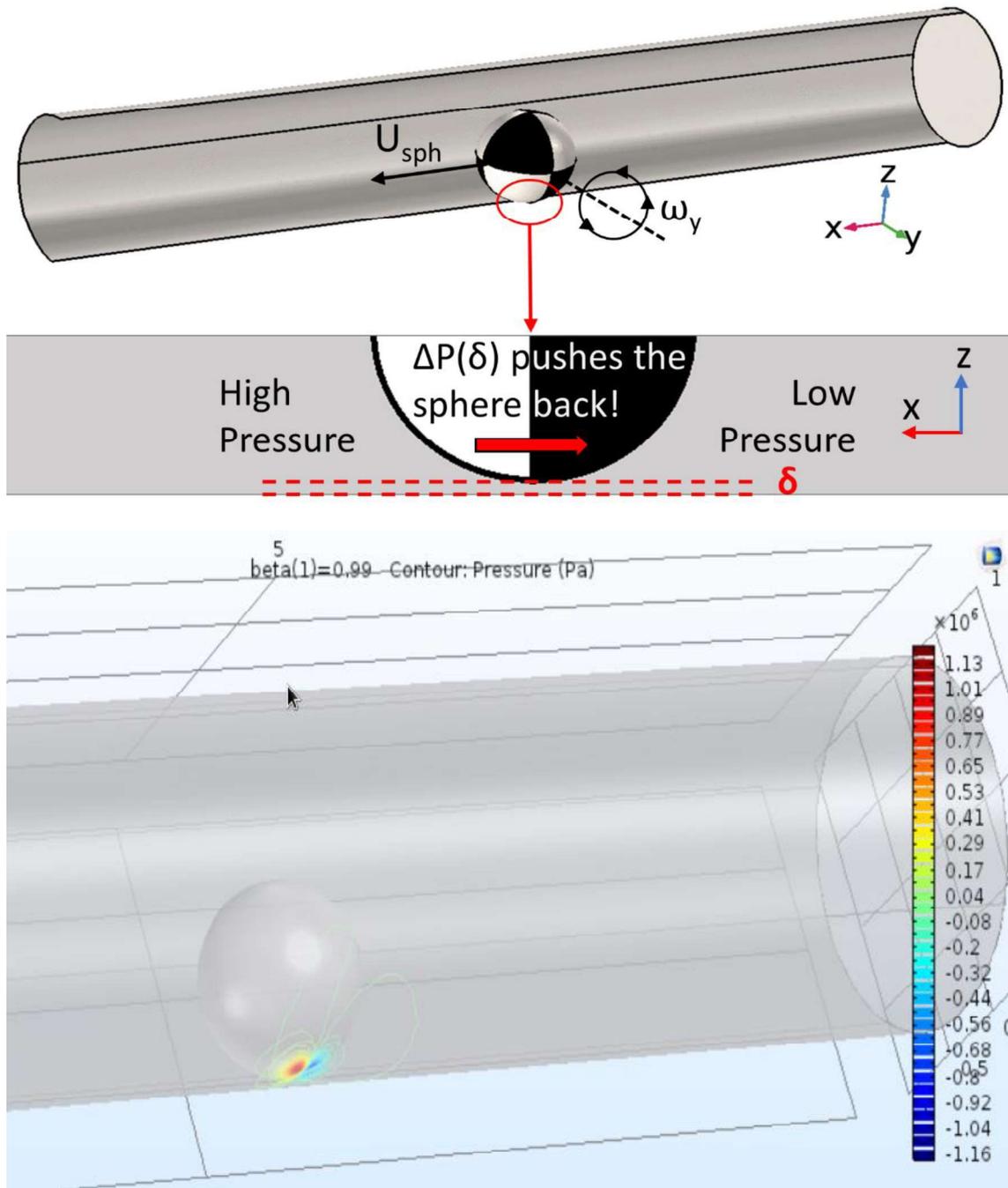
Figure 3.12 Close up visualization of the wall-sphere separation and effect of the pressure gradient between the front and the wake of the sphere

In our study, a decrease in velocity with decreasing viscosity is reported. This behavior is attributed to the dependence of ΔP depicted in Figure 3.12 on viscosity and δ. δ is a function of ΔP and $m_{sph}g$ and it is inversely proportional to both these quantities. As the viscosity decreases, δ decreases, therefore ΔP increases. The rolling sphere loses more traction, hence a decrease in velocity is observed with decreasing viscosity.

In the literature, this behavior is also attributed to the difference in the apparent (measured) viscosity and the viscosity experienced by the swimmer, when the fluid medium is a polymer solution. Berg and Turner [98] argue that the solute in the polymeric fluids form a "quasi-rigid network easily penetrated by particles of microscopic size". The authors report the results of experiments with two different fluid media with the same apparent viscosities to demonstrate the difference of the apparent viscosity from the actual viscosity experienced by the swimmer. Magariyama and Kudo [99] prepared a mathematical model of Berg and Turner's argument. They argue that the viscosity term in calculating the translational and rotational drag forces require a correction. Namely they suggest that the perceived viscosity is not different only from the measured viscosity, but that it changes also for translational and rotational motions of the same swimmer in the same fluid. The slight decrease in the velocity with decreasing viscosity observed in our experiments can be thus attributed to two other reasons: 1) Our fluid medium is silicone oil, which is a solution of polydimethylsiloxane (PDMS) polymer; thus, the sphere might experience a different rotational viscosity than the measured viscosity according to Magariyama and Kudo [99], and 2) the change in distance between the sphere and the channel wall, δ, might be the cause for the similar velocities if the lift force experienced by the sphere due to the hydrodynamics interactions that occur due to the proximity to the wall (which is not quantified for the spheres inside cylindrical conduits yet) is dependent on the viscosity.
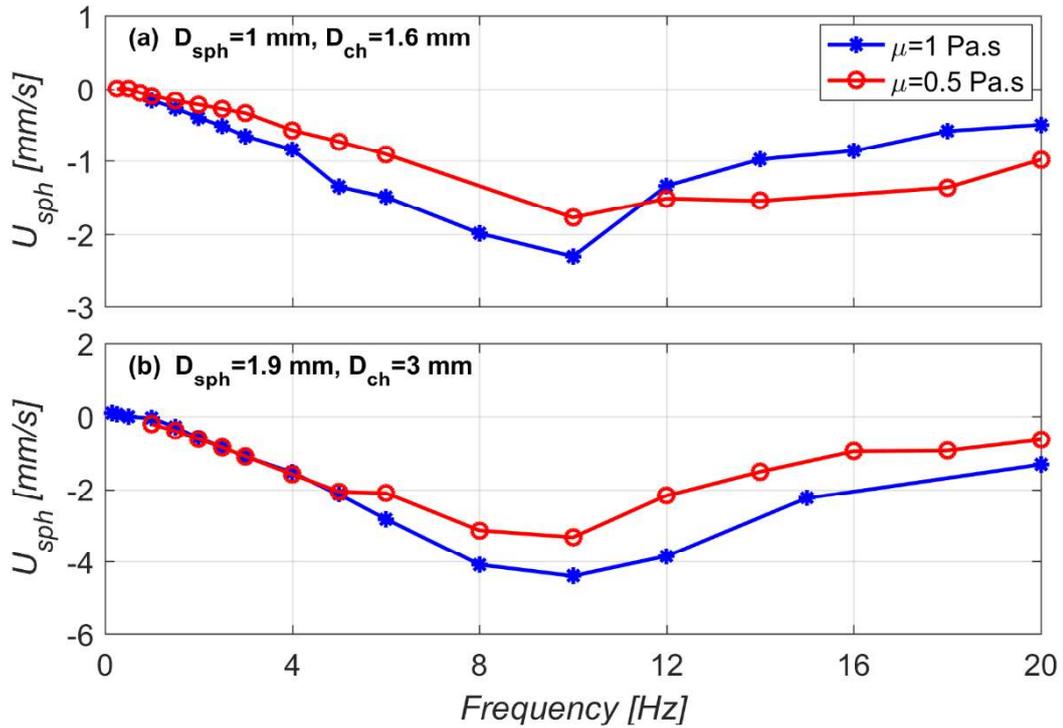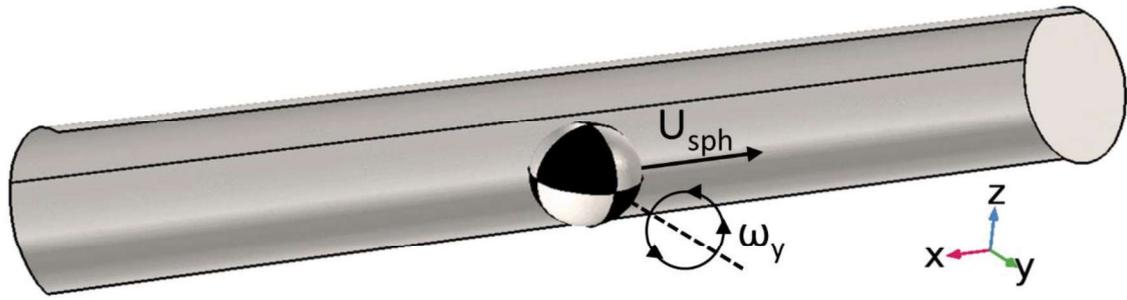
Figure 3.13 Swimmer velocity vs. magnetic field rotation frequency plotted for the silicone oil viscosities of $\mu = 1$ Pa.s and $\mu = 0.5$ Pa.s for the configurations a) $D_{sph} = 1$ mm, $D_{ch} = 1.6$ mm, and b) $D_{sph} = 1.9$ mm, $D_{ch} = 3$ mm where D_{ch}/D_{sph} ratio is 1.6

Lateral velocities of the spheres of diameters 1 mm and 1.9 mm, in cylindrical glass channels of diameters 1.6 mm and 3 mm respectively, are plotted against frequency for two different viscosities of silicone oil in Figure 3.13. All lateral velocities are observed to be negative, except for the velocities obtained at very small frequencies under 0.5 Hz. Highest speed in the negative x-direction achieved by the 1 mm sphere is -2.31 mm/s, which occurs at 10 Hz and in 1 Pa.s silicone oil (Figure 3.13a). Velocity profile is linear up to 10 Hz, similar to the trend observed in Figure 3.11a. In 0.5 Pa.s silicone oil the maximum speed attained opposite to rolling direction is 1.09 mm/s for the sphere of diameter 1 mm. It is observed that the velocities are very similar for both viscosities, as

also observed for the rolling spheres. Velocity profile of the sphere with 1.9 mm diameter is depicted in Figure 3.13b. It is observed that step out occurs for frequencies above 10 Hz in both viscosities. Maximum speeds reached are 4.40 mm/s and 3.33 mm/s for 1 Pa.s and 0.5 Pa.s silicone oils respectively. An almost linear increase in the speed is observed with the increase in frequency up to the step-out frequency. Velocities obtained by the larger sphere with diameter 1.9 mm are almost double the velocities obtained by the smaller sphere of diameter 1 mm.

Translation opposite to rolling direction, which is referred to as "sliding" in this work, is attributed to the large pressure difference between the front and the wake of the sphere. Contrary to the experiments with $D_{ch}/D_{sph} = 3$ where 2/3 of the channel cross-section is not blocked by the sphere, at the ratio $D_{ch}/D_{sph} = 1.6$ more than 2/3 of the channel cross section is blocked. In the case of a larger ratio, pressure build up still occurs due to the asymmetry of the distances between the sphere and the channel wall in $z = R_{ch}$ and $z = -R_{ch}$ coordinates, but it is partially and easier relieved compared to the configuration with the tighter confinement. At very low frequencies, the pressure build-up is not strong enough to change the spheres' direction even at $D_{ch}/D_{sph} = 1.6$ configuration. However, as the sphere rotates faster, ΔP (depicted in Figure 3.12) increases to a point where it effectively pushes the spheres opposite to the rolling direction.

Figure 3.14 depicts U_{sph} normalized with the contact rolling velocity ωr_{sph}. Similar to the rolling spheres, an almost linear decrease in the magnitude is observed.
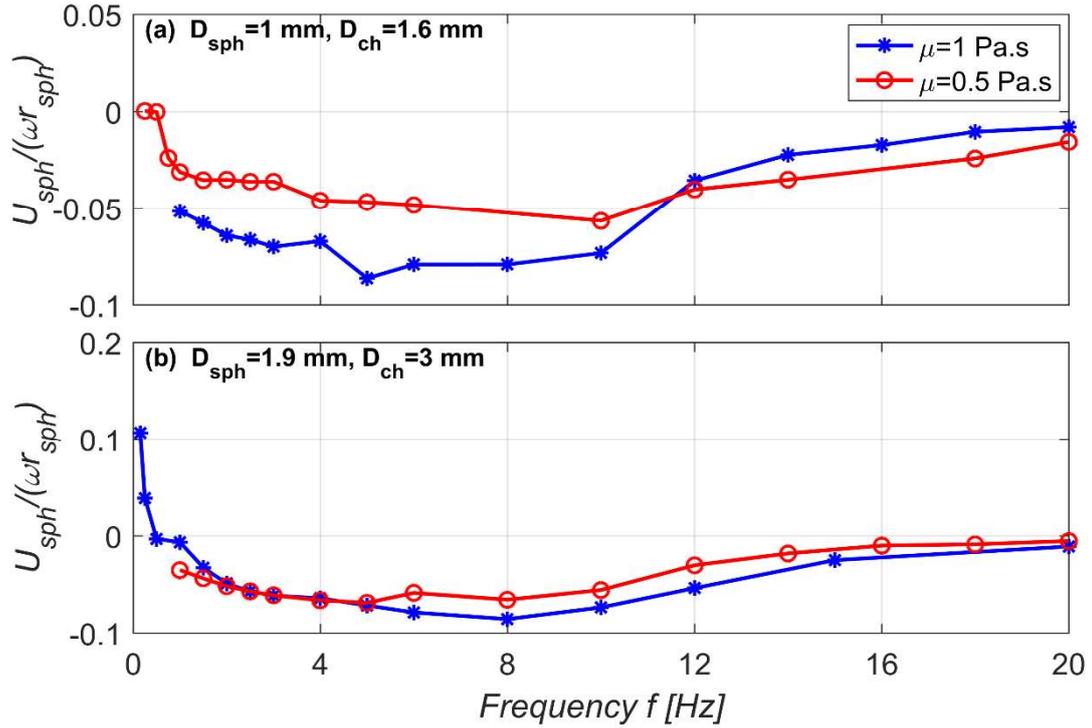
Figure 3.14 Swimmer velocity normalized with contact rolling velocity vs. magnetic field rotation frequency plotted for the silicone oil viscosities of μ= 1 Pa.s and μ= 0.5 Pa.s for the configurations a) D_{sph} = 1 mm, D_{ch} = 3 mm, and b) D_{sph} = 1.9 mm, D_{ch} = 5.7 mm where D_{ch}/D_{sph} ratio is 3

3.2.1.2. Rotation about x-axis

To understand the dynamics of the sphere rotating inside the cylindrical channel, its motion while rotating about the x-axis is observed. The results reported in this section are observed for the spheres of 1 mm and 1.9 mm both, with the channel diameter to sphere diameter ratio of D_{ch}/D_{sph} = 1.6.

In the first case, the sphere is rotated about x-axis as demonstrated in Figure 3.15 by activating the Helmholtz coil pairs along y-axis and z-axis with 90° phase difference as explained in section 3.1.1.1. Starting from 0.25 Hz, frequency is increased until a stable and observable trajectory is obtained. At and above the frequency of 6 Hz, it is observed that the sphere follows a circular trajectory by sliding along the channel wall as shown in Figure 3.15. No magnetic field in x-direction is applied in this experiment. For the

76

frequencies including and above 6 Hz, both smaller and larger spheres follow and repeat full circular trajectories without translating in x-direction. It is noted that the frequency at which the sphere "orbits" the central axis of the cylindrical channel is different from the frequency of the magnetic field rotating about x-axis.
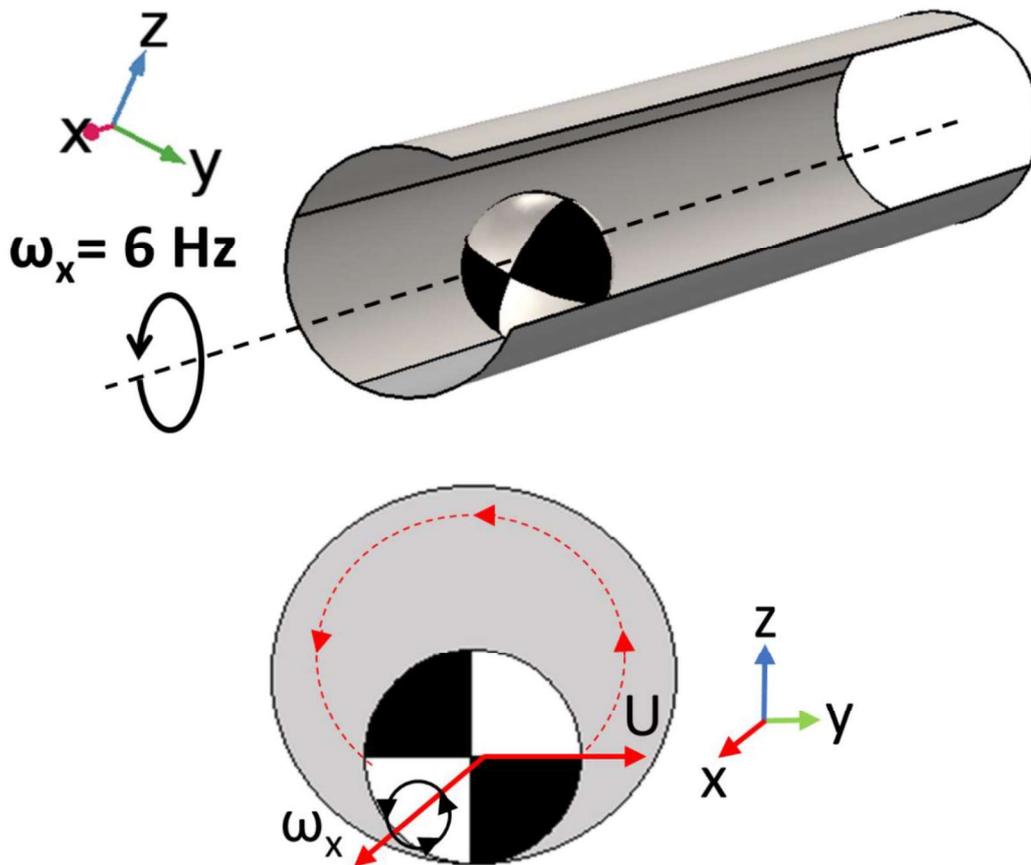
Figure 3.15 Visualization of the rotation of the sphere about x-axis under a magnetic field rotation frequency 6 Hz. No magnetic field gradient along x-axis is applied in this experiment.

After this observation, motion of the sphere rotating about x-axis is studied under the presence of a magnetic field gradient in x-direction. Both coils along x-axis are activated to apply 1 mT magnetic field (measured at the center) for this experiment and a magnetic field strength along x-axis that peaks at the center of the channel is obtained as shown in red in Figure 3.16. The experiments showed that in this case the sphere translates in x-direction following a helical trajectory by sliding along the channel walls towards the center of the channel. Wavelength of the helical trajectory gets smaller as the sphere

approaches the center and once the center is reached, the sphere starts to follow a circular trajectory as translation velocity in x-direction approaches zero. This behavior is attributed to the stronger synchronization of the magnetic dipole moment the sphere and the applied magnetic field at the center, where the magnetic field strength peaks. This behavior is highly desirable for drug delivery applications. The spheres settle where the magnetic field gradient is zero, therefore one can exploit this behavior to accumulate the spheres in the targeted region.
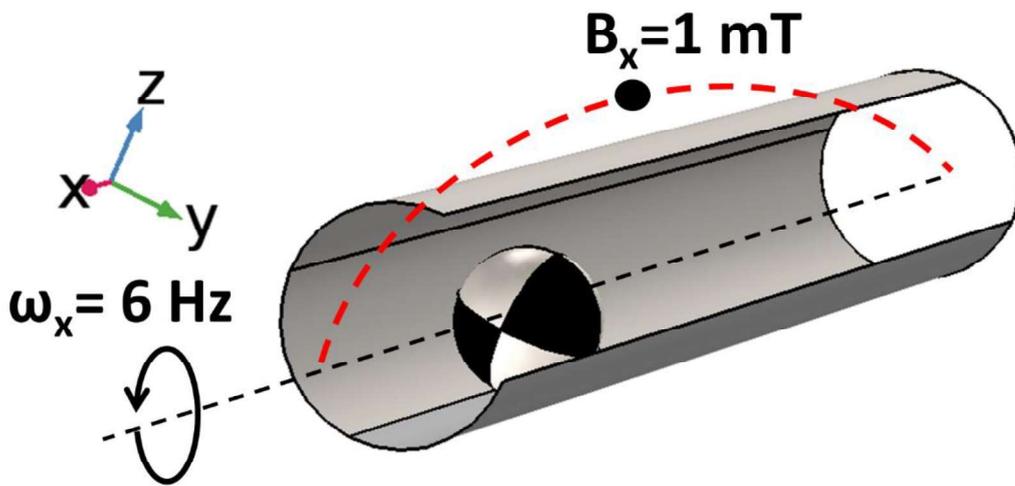
Figure 3.16 Visualization of the rotation of the sphere about x-axis under a magnetic field rotation frequency 6 Hz. Parabolic magnetic field along x-axis is applied in this experiment.

After establishing that the sphere following a circular path along the channel wall can be made to translate in x-axis, magnetic field in x-axis is modified such that the sphere can swim the full length of the channel. It is observed that a constant magnetic field should be applied in x-direction. As demonstrated in Figure 3.17, the sphere is made to traverse the entire length of the channel. Another observation made during this experiment is that the radius of the helical trajectory decays over time. A slight but noticeable change in the helical trajectory radius towards the end of the channel indicates that the magnetic field gradient plays an important role in the characteristics of this motion.
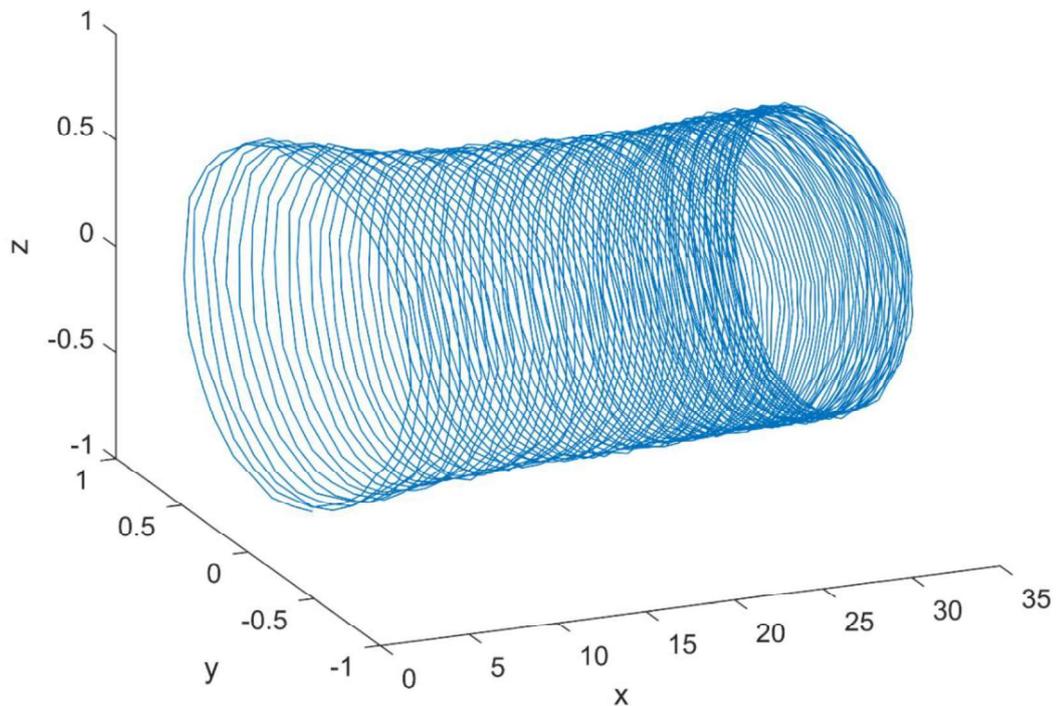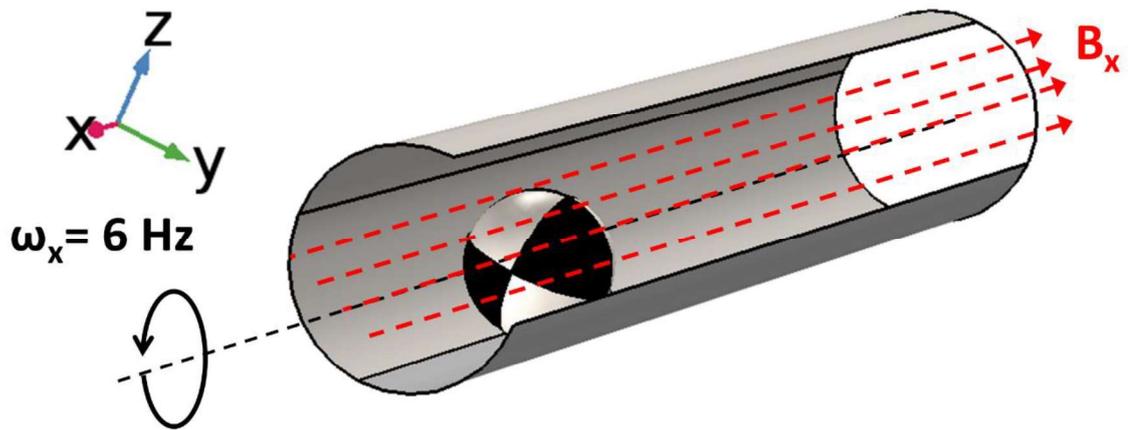
Figure 3.17 Visualization of the rotation of the sphere about x-axis under a magnetic field rotation frequency 6 Hz, following a helical trajectory under constant magnetic field application along x-axis.

Next, the effects of the changes in magnetic field gradient on the sphere's swimming characteristics are studied. A set of three experiments are conducted. Rotating magnetic field about the x-axis is set to the frequency of 6 Hz for each case (at which the helical trajectory is starts to be observed) while the magnetic field applied in x-direction is provided by only one of the coils along the x-axis, thus creating a decaying magnetic field strength as the sphere moves away from the coil. Namely, in this case, the sphere is

being "pushed" away from the activated coil along the x-axis. The strength of the magnetic field along x-axis is set to 1 mT, 2 mT and 3 mT respectively for each case, measured in the immediate vicinity of the activated coil. As expected, translation of the sphere along x-axis slows down as the sphere moves away from the coil applying the magnetic field in x-direction (Figure 3.18,

Figure 3.19 and Figure 3.20). Rotation rate of the sphere about the cylinder axis, υ_θ, is entirely different from the rotation rate of the magnetic field about x-axis (Figure 3.22).

Two significant observations are made at the light of the results of these three experiments: 1) The translation velocity of the sphere along x-axis does not show a linear dependency on the strength of the magnetic field applied in x-direction (Figure 3.21), and 2) a stronger magnetic field in translation direction causes a more rapid decay in the radius of the helical trajectory, i.e. the amount of decay per distance travelled in x-direction is higher for the higher magnetic field strength application in translation direction (Figure 3.21). However, rate of radial migration towards the central axis of the cylinder does not show a linear dependency on the magnetic field strength along x-axis. Beyond applied magnetic field strength of 3 mT along x-axis, the sphere experiences a chaotic combination of angular velocities in three axes, and as such it fails to follow an observable and plottable trajectory as it vibrates without translating in any particular direction.

Velocities depicted in Figure 3.21 and Figure 3.22 are obtained as follows: For the velocity in x-direction, only the linear region of the position vs. time curve is considered. For the velocities in y and z-directions, maximum displacement in the chosen direction up to the saturation is considered. To estimate υ_θ, number of turns the sphere performs about the center axis of the cylinder are counted for the region where the velocity in x-direction is constant.

(a)
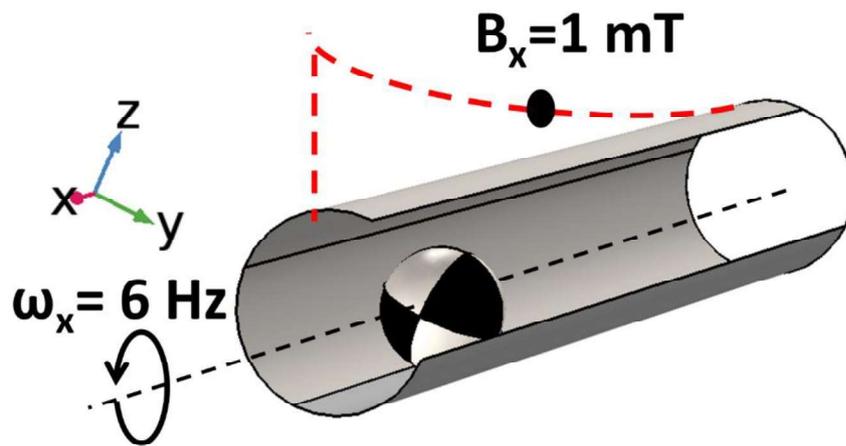
(b)
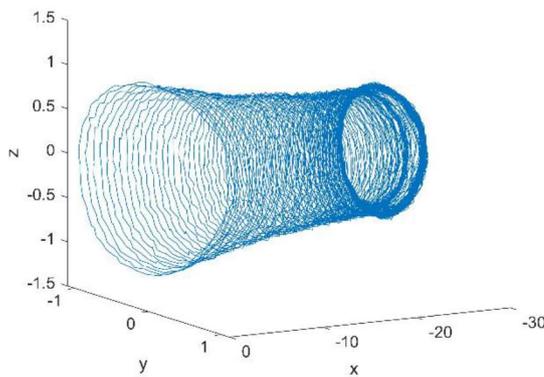
(c)
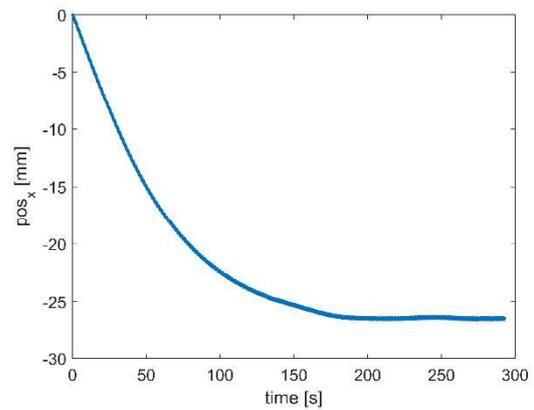
(d)
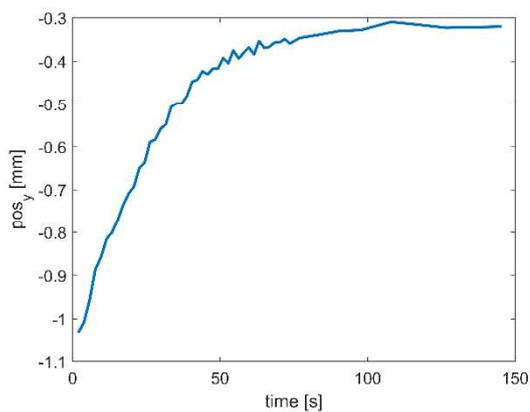
(e)
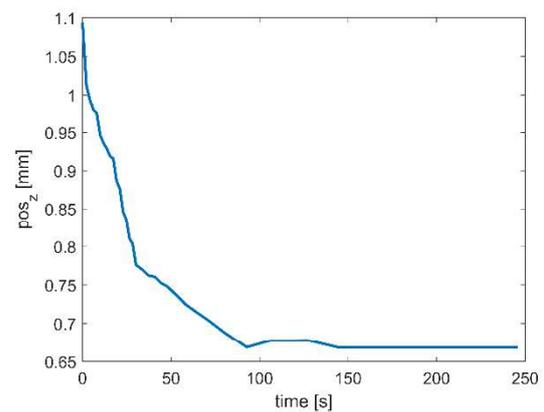

Figure 3.18 Visualization of the rotation of the sphere about x-axis under a magnetic field rotation frequency 6 Hz, following a helical trajectory under magnetic field along x-axis applied at 1 mT from the wake of the sphere only. Following the decay in the radius of the helical trajectory, the sphere starts to follow a circular path once the distance from the coil applying magnetic field in x-direction is sufficiently great.
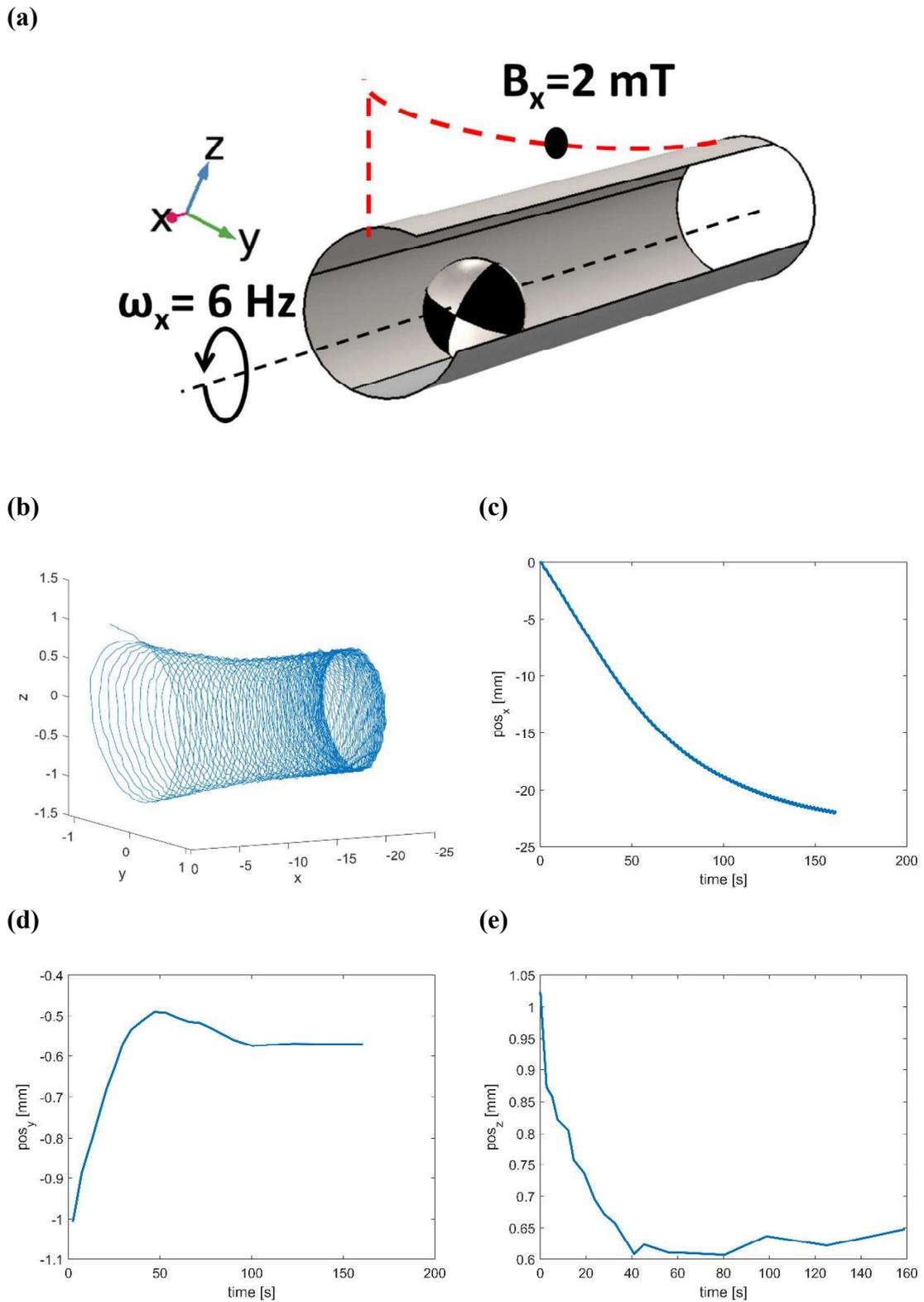
Figure 3.19 Visualization of the rotation of the sphere about x-axis under a magnetic field rotation frequency 6 Hz, following a helical trajectory under magnetic field along x-axis applied at 2 mT from the wake of the sphere only. A decay in the radius of the helical trajectory is observed as the sphere migrates towards the center of the cylindrical channel.

(a)
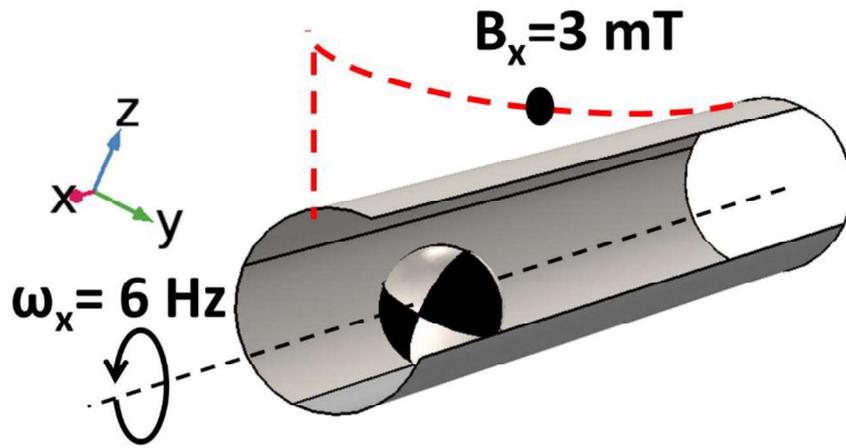
(b)
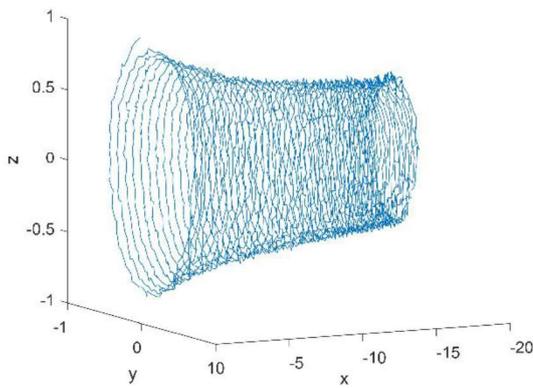

(c)
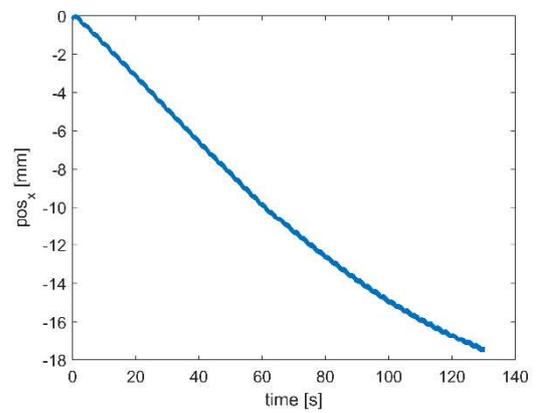
(d)
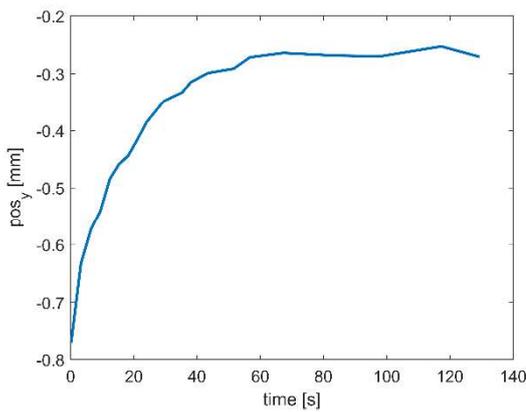
(e)
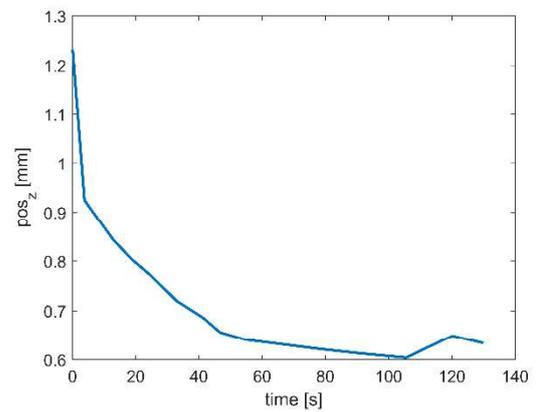
Figure 3.20 Visualization of the rotation of the sphere about x-axis under a magnetic field rotation frequency 6 Hz, following a helical trajectory under magnetic field along x-axis applied at 3mT from the wake of the sphere only. A decay in the radius of the helical trajectory is observed as the sphere migrates towards the center of the cylindrical channel. The sphere does not settle into a circular trajectory at the end of the workspace where the magnetic field applied in x-direction is still effective due to the greater magnitude applied.

83
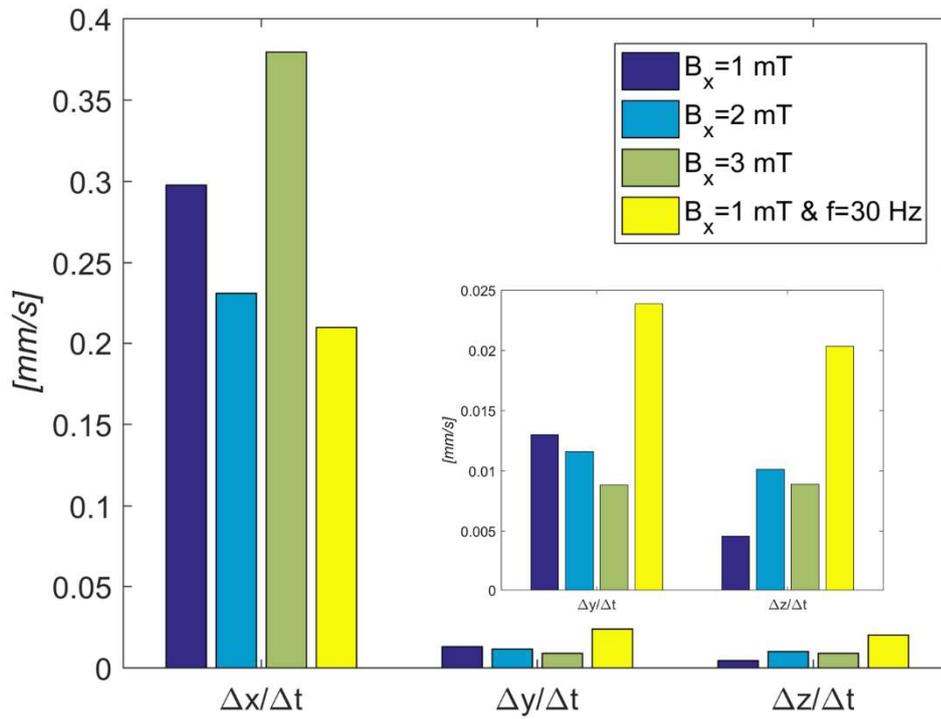
Figure 3.21 Velocities obtained by the sphere following a helical trajectory under different magnetic field gradients along x-axis.
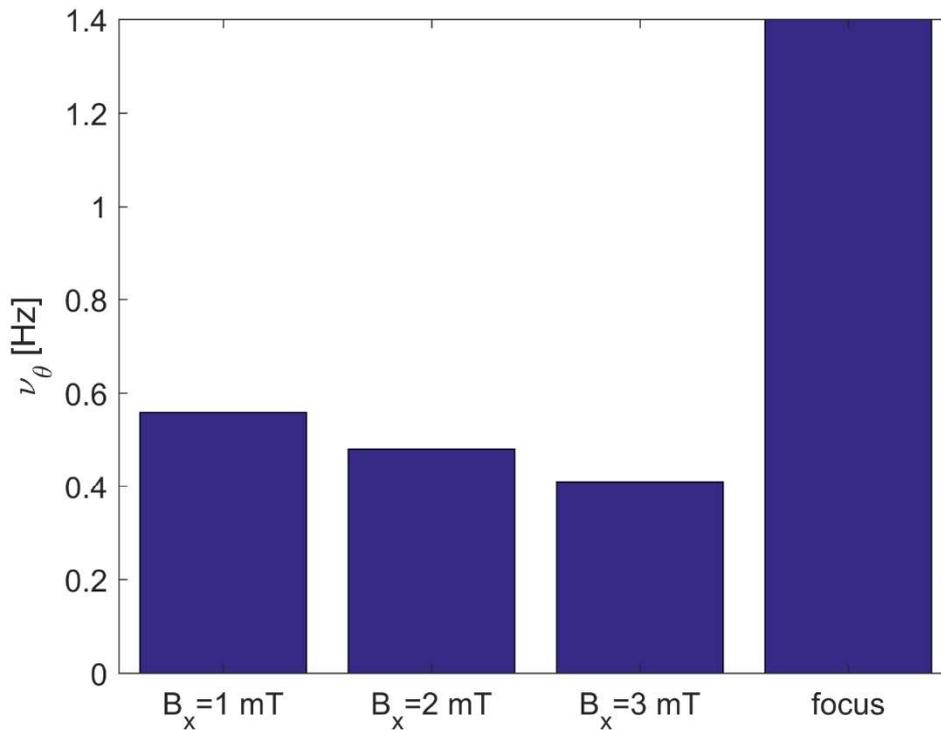
Figure 3.22 υ_θ is depicted for the test cases presented in Figure 3.18Figure 3.19,Figure 3.20 andFigure 3.23.

Lastly, the effect of the magnetic field rotation frequency on the motion of the sphere rotating about x-axis under applied magnetic field gradient along x-axis is studied. Figure 3.23 depicts the trajectory of the sphere subjected to magnetic field rotating about x-axis with a frequency of 30 Hz and a magnetic field in x-direction of strength 1 mT generated by a single coil pushing the sphere away from itself. Under these conditions, the sphere is observed to perform several helical turns of decaying radii before eventually settling down to the center of the cylindrical channel (Figure 3.23). After the sphere is focused on the center, a significant decrease in its velocity is observed, however, it is confirmed that the sphere keeps translating along x-axis. The sphere's focusing behavior is determined to be stable and responsive to changes in direction of applied magnetic field along the x-axis. Namely, once the sphere is settled on the centerline of the cylindrical conduit, it translates along the central axis even when a sudden change in the direction of applied magnetic field along the x-axis occurs. Spontaneous changes in direction causes the sphere to "wobble" for a short time and it quickly focuses on the centerline following the perturbation. This observation proves that the focusing behavior does not stem from unsteady effects and in fact that it occurs due to hydrodynamic interactions between the sphere and the channel and rotary motion of the sphere near channel boundaries. Even though the circular and helical trajectories described in Figure 3.18,

Figure 3.19 and Figure 3.20 can be obtained in the configurations where $D_{ch}/D_{sph} = 3$, focusing behavior could not be achieved despite numerous modifications to the applied magnetic fields. This behavior will be elaborated on in the following section, where the results obtained from the kinematic model are compared to the experimental results reported in this section. In none of the reported experiments that result in circular or helical trajectories the frequency at which the sphere orbits the x-axis matches the frequency of the magnetic field rotating about the x-axis. It is also noteworthy that the sphere does not experience step-out at frequencies higher than 10 Hz as it did in the experiments where the magnetic field rotating about y-axis is applied. This behavior can be attributed to the decreased resistance to rotation compared to the resistance to translation. Linear drag on the sphere is proportional to the length scale, whereas rotational drag of a sphere is proportional to the cube of the length scale. Therefore, the sphere is easier to move with rotational motion, thus it can achieve synchronous motion with the rotating magnetic field at higher magnetic field rotation frequencies.

(a)

(b)

(c)

**(d)**

(e)
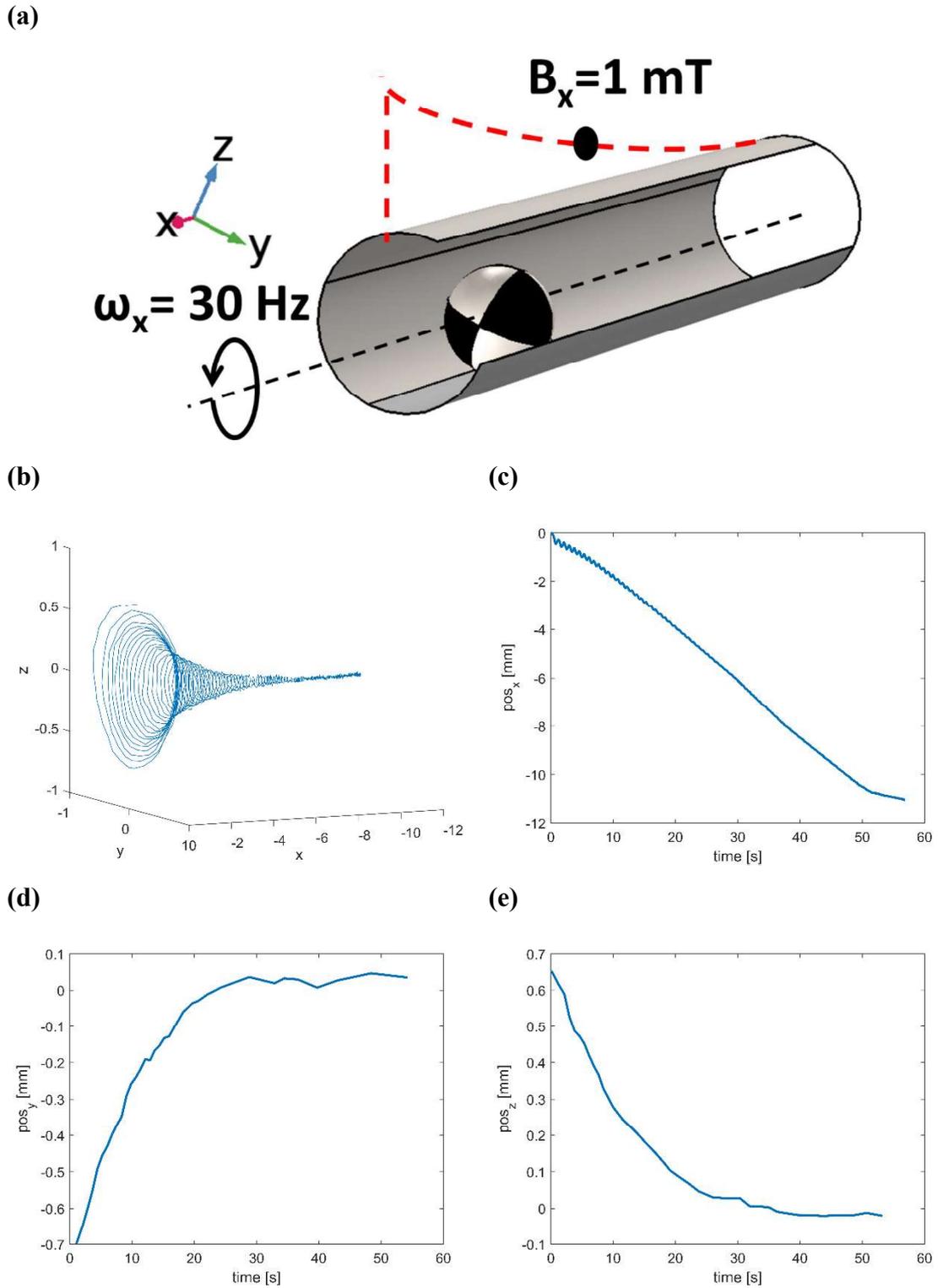
Figure 3.23 Visualization of the rotation of the sphere about x-axis under a magnetic field rotation frequency 30 Hz, following a helical trajectory under magnetic field along x-axis applied at 1 mT from the wake of the sphere only. Radius of the helical trajectory quickly converges to zero as the sphere settles down onto the central axis of the cylindrical channel.

3.2.2. Numerical Results

3.2.2.1. Rotation about y-axis

Kinematic model described in section 3.1.2.1. is used to analyze the swimming behavior of magnetically actuated spheres inside cylindrical conduits. Each of the conditions used in the experimental studies reported in the previous section are applied to the kinematic model at the initialization. In Figure 3.24, predicted translation velocities of the spheres inside cylindrical channels with channel diameter to sphere diameter ratios of $D_{ch}/D_{sph} = 3$ are plotted against the magnetic field rotation frequency. Blue curves with star markers show the experimental results whereas the red curves with circular markers depict the numerical results. Figure 3.24a and Figure 3.24c depict the results obtained for the spheres of diameter 1 mm and 1.9 mm moving in the silicone oil with a viscosity of 1 Pa.s respectively. Predicted velocities obtained using the kinematic model are in excellent agreement with the experimental results for both before and after the step-out occurs, considering that slight differences in the magnitudes are expected as the motion after region is highly irregular.

Even though the numerical results agree with the experimental results, it is observed to be less accurate at predicting the velocities of the spheres moving in silicone oil with a viscosity of 0.5 Pa.s (Figure 3.24b and 3.24d). These results are explained as follows: It is not possible to determine the distance between the sphere and the channel wall, δ, instantaneously. In the kinematic model, the sphere's initial position is defined along with the minimum distance the sphere can be located from the channel wall at any given time. This setting is not adjusted during the simulation, namely δ can change during the simulation only if the forces and torques experienced by the sphere induce a movement along radial direction. Initial setting is determined by a preliminary study where the minimum distance to the sphere wall is adjusted until the velocities of the spheres are predicted accurately at very low frequencies. This approach is based on the following reasoning: Even though an explicit expression for the lift force experienced by a sphere swimming inside a cylindrical conduit is not reported in the literature yet, existing models for spheres swimming in bulk or at higher Reynolds numbers point to a strong suggestion between an increasing angular velocity and increasing lift force. Furthermore, in the

experimental studies reported in the previous section, it is observed that the sphere moves towards the center of the channel more rapidly at higher frequencies, which suggests that the missing expression for the lift force on the spheres swimming in cylindrical conduits will have a proportional dependence on the angular velocity as well. It is expected for the kinematic model to predict the coordinates of the sphere based on the linear and rotational velocities that depend on forces and torques on the sphere. Less accurate prediction of the velocities for a smaller viscosity points to the importance of determining the correct expression for the lift force.
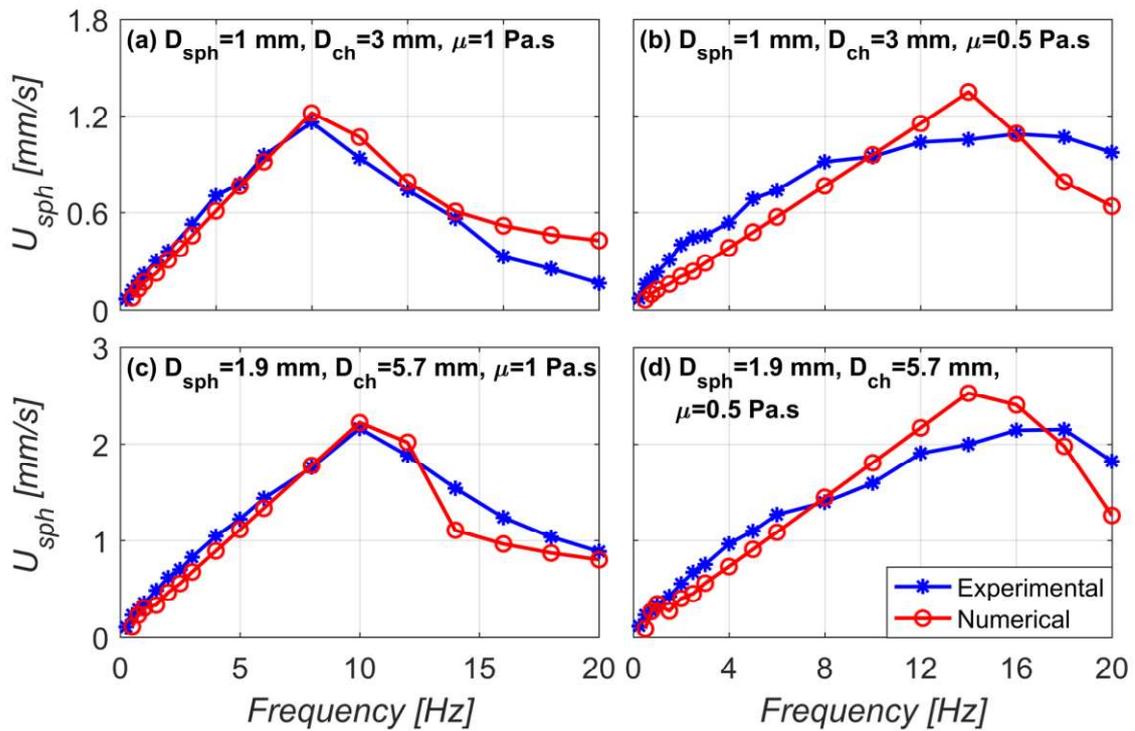
Figure 3.24 Comparison of the experimental results to the numerical predictions for $D_{ch}/D_{sph} = 3$ for two different silicone oil viscosities of $\mu = 1$ Pa.s and $\mu = 0.5$ Pa.s.

Numerical results for the confined spheres with $D_{ch}/D_{sph} = 1.6$ are compared to the experimental results in Figure 3.25. Overall, it can be observed that the results predicted by the kinematic model are in a better agreement with the experimental results for the "sliding" spheres. This could be attributed to the preeminence of the forces driven by the pressure gradient in this case. However, the "rolling" motion is dominantly governed by the contact and proximity between the sphere and the channel wall, therefore, the predictions are more sensitive to the changes in δ. Results for the sphere of diameter 1 mm swimming in 1 Pa.s silicone oil and for the sphere of diameter 1.9 mm swimming in

0.5 Pa.s silicone oil are remarkably accurate in both linear regime and after the step-out occurs (Figure 3.25a and 3.25d). For the sphere with 1.9 mm diameter, the velocities are observed to be in very good agreement in the linear regime. Slope of the velocity vs. frequency plot in the linear regime for the sphere of diameter 1 mm swimming in silicone oil of viscosity 0.5 Pa.s is slightly off compared to the experimental results (Figure 3.25b). Further adjustment of the maximum proximity condition might be necessary for this case.
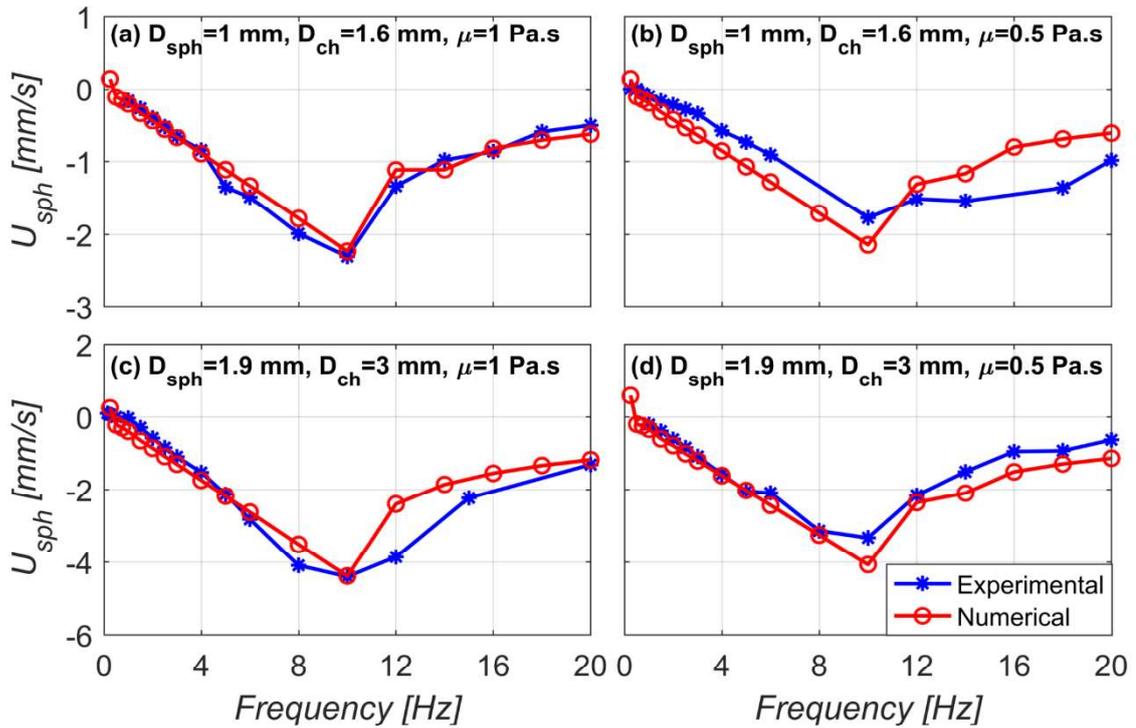
Figure 3.25 Comparison of the experimental results to the numerical predictions for D_{ch}/D_{sph} = 1.6 for two different silicone oil viscosities of μ = 1 Pa.s and μ = 0.5 Pa.s.

3.2.2.2. Rotation about x-axis

As demonstrated so far, kinematic model is accurate in predicting the results when the sphere is actuated by a magnetic field rotating about y-axis. Qualitatively, the model can predict helical trajectories. But, translational velocities of the spheres following helical paths cannot be predicted accurately with this model. This lack of accuracy stems from the missing lift force term in the model. Even though the sphere does not migrate

towards the center of the channel in each case, slight movement in radial direction is observed every time, except for the experiments with spheres in $D_{ch}/D_{sph} = 3$ configuration. With the omission of history and added mass terms, the net force balance becomes:

$$\mathbf{f}_{visc} + \mathbf{f}_{mag} + \mathbf{f}_g + \mathbf{f}_{lift} = 0 \tag{31}$$

where the viscous forces and torques balance external and inertial forces and torques. As explained in section 3.1.2.1. in the construction of the kinematic model, even though a formula for the lift force on the sphere in close proximity of another curved boundary is reported, the lift force is most likely to be proportional to the ever-recurring term $(\mathbf{\Omega} \times \mathbf{U})$. The reasoning behind this argument is visualized in Figure 3.26. If the lift force is proportional to $(\mathbf{\Omega} \times \mathbf{U})$, it becomes apparent why the sliding spheres can be focused while rolling spheres cannot be manipulated the same way. For the lift force to point towards the center of the cylindrical channel, ω_x and U must have the same sign, which only happens when the sphere is in the sliding mode. If the sphere were to roll along the channel wall, the resulting force calculated with this formula would be pushing the sphere further towards the channel wall. Hence, the experimental results which report that the hydrodynamic focusing can be achieved only with spheres in sliding mode would be consistent with the force balance.

Despite the experimental and numerical data supporting the relevance of the term $(\mathbf{\Omega} \times \mathbf{U})$ to the lift force, coefficients found in the literature need adjustment for the special case of a sphere inside a cylindrical channel having a boundary with a curvature. Kinematic model presented in this study is used to estimate the order of magnitude of the lift force required to hydrodynamically focus the sphere on the central axis of the cylindrical channel. Lift force reported by Rubinow and Keller [74] is included in the kinematic model as:

$$\mathbf{f}_{lift} = C\pi r_{sph}^3 \rho \left(\mathbf{\Omega} \times \mathbf{U} \right) \tag{32}$$

It is observed that the sphere follows a helical trajectory without experiencing lift when $C = 1$. After this result, C is gradually increased until the lift can be observed. The trajectory depicted in Figure 3.26 is obtained when the Rubinow-Keller lift is multiplied by 90, which is the smallest magnitude of the lift force where focusing is observed at all.

However, focusing takes place suddenly after the central axis is orbited by the sphere a few times, as opposed to the behavior seen in the experimental results, where the sphere slowly migrated towards the center at each turn.

(a)
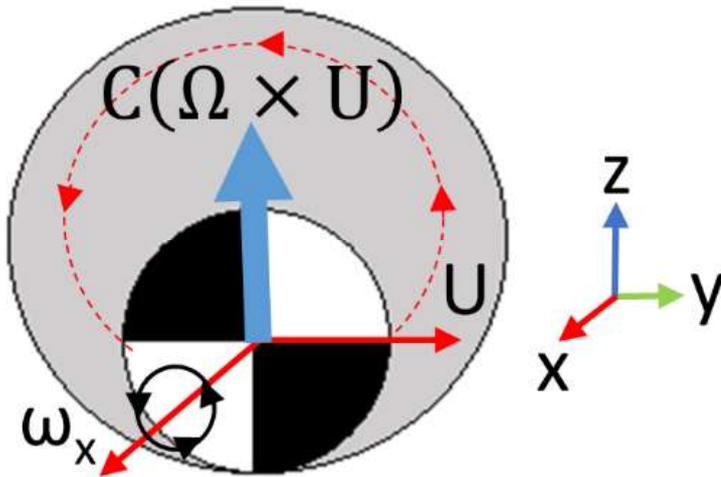
With C(**Ω×U**) term, rotation about x-axis and **sliding-mode** would lead to **focusing!**

(b)
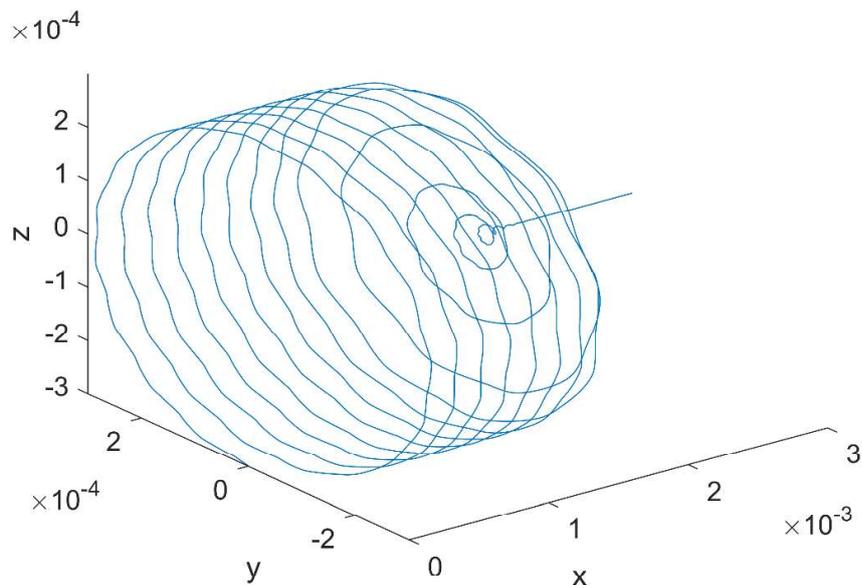
Figure 3.26 Trajectory of the 1.9 mm sphere inside the channel with 3 mm diameter predicted by the kinematic model when the lift force is applied 90 times the lift force suggested by Rubinow and Keller [74] for spheres swimming in bulk. It is observed that the radius of the helical trajectory decays suddenly under such a force as opposed to the incremental decay observed in the experiments.

3.3. Discussion

Magnetic spheres of two different diameters are rotated by means of an external field. Cylindrical glass channels of two different D_{sph}/D_{ch} ratios, in fluid medium consisting of silicone oils at two different viscosities. Depending on the ratio D_{sph}/D_{ch}, the spheres are observed to perform "rolling" or "sliding" motion when actuated by magnetic field rotating about y-axis. Rotation about x-axis resulted in various swimming trajectories depending on the magnetic field gradients and D_{sph}/D_{ch}. Sliding spheres are successfully focused along the channel axis, and they can follow helical trajectories.

Numerical model is very accurate in predicting the velocities for the spheres rotating about y-axis. However, the absence of the lift force term prevents capturing the focusing behavior and the translational velocity of spheres following helical trajectories.

As the first demonstration of the swimming behavior and focusing of the rotating rigid spheres inside cylindrical channels, this study makes novel contributions to the field of micro swimmers. However, finding the lift force on rotating spheres inside cylindrical conduits in the absence of a flow is crucial for predicting the focusing behavior and possibly modifying the position at which the spheres will be focused.

Table 3.3 Motion of the sphere based on actuation mode and frequency

Motion	Rotation		Magnetic Field	
	ω_x	ω_y	grad(B$_x$)	Frequency
Rolling	0	$\neq 0$	≥ 0	$0 - 30$ Hz
Sliding	0	$\neq 0$	≥ 0	$0.5 - 30$ Hz
Circle	$\neq 0$	0	0	$1 - 30$ Hz
Helical Trajectory	$\neq 0$	0	≥ 0	$1 - 5$ Hz
Focusing	$\neq 0$	0	> 0	$6 - 30$ Hz

4 CONCLUSION

Swimming characteristics of both helical structures and rigid spheres are investigated and following conclusions are made:

Swimming performance of helical structures are affected by the proportion of their geometric parameters greatly. Regardless of their cross-sectional shape. The wavelength presents with an optimum value that maximizes the velocity under both constant angular velocity and constant torque per wavelength applications. Increasing the helical radius results in faster swimmers up to an optimum value. However, optimum value of B for efficiency is much smaller. Therefore, one must decide on the magnitude of B considering the requirement of higher velocity or efficiency. Increased thickness almost always leads to better performance under constant torque applications. Despite that, at constant angular velocity applications, thinner structures are more beneficial due to the reduced drag. Presence of a confinement increases the swimming performance unless the confinement is too tight, so there is an optimum value. In case of swimmers with large width, coating them magnetically yields better results, as the increase in width always decreases the performance.

Axisymmetric particles such as spheres can also swim inside cylindrical channels despite their geometry. Hydrodynamic interactions between the sphere and the channel walls break the symmetry, thus the sphere becomes mobile. D_{sph}/D_{ch} ratio, rotation direction of the magnetic field and the frequency at which the sphere is actuated is crucial in determining the mode of swimming that can be achieved using spherical particles. It is observed that at tight confinements the sphere performs "sliding" motion, and sliding

spheres are capable of focusing to the central axis of the channel. Spheres are observed towards the region in the channel where the magnetic field gradient is zero, and they prefer to stay in this region. This is one of the most important findings in this study, as one can take advantage of this behavior for successful targeted drug delivery applications. Spheres can be accumulated in the targeted regions inside the body with the application of correct magnetic field gradients.

Trajectory and the velocity of the spherical particle rolling or sliding inside cylindrical conduits can be accurately predicted using the kinematic model. However, prediction of helical trajectories requires identifying the lift force acting on the sphere.

Resistance coefficients for the helical structures are functions of geometric parameters, namely, $R = f(\lambda, B, a, z_0, d, w, R_{ch}...)$. Resistance coefficients of the spheres are highly dependent on the distance of the spherical particle from the channel wall as well as the ratio of the diameters of the channel and the spherical particle: $R = f(\beta, D_{ch}/D_{ch,})$.

To compare the swimming performance of the helical structures and rigid spheres, one can consider the distance travelled by the swimmer per rotation as follows:

$$U_{sw}^{*} = U_{sw} / (L\omega) \tag{31}$$

Zhang et al. [23] report that the maximum speed their ribbon attained is achieved under 2 mT magnetic field strength with 18 μm/s at 30 Hz magnetic field rotation frequency. Length of the swimmer at the time of the experiment is 38 μm. Highest speed recorded in our experiments is 4.40 mm/s at 10 Hz, achieved by 1.9 mm sphere in sliding mode, with magnetic field strength 1.5 mT. Zhang et al. [23] used water in the experiments, which has the same viscosity as the silicone oil with 1 Pa.s viscosity used in our experiment. Therefore, we can compare the results reported by Zhang [23] for the ribbon to the performance of the spherical particle.

For the ribbon, we can choose the length scale as the length of the ribbon or the radius of the helical tail (1.4 μm):

$$U_{ribbon}^{*} = U_{ribbon} / (L_{ribbon}\omega) = 0.0156 \tag{33a}$$

$$U_{ribbon}^{*} = U_{ribbon} / (B_{ribbon}\omega) = 0.4286 \tag{33b}$$

For the sphere, we can choose the length scale as the diameter or the perimeter:

$$U_{sph}^* = U_{sph} / (D_{sph}\omega) = 0.2316 \qquad (34a)$$

$$U_{sph}^* = U_{sph} / (P_{sph}\omega) = 0.0737 \qquad (34b)$$

As demonstrated in equations 33-34, swimming performance of the helical tails and the rigid spheres are comparable. Rigid spheres also have the added advantage of being easier to manufacture and miniaturize, which makes them better candidates for small scale applications.

5   FUTURE WORK

The results obtained during the course of this thesis work indicate that identifying the lift force acting on a spherical particle swimming inside cylindrical conduits is crucial, therefore, CFD and experimental studies to this end will be conducted. To this end, an advanced CFD model solving Navier-Stokes equations will be constructed. Effect of various parameters such as β, channel and sphere diameters, viscosity of the working fluid on the lift force will be examined. Based on the results, an expression for the lift force acting on the spherical particles swimming inside cylindrical conduits will be derived as a function of the parameters investigated.

Visualization of the flow field might help understanding the dynamics better. To this end, PIV study with hollow glass particles can be carried on. Tests on non-Newtonian fluids will be performed to compare the results with the tests done in Newtonian fluids and construct a full dynamic model.

3D active control of the spherical particles will be studied. A complex channel system along which magnetic field gradients will vary can be constructed to implement targeted accumulation of spherical particles at desired regions. Helical swimmers with flexible tails and a spherical head will be manufactured and tested in both tight and loose confinements as a part of 3D trajectory control study. Non-magnetic particles of different sizes will be introduced to the system in order to test for mixing, sorting and focusing capabilities. Further applications such as virus enrichment and cargo transport will be explored.

6 REFERENCES

[1] E. M. Purcell, "Life at low Reynolds number," *Am. J. Phys*, vol. 45, no. June 1976, pp. 3–11, 1977.

[2] J. Wang, "Cargo-towing synthetic nanomachines: Towards active transport in microchip devices," *Lab Chip*, vol. 12, no. 11, pp. 1944–1950, 2012.

[3] A. I. Campbell, S. J. Ebbens, P. Illien, and R. Golestanian, "Experimental Observation of Flow Fields Around Active Janus Spheres," pp. 1–10, 2018.

[4] T. Qiu *et al.*, "Swimming by reciprocal motion at low Reynolds number.," *Nat. Commun.*, vol. 5, no. May, p. 5119, 2014.

[5] B. J. Nelson, I. K. Kaliakatsos, and J. J. Abbott, "Microrobots for minimally invasive medicine.," *Annu. Rev. Biomed. Eng.*, vol. 12, pp. 55–85, 2010.

[6] M. Sitti *et al.*, "Biomedical Applications of Untethered Mobile Milli/Microrobots," in *Proceedings of the IEEE*, 2015, vol. 103, no. 2, pp. 205–224.

[7] J. Feng and S. K. Cho, "Mini and micro propulsion for medical swimmers," *Micromachines*, vol. 5, no. 1, pp. 97–113, 2014.

[8] X. Yan *et al.*, "Magnetite Nanostructured Porous Hollow Helical Microswimmers for Targeted Delivery," *Adv. Funct. Mater.*, vol. 25, no. 33, pp. 5333–5342, 2015.

[9] F. Qiu and B. J. Nelson, "Magnetic Helical Micro- and Nanorobots: Towards Their Biomedical Applications," *Engineering*, vol. 1, no. 1, pp. 21–26, 2015.

[10] C. Brennen and Howert Winet, "Fluid Mechanics of Propulsion By Cilia and Flagella," *Annu. Rev. Fluid Mech.*, vol. 9, no. Lehninger 1971, pp. 339–398, 1977.

[11] J. Elgeti, R. G. Winkler, and G. Gompper, "Physics of microswimmers--single particle motion and collective behavior: a review.," *Rep. Prog. Phys.*, vol. 78, no. 5, p. 056601, 2015.

[12] P. P. Lele, T. Roland, A. Shrivastava, Y. Chen, and H. C. Berg, "The flagellar motor of Caulobacter crescentus generates more torque when a cell swims backwards," *Nat. Phys.*, vol. 12, no. November, pp. 175–179, 2015.

[13] A. Barbot, D. Decanini, and G. Hwang, "On-chip Microfluidic Multimodal Swimmer toward 3D Navigation.," *Sci. Rep.*, vol. 6, no. January, p. 19041, 2016.

[14] N. Beyrand, L. Couraud, A. Barbot, D. Decanini, and G. Hwang, "Multi-flagella helical microswimmers for multiscale cargo transport and reversible targeted binding," *IEEE Int. Conf. Intell. Robot. Syst.*, vol. 2015–Decem, pp. 1403–1408, 2015.

[15] G. Huang and Y. Mei, "Helices in micro-world: Materials, properties, and applications," *J. Mater.*, vol. 1, no. 4, pp. 296–306, 2015.

[16] Y. P. Zhao, D. X. Ye, G. C. Wang, and T. M. Lu, "Designing nanostructures by

glancing angle deposition," *Proc. SPIE Vol. 5219 Nanotub. Nanowires*, vol. 5219, pp. 59–73, 2003.

[17] M. M. Stanton, C. Trichet-Paredes, and S. Sanchez, "Applications of three-dimensional (3D) printing for microswimmers and bio-hybrid robotics.," *Lab Chip*, vol. 15, no. January, pp. 1634–1637, 2015.

[18] I. S. M. Khalil, F. Van Den Brink, O. S. Sukas, and S. Misra, "Microassembly using a Cluster of Paramagnetic Microparticles," in *IEEE International Conference on Robotics and Automation*, 2013, pp. 5507–5512.

[19] A. Ghosh and P. Fischer, "Controlled propulsion of artificial magnetic nanostructured propellers," *Nano Lett.*, vol. 9, no. 6, pp. 2243–2245, 2009.

[20] J. Li *et al.*, "Template electrosynthesis of tailored-made helical nanoswimmers.," *Nanoscale*, 2013.

[21] L. Liu, S. H. Yoo, S. A. Lee, and S. Park, "Wet-chemical synthesis of palladium nanosprings," *Nano Lett.*, vol. 11, no. 9, pp. 3979–3982, 2011.

[22] W. Gao *et al.*, "Bio-inspired Helical Microswimmer based on Vascular Plant," *Nano Lett.*, vol. 14, no. 1, pp. 305–310, 2013.

[23] L. Zhang *et al.*, "Characterizing the swimming properties of artificial bacterial flagella," *Nano Lett.*, vol. 9, no. 10, pp. 3663–3667, 2009.

[24] F. Qiu, R. Mhanna, L. Zhang, Y. Ding, S. Fujita, and B. J. Nelson, "Artificial bacterial flagella functionalized with temperature-sensitive liposomes for controlled release," *Sensors Actuators, B Chem.*, vol. 196, pp. 676–681, 2014.

[25] A. M. Maier, C. Weig, P. Oswald, E. Frey, P. Fischer, and T. Liedl, "Magnetic Propulsion of Microswimmers with DNA-Based Flagellar Bundles," *Nano Lett.*, vol. 16, no. 2, pp. 906–910, 2016.

[26] D. de Lanauze, O. Felfoul, J.-P. Turcot, M. Mohammadi, and S. Martel, "Three-dimensional remote aggregation and steering of magnetotactic bacteria microrobots for drug delivery applications," *Int. J. Robot. Res. *, vol. 33, no. 3, pp. 359–374, 2014.

[27] S. Martel and M. Mohammadi, "Using a swarm of self-propelled natural microrobots in the form of flagellated bacteria to perform complex micro-assembly tasks," *Proc. - IEEE Int. Conf. Robot. Autom.*, no. August, pp. 500–505, 2010.

[28] K. E. Peyer, S. Tottori, F. Qiu, L. Zhang, and B. J. Nelson, "Magnetic helical micromachines," *Chem. - A Eur. J.*, vol. 19, no. 1, pp. 28–38, 2013.

[29] W. Gao and J. Wang, "Synthetic micro/nanomotors in drug delivery," *Nanoscale*, vol. 00, no. September, pp. 1–9, 2014.

[30] F. Z. Temel and S. Yesilyurt, "Magnetically actuated micro swimming of bio-inspired robots in mini channels," *2011 IEEE Int. Conf. Mechatronics, ICM 2011 - Proc.*, pp. 342–347, 2011.

[31] L. Zhang and B. J. Nelson, "Rolled-up helical nanobelts: from fabrication to swimming microrobots Li Zhang and Bradley J. Nelson Institute of Robotics and Intelligent Systems, ETH Zurich, Tannenstrasse 3, Zurich, CH 8092, Switzerland," vol. 1272, pp. 1–6, 2010.

[32] J. Lighthill, "Flagellar Hydrodynamics: The John von Neumann Lecture, 1975," *SIAM Rev.*, vol. 18, no. 2, pp. 161–230, 1976.

[33] B. U. Felderhof, "Swimming at low Reynolds number of a cylindrical body in a circular tube," *Phys. Fluids*, vol. 22, no. 11, pp. 1–6, 2010.

[34] Y. Man and E. Lauga, "The wobbling-to-swimming transition of rotated helices," *Phys. Fluids*, vol. 25, no. 7, pp. 1–16, 2013.

[35] L. Koens and E. Lauga, "Slender-ribbon theory," *Phys. Fluids*, vol. 28, no. 1, pp. 0–26, 2016.

[36] B. Liu, K. S. Breuer, and T. R. Powers, "Propulsion by a helical flagellum in a capillary tube," *Phys. Fluids*, vol. 26, no. 1, 2014.

[37] S. E. Spagnolie and E. Lauga, "The optimal elastic flagellum," *Phys. Fluids*, vol. 22, no. 3, pp. 1–15, 2010.

[38] J. Lighthill, *Mathematical Biofluiddynamics*. Philadelphia, PA: SIAM, 1975.

[39] S. E. Spagnolie, B. Liu, and T. R. Powers, "Locomotion of helical bodies in viscoelastic fluids: Enhanced swimming at large helical amplitudes," *Phys. Rev. Lett.*, vol. 111, no. 6, 2013.

[40] L. Li and S. E. Spagnolie, "Swimming and pumping by helical waves in viscous and viscoelastic fluids," *Phys. Fluids*, vol. 27, no. 2, 2015.

[41] T. D. Montenegro-Johnson *et al.*, "Microscale flow dynamics of ribbons and sheets," *Soft Matter*, vol. 490, no. 3, pp. 15–35, 2017.

[42] E. E. Keaveny and M. J. Shelley, "Applying a second-kind boundary integral equation for surface tractions in Stokes flow," *J. Comput. Phys.*, vol. 230, no. 5, pp. 2141–2159, 2011.

[43] E. E. Keaveny, S. W. Walker, and M. J. Shelley, "Optimization of chiral structures for microscale propulsion," *Nano Lett.*, vol. 13, no. 2, pp. 531–537, 2013.

[44] A. Acemoglu and S. Yesilyurt, "Effects of geometric parameters on swimming of micro organisms with single helical flagellum in circular channels," *Biophys. J.*, vol. 106, no. 7, pp. 1537–1547, 2014.

[45] H. Brenner and J. Happel, "Slow viscous flow past a sphere in a cylindrical tube," *J. Fluid Mech.*, vol. 4, no. 2, pp. 195–213, 1958.

[46] A. J. Goldman, R. G. Cox, and H. Brenner, "Slow viscous motion of sphere parallel to a plane wall - I Motion through a quiescent fluid," *Chem. Eng. Sci.*, vol. 22, pp. 637–651, 1967.

[47] P. M. Bungay and H. Brenner, "The motion of a closely-fitting sphere in a fluid-filled tube," *Int. J. Multiph. Flow*, vol. 1, no. 1, pp. 25–56, 1973.

[48] J. J. L. Higdon and G. P. Muldowney, "Resistance functions for spherical particles, droplets and bubbles in cylindrical tubes," *J. Fluid Mech.*, vol. 298, pp. 193–210, 1995.

[49] S. Bhattacharya, C. Mishra, and S. Bhattacharya, "Analysis of general creeping motion of a sphere inside a cylinder," *J. Fluid Mech.*, vol. 642, pp. 295–328, 2010.

[50] L. Zhu, E. Lauga, and L. Brandt, "Low-Reynolds-number swimming in a capillary tube," *J. Fluid Mech.*, vol. 726, pp. 285–311, 2013.

[51] F. Lugli, E. Brini, and F. Zerbetto, "Shape governs the motion of chemically propelled Janus swimmers," *J. Phys. Chem. C*, vol. 116, no. 1, pp. 592–598, 2012.

[52] R. Dreyfus, J. Baudry, M. L. Roper, M. Fermigier, H. a Stone, and J. Bibette, "Microscopic artificial swimmers," *Nature*, vol. 437, no. 7060, pp. 862–865, 2005.

[53] A. Djellouli, P. Marmottant, H. Djeridi, C. Quilliet, and G. Coupier, "Buckling Instability Causes Inertial Thrust for Spherical Swimmers at All Scales," *Phys. Rev. Lett.*, vol. 119, no. 22, pp. 1–5, 2017.

[54] D. Takagi, J. Palacci, A. B. Braunschweig, M. J. Shelley, and J. Zhang, "Hydrodynamic capture of microswimmers into sphere-bound orbits," pp. 1784–1789, 2013.

[55] a. J. Goldman, R. G. Cox, and H. Brenner, "Slow viscous motion of a sphere parallel to a plane wall—II Couette flow," *Chem. Eng. Sci.*, vol. 22, no. 4, pp. 653–660, 1967.

[56] Y. J. Liu, J. Nelson, J. Feng, and D. D. Joseph, "Anomalous rolling of spheres down an inclined plane," *J. Nonnewton. Fluid Mech.*, vol. 50, no. 2–3, pp. 305–329, 1993.

[57] J. Bico, J. Ashmore-Chakrabarty, G. H. McKinley, and H. A. Stone, "Rolling stones: The motion of a sphere down an inclined plane coated with a thin liquid film," *Phys. Fluids*, vol. 21, no. 8, pp. 1–9, 2009.

[58] H. Brenner, "The slow motion of a sphere through a viscous fluid towards a plane surface," *Chem. Eng. Sci.*, vol. 16, no. 3–4, pp. 242–251, 1961.

[59] F. Charru, E. Larrieu, J. B. Dupont, and R. Zenit, "Motion of a particle near a rough wall in a viscous shear flow," *J. Fluid Mech.*, vol. 570, no. 2007, pp. 431–453, 2007.

[60] D. J. Jeffrey and Y. Onishi, "The slow motion of a cylinder next to a plane wall," *Q. J. Mech. appl. Math*, vol. 34, pp. 129–137, 1981.

[61] Z. Adamczyk, M. Adamczyk, and T. G. M. van de Ven, "Resistance coefficient of a solid sphere approaching plane and curved boundaries," *J. Colloid Interface Sci.*, vol. 96, no. 1, pp. 204–213, 1983.

[62] S. Navardi, S. Bhattacharya, and H. Wu, "Stokesian simulation of two unequal spheres in a pressure-driven creeping flow through a cylinder," *Comput. Fluids*, vol. 121, pp. 145–163, 2015.

[63] B. Cichocki, B. U. Felderhof, K. Hinsen, E. Wajnryb, and J. Bławzdziewicz, "Friction and mobility of many spheres in Stokes flow," *J. Chem. Phys.*, vol. 100, no. 5, pp. 3780–3790, 1994.

[64] A. B. Basset, *A treatise on hydrodynamics: with numerous examples*. Deighton, Bell and Company, 1888.

[65] J. Boussinesq, *Théorie analytique de la chaleur: mise en harmonie avec la thermodynamique et avec la théorie mécanique de la lumière*. Gauthier-Villars, 1903.

[66] C. W. Oseen, *Neuere Methoden und Ergebnisse in der Hydrodynamik*. Leipzig: Akademische Verlagsgesellschaft M. B. H., 1927.

[67] M. R. Maxey and J. J. Riley, "Equation of motion for a small rigid sphere in a nonuniform flow," *Phys. Fluids*, vol. 26, no. 4, pp. 883–889, 1983.

[68] C.-M. Tchen, "Mean Value and Correlation Problems connected with the Motion of Small Particles suspended in a turbulent fluid," Technische Universiteit Delft, 1947.

[69] J. Corrsin, S; Lumley, "On the equation of motion for a particle in turbulent fluid," *Appl. Sci. Res.*, vol. 6, pp. 114–116, 1965.

[70] Y. A. Buevich, "Motion resistance of a particle suspended in a turbulent medium," *Inzv. AN SSSR*, vol. 1, no. July, pp. 182–183, 1966.

[71] S. L. Soo, "Equation of motion of a solid particle suspended in a fluid," vol. 18, no. 1975, pp. 263–264, 1988.

[72] M. Gitterman and V. Steinberg, "Memory effects in the motion of a suspended particle in a turbulent fluid," vol. 23, pp. 2154–2160, 1980.

[73] M. P. Auton, T. R.; Hunt, J. C. R.; Hommeii, "The force exerted on a body in inviscid unsteady non-uniform rotational flow," *J. Fluid Mech.*, vol. 197, pp. 241–257, 1988.

[74] S. I. Rubinow and J. B. Keller, "The transverse force on a spinning sphere moving in a viscous fluid," *J. Fluid Mech.*, vol. 11, no. 03, p. 447, 1961.

[75] P. G. Saffman, "The lift on a small sphere in a slow shear flow," *J. Fluid Mech.*, vol. 22, no. 02, p. 385, 1965.

[76] D. A. Drew, "The lift force on a small sphere in the presence of a wall," *Chem. Eng. Sci.*, vol. 43, no. 4, pp. 769–773, 1988.

[77] R. G. Cox and H. Brenner, "The lateral migration of solid particles in Poiseuille flow - I theory," *Chem. Eng. Sci.*, vol. 23, no. 2, pp. 147–173, 1968.

[78] B. P. . L. Ho L.G., "Inertial migration of rigid spheres in two-dimensional unidirectional flows," *J. Fluid Mech.*, vol. 65, no. 2, pp. 365–400, 1974.

[79] P. Vasseur and R. G. Cox, "The lateral migration of a spherical particle in two-dimensional shear flows," *J. Fluid Mech.*, vol. 78, no. 2, pp. 385–413, 1976.

[80] R. G. Cox and S. K. Hsu, "The lateral migration of solid particles in a laminar flow near a plane," *Int. J. Multiph. Flow*, vol. 3, no. 3, pp. 201–222, 1977.

[81] J. B. McLaughlin, "The lift on a small sphere in wall-bounded linear shear flow," *J. Fluid Mech.*, vol. 246, pp. 249–265, 1992.

[82] P. Cherukat and J. B. Mclaughlin, "The inertial lift on a rigid sphere in a linear shear flow field near a flat wall," *J. Fluid Mech.*, vol. 285, no. 1, p. 407, 1995.

[83] G. P. Krishnan and D. T. Leighton, "Inertial lift on a moving sphere in contact with a plane wall in a shear flow," vol. 7, pp. 2538–2545, 1995.

[84] D. Leighton and A. Acrivos, "The lift on a small sphere touching a plane in the presence of a simple shear flow," *ZAMP Zeitschrift für Angew. Math. und Phys.*, vol. 36, no. 1, pp. 174–178, 1985.

[85] D. Hall, "Measurements of the mean force on a particle near a boundary in turbulent flow," *J. Fluid Mech.*, vol. 187, pp. 451–466, 1988.

[86] J. A. Schonberg and E. J. Hinch, "Inertial migration of a sphere in Poiseuille flow," vol. 203, pp. 517–524, 1989.

[87] H. Lee and S. Balachandar, "Drag and lift forces on a spherical particle moving on a wall in a shear flow at finite Re," *J. Fluid Mech.*, vol. 657, pp. 89–125, 2010.

[88] E. Purcell, "Life at low Reynolds number," *American Journal of Physics*, vol. 45, no. 1. p. 3, 1977.

[89] E. Demir and S. Yesilyurt, "Low Reynolds number swimming of helical structures in circular channels," *J. Fluids Struct.*, vol. 74, 2017.

[90] "COMSOL Multiphysics® v. 5.2. www.comsol.com. COMSOL AB, Stockholm, Sweden." .

[91] J. J. L. Higdon, "The hydrodynamics of flagellar propulsion: helical waves," *J. Fluid Mech.*, vol. 94, no. 02, p. 331, 1979.

[92] R. Maniyeri, Y. K. Suh, S. Kang, and M. J. Kim, "Numerical study on the propulsion of a bacterial flagellum in a viscous fluid using an immersed boundary method," *Comput. Fluids*, vol. 62, pp. 13–24, 2012.

[93] H. Wu *et al.*, "Amoeboid motion in confined geometry," *Phys. Rev. E - Stat. Nonlinear, Soft Matter Phys.*, vol. 92, no. 5, pp. 1–5, 2015.

[94] M. Farazmand and G. Haller, "The Maxey-Riley Equation: Existence, Uniqueness and Regularity of Solutions," *Nonlinear Anal. Real World Appl.*, vol. 22, pp. 98–106, 2013.

[95] H. H. Jakobsen, "Escape response of planktonic protists to fluid mechanical signals," *Mar. Ecol. Prog. Ser.*, vol. 214, pp. 67–78, 2001.

[96] M. van Aartrijk and H. J. H. Clercx, "Vertical dispersion of light inertial particles in stably stratified turbulence: The influence of the Basset force," *Phys. Fluids*, vol. 22, no. 1, pp. 1–9, 2010.

[97] S. Wang and A. M. Ardekani, "Unsteady swimming of small organisms," *J. Fluid Mech.*, vol. 702, pp. 286–297, 2012.

[98] H. C. Berg and L. Turner, "Movement of microorganisms in viscous environments [12]," *Nature*, vol. 278, no. 5702. pp. 349–351, 1979.

[99] Y. Magariyama and S. Kudo, "A mathematical explanation of an increase in bacterial swimming speed with viscosity in linear-polymer solutions," *Biophys. J.*, vol. 83, no. 2, pp. 733–739, 2002.